Cortical actomyosin network organization in epithelial cells

Christoph Klingner

Dissertation
an der Fakultät Physik
der Ludwig–Maximilians–Universität
München

vorgelegt von
Christoph Klingner
aus Dresden

München, den 17.04.2014

Erstgutachter: Prof. Joachim Rädler
Zweitgutachter: Prof. Roland Wedlich-Söldner
Tag der mündlichen Prüfung: 05.06.2014

Contents

List of Figures

List of Tables

List of Abbreviations

μm	Micrometer
°C	Degree celcius
AFM	Atomic force microscopy
ATP	Adenosine-5'-triphosphate
ATPase	Adenosine triphosphate hydrolase
au	Arbitrary unit
BP	Bending parameter
bp	Base pair
Ca	Calcium
CCD	Charged-coupled device
CoM	Center of mass
cov	Covariance
DNA	Deoxyribonucleic acid
ECs	Epithelial cells
ER	Endoplasmatic reticulum
f-actin	filamentous actin
Fig.	Figure
FLIM	Fluorescence lifetime imaging microscopy
FM	Fluorescence microscopy
FRAP	Fluorescence recovery after photobleaching
FRET	Fluorescence resonance energy transfer

GFP	Green fluorescent protein
GTP	Guanine triphosphatase
HGF	Hepatocyte growth factor
ICS	Image correlation spectroscopy
ITIC	Incremental temporal image correlation
LatA	Latrunculin A
LatB	Latrunculin B
MDCK	Madin Darby Canine Kidney
MHCA	Non muscle myosin heavy chain A
MHCB	Non muscle myosin heavy chain B
MIT	Massachusettes Intstitue of Technology
MLC	Non muscle myosin regulatory light chain
MLCK	Myosin light chain kinase
MPI	Max-Planck Institute
MV	Microvilli
n	Number of samples
ng	nanogramm
nm	Nanometer
PC	Pearson coefficient
PCF	Pearson correlation function
PIV	Particle image velocimetry
PSF	Point spread function
ROI	Region of interest
SCF	Spatial correlation function
SE	Standard error
sec	Seconds

SEM	Scanning electron microscopy
STD	Standard deviation
STICS	Spatiotemporal image correlation spectroscopy
t	Time
TCF	Temporal correlation function
TIRF	Total internal reflection fluorescence

Zusammenfassung

Epithelzellen, die Modell-Zelllinien dieser Dissertation, sind für die Aufteilung und Abtrennung verschiedener Kompartimente eines Organismus zuständig, indem sie sich zu Grenzflächen zusammenschliessen, welche häufig hohen physikalischen Spannungen und Kräften ausgesetzt sind. Um diese physikalischen Kräfte zu verarbeiten oder sie selbst zu produzieren, verwenden Epithelzellen, wie alle anderen Zelltypen auch, das Zytoskelett, das sich im Allgemeinen aus den Komponenten Mikrotubuli, Intermediär-Filamenten und Aktin sowie den damit korrespondierenden Motorproteinen Dynein, Kinesin sowie Myosin zusammensetzt.

In dieser Dissertation wird das Zusammenspiel von Aktin und Myosin auf der apikalen Seite von Epithelzellen untersucht. Im Falle von konfluenten Zellen mit vollständig ausgebildeten Zell-Zell-Kontakten sind auf der apikalen Seite der Zellen Mikrovilli zu finden, kleine, mit Aktin-Bündeln gefüllte Ausstülpungen aus der Zelloberfläche, welche für die optimierte Nahrungsaufnahme sowie als Antennen für Signalverarbeitung zuständig sind. Im Zuge der Arbeit konnten wir feststellen, dass sich der Aktin-Myosin-Aufbau auf der apikalen Seite von Einzelzellen ohne Zell-Zell-Kontakte, sogenannten nicht-konfluenten Zellen, grundsätzlich ändert. Mittels Fluoreszenz-Mikroskopie und anderen experimentellen Methoden zeigen wir, dass zwar ähnliche Ausstülpungen auf der apikalen Oberfläche von Einzelzellen zu finden, diese jedoch häufig verlängert, gebogen, hoch-dynamisch und oft parallel zur Zellmembran orientiert sind. Wir zeigen mittels molekularbiologischer Methoden, dass ein zusätzliches, innerhalb der apikalen Zellmembran liegendes isotropes Akto-Myosin-Netzwerk für die dynamische Reorganisation der Mikrovilli-Ausstülpungen verantwortlich ist.

Der Identifizierung des isotropen Akto-Myosin-Netzwerkes, welches eine der Hauptaussagen dieser Dissertation ist, wird eine detaillierte Analyse der dynamischen Netzwerkreorganisation angefügt, die mittels temporaler und örtlicher Bild-Korrelationsanalysen charakteristische Zeiten und Längen der Dynamik definiert. Des Weiteren entwickeln wir mehrere Bild-Analyseverfahren, allen voran die Methode der iterativen temporalen Bildkorellation sowie des optischen Flusses, wodurch wir eine Oszillation der Netzwerk-Reorganisationsgeschwindigkeit identifizieren und parametrisieren können. Verschiedene, auf Fluoreszenzmikroskopie und automatisierter optischer Fluss-Bildanalyse basierende Experimente geben Hinweise auf zwei mögliche Erklärungen für die identifizierten Oszillationen. Sowohl Myosin aktivitätsregulierende Proteine als auch spontan auftretende Spannungsfluktuationen im unter Zugspannung liegenden Netzwerk können mögliche Ursachen für die identifizierten Netzwerkoszillationen sein. Obwohl eine eindeutige zelluläre Funktion des apikalen Akto-Myosin-Netzwerkes im Rahmen dieser Doktorarbeit noch nicht identifiziert werden konnte, so können wir aufgrund von verschiedenen Resultaten dennoch postulieren, dass das hier identifizierte Netzwerk eine entscheidende Rolle bei der Zellmigration und Signaltransduktion einnimmt. Unabhängig davon repräsentiert das hier gefundene Netzwerk die faszinierende Möglichkeit, ein aktives, zweidimensionales Akto-Myosin-Netzwerk nicht nur *in vitro*, sondern in seiner natürlichen Umgebung studieren und biophysikalische Eigenschaften analysieren zu können.

Abstract

The cytoskeleton plays a central role in cellular morphogenesis by generating, sensing and transmitting physical forces. Actin filaments are key cytoskeletal elements that are mostly located close to the cell cortex. They can generate protrusive or contractile forces in combination with myosin motor proteins. We have identified a novel, highly dynamic actin structure at the apical side of non-polarized epithelial cells that is driven by an underlying non muscle myosin II network. By using various image analysis techniques, such as maximum intensity tracking, optical flow and correlation analysis, we observe contractile actomyosin activity within subregions of the cell cortex. The resulting spatially restricted mechanical forces differ in directionality which leads to shear stress and friction within the apical cell cortex. Additionally, we identified a global oscillatory behavior using autocorrelation analysis methods. The actomyosin network oscillates between states of low and high activity, as confirmed by iterative temporal image correlation (ITIC), a newly developed method for global feature extraction from image sequences, and highest intensity tracking. These remarkable features of subcellular cortex regulation give important insights into how mechanical force generation and propagation control cell shape and migration in non-polarized epithelial cells.

Chapter 1

General introduction

It is commonly known that cells are the basic living units to form biological higher order organisms. To achieve the goal of organism formation, various cell types with distinct features and functions have to work together. By features, we mean that some cells can survive on their own while others need cell neighbors. Some cells are multi-functional while others are highly specified. Some cells are flat while others are thick or round. Some cells are highly motile whereas others stick to their position. Nevertheless, despite the broad diversity in cell type features, all cells exhibit some universal traits. They need nutrition for survival, they can divide and they need to create, maintain and resist physical forces. These physical forces are essential for more than keeping the cells in their specific shape, transporting cargo within the cell or dividing the two subparts during cell division. These physical forces are also essential for the cell to adapt and communicate with its environment, to hold on to its supporting substrate, to move around and to resist and exert force to surrounding barriers.

A broad range of implications concerning cellular physical forces, both for the cell as well as for its environment, have been described in recent years. In the last century great effort has been invested in understanding the biochemical pathways within cells thereby shedding light on the interplay between chemistry and biology. In the last decades the focus broadened, due to technological advances, to now identify and comprehend the interaction of physics and biology in cells by e.g. introducing mechanics as a regulating process. This mechanobiology field has recently shown, by fascinating experiments, that physical forces and mechanics are not to be neglected to understand cellular functions (Ref.[94]). For example, pluripotent stem cells have been demonstrated to differentiate into neuronal, muscle or bone precursor cells only depending on the elastic substrate stiffness (Ref.[30],[31]). Hence, purely mechanistic properties of the environment already influence cellular fate thereby demonstrating the importance of understanding the linkage between physical force and cellular behavior.

The three main directions of biophysical and mechanobiology research are (1) mechanosensing, which questions how cells can sense physical forces (Ref.[40],[97]), (2) mechanotransduction, which questions how the cell can transform mechanical cues to biochemical signals (Ref.[173],[181],[18]), and (3) mechanosignalling, which questions if and how cells can produce and receive mechanical signals (Ref.[92],[154]). For all of these processes the cell itself needs to create physical forces to counterbalance, exert or translate the mechanical cues. Though, the question remains - how does the cell create force?

In cells, the cytoskeleton is the key player in the generation, maintenance and transmission of physical forces. It consists of three main components, namely (1) the microtubules, (2) the intermediate filaments and (3) the actin filament structures. The functions of these key

cellular players are very diverse ranging from transport processes, transmission of mechanical signals to other cell regions, resistance to compressive forces, stress absorbance, cellular motility, to creating protrusions in the cell cortex. For the key components microtubule and actin one way to generate or resist forces is to assemble to filamentous structures. This filament assembly, also named polymerization, can already lead to generation of force when one end of the filament is fixed to a stable reference point. Then polymerization at the other end leads to pushing forces (Ref.[127]). Alternatively the cytoskeletal filaments can be arranged in entangled networks that then sustain compressive forces (Ref.[9]).

The second way to create forces in cells also involves the cytoskeleton and another set of very abundant proteins, namely the motor proteins. These motor proteins walk along the filamentous cytoskeletal structures. Notably, for the motor proteins to function properly the cytoskeletal filaments have to be polar. Filament polarity of filament means that two distinguishable ends are defining a directionality. Actin filament ends can be differentiated due to differences in polymerization and depolymerization speeds (Ref.[127],[130]). The filament polarity then distinguishes the motor protein direction of movement. Intermediate filaments are not known to be polar and no related motor protein is known so far. For microtubules, the corresponding motor protein classes are kinesins and dyneins (Ref.[57],[75]). Actin filament-related motor proteins belong to the protein superfamily of myosins. Myosins either walk along actin filaments and function as transporters (Ref.[48]) or several myosins tether two antiparallel actin filaments by preforming so called minifilaments with several head groups at both ends that can consequently slide the two filaments against each other. In muscle fibers, for example, the antiparallel actin filaments are fixed at their opposing ends to some cellular structure. The myosin minifilaments are then causing cell contraction upon external stimulus (Ref.[45]). However, not only muscle cells depend on the functional actomyosin interplay. Actomyosin structures are extremely versatile in function. Hence, all other cell types utilize actomyosin as well to generate contractile forces and for translocation purposes.

This thesis focuses on epithelial cells, a cell type that is responsible for compartimantalisation of tissues in multicellular organisms. To maintain the organization of tissue boundary layers epithelial cells must generate and bear significant mechanical force and stress. Hence, within epithelial cells, various distinct actomyosin structures help to generate and bear physical forces. The most prominent actomyosin structures in these cells are (1) stress fibers, that connect the cell to its substrate via focal adhesion (Ref.[113]), (2) the cortical actin network, coupling to membrane-actin associating proteins and being related to signal transduction (Ref.[175],[50]), and (3) the circumferential ring, that tightly binds epithelial cells to its neighbors via adherens junctions thereby providing the physical link to transmit forces within a cellular sheet ((Ref.[50],[132])) (Fig. 1.1).

At the top of the cell, named apical region (Fig. 1.1), thick actin bundles protrude perpendicularly from the cell surface. These protrusions are called microvilli (MV) and are related to functions such as increasing the apical cell surface for optimized nutrition uptake as well as regulating energy metabolism, gating ion flux, generating and modulating membrane potential and calcium ion signaling and storage (Ref.[90]).

The typical physiological situation for epithelial cells is largely defined by confluence, which relates to the formation of a cellular monolayer with defined apical and basal regions and the resulting characteristic actomyosin structures. Such polarized epithelial layers can be found in the small intestine, where they take up nutrition at their apical side, transport it

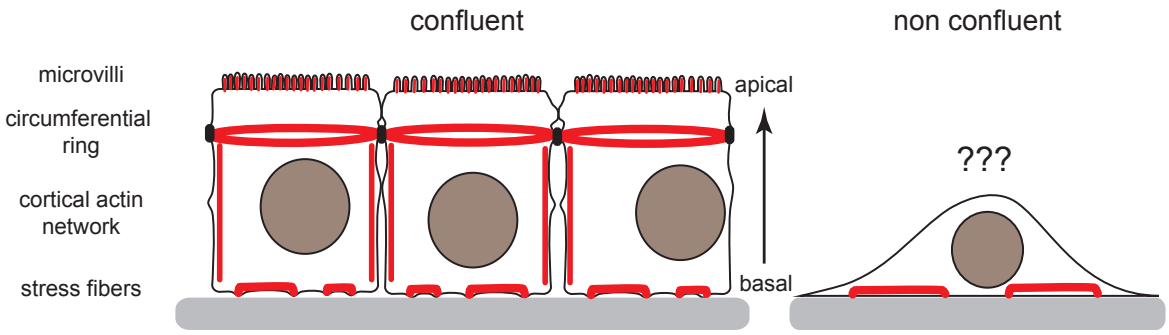

Figure 1.1: Schematic of confluent cell monolayer (left) and non-confluent cell (right) with characteristic actomyosin structures (red) from basal to apical region: stress fibers, cortical actin network, circumferential ring and microvilli protrusions. Dome-shaped non-confluent cells (right) are well-known to exhibit stress fibers for migration while actomyosin organization of apical region is not yet well described.

through the cell and dispense it at their basal region for further use in the compartmentalized tissue (Ref.[114]). However, in some cases epithelial cells lose their cell-cell contacts, e.g. upon wounding, which results in non-confluent cells that are dome-shaped (Fig. 1.1, right). These cells exhibit different actomyosin structures as they are now in a migratory state. non-confluent cells have enhanced stress fiber formation and they frequently exhibit actin based basal protrusions called lamellipodia and filopodia enabling them to migrate (Ref:[171]). While most insights regarding actin behavior in non-confluent cells was obtained studying lamellipodia, filopodia and stress fibers, only little is known so far about the actomyosin organization in the apical region of non-confluent cells (Fig. 1.1, right).

In this thesis, we are investigating the actomyosin organization at the apical side of non-confluent cells. We can identify that non-confluent cells as well exhibit microvilli protrusions at their apical side (chapter 3). However, these protrusions feature distinct differences, compared to microvilli in confluent epithelial cells, such as being bent and more elongated structures with partial membrane-parallel orientation and less abundance. Most importantly though, the microvilli of non-confluent cells are highly dynamic compared to confluent microvilli. We could elucidate that this process is myosin-driven.

The involvement of myosin motor proteins prompted us to more carefully investigate the localization and interplay of myosin and actin. Interestingly, we identify an isotropic myosin network underlying the cell plasma membrane (chapter 4). This extensive network is not unique to our standard model cell line, Madine-Darby Canine Kidney cells (MDCK), but is prominent in various epithelial and epithelial-like cells from different physiological backgrounds, e.g. carcinoma, osteosarcoma or fibroblast cell types. Hence, this isotropic apical myosin network is presumably a universal feature of non-confluent epithelial cells.

Astonishingly, the co-localization experiments for actin and myosin in stably double transfected cells reveal that the two proteins only partially overlap (chapter 5). However, myosin is not known to establish network structures without supporting actin filament structures. By using Latrunculin, an actin filament sequestering drug, we show that the myosin network

ruptures thereby confirming, that within the network thin actin filaments must be present. Furthermore, we confirm by temporal, spatial and spatiotemporal (STICS) image correlation analysis that the actin-filled microvilli protrusion and the myosin network structure are interlinked. Considering all findings of chapters 3 to 5, we postulate a model of two different actin based apical structures in non-confluent cells. First, we find highly dynamic microvilli with distinct characteristics on the apical side of non-confluent cells. Second and more importantly, we postulate the existence of an extensive isotropic actin filament network parallel to the apical plasma membrane that is covered by attaching myosin filaments. Though we are unable to visualize the actin network with fluorescence markers, probably due to only thin filamentous structures compared to the thick and highly fluorescent microvilli bundles, we consider this apical actomyosin network a key mechanical regulator of the apical cell cortex, as we can additionally show that this network is under considerable physical tension.

In the second part of this thesis we concentrate on characterizing the apical actomyosin network dynamics in more detail. By applying various computer based image analysis methods we demonstrate that the cortical network oscillates between states of high and low reorganization activity (chapter 6). To characterize these oscillations we have developed a novel iterative temporal image correlation analysis (ITIC) that allows us to distinguish between states of high and low reorganization speed. With an additional highly advanced image analysis approach, the optical flow method, we verify the ITIC finding and subsequently adapt this optical flow program to allow for large scale cellular screens using drugs and protein expression approaches to possibly identify a mechanism responsible for this oscillatory network behavior.

To find this oscillation pace maker we interfere with different members of the myosin regulating protein cascade (chapter 7). Using chemical inhibitors as well as intracellular calcium chelators we are able to reduce oscillation period and network dynamics. On the other hand we can slightly enhance the oscillation period by either using hepatocyte growth factor (HGF), a paracrine that is involved in wound healing and organ regeneration (Ref.[15]), or by expressing constitutively active RhoA protein. Even though the experimental and image analysis results give very promising first indications of possible pace makers, the screens partially lack the final statistical robustness to pinpoint one key regulating mechanism.

Finally, we characterize how the newly identified cortical myosin network influences the cortical elasticity of cells (chapter 8). It was reported earlier that MDCK cells undergo oscillatory changes in cell elasticity (Ref.[148]). Thus, we use combined atomic force and fluorescence microscopy to check for a link between the oscillatory myosin network behavior and the periodic change of cortical cell elasticity. Although the oscillation periods of elasticity and network reorganization speed are very similar, we are not able to confirm a direct dependency by means of cross-correlation analysis. Nevertheless, we presume that there should be a mechanical link between the two processes. Finding this mechanical coupling should be a strong focus point in future experiments.

A very interesting observation led to an alternative explanation of myosin network reorganization. When cutting through large fractions of the isotropic network with a pulsed UV laser ablation system, the remaining network motion stalls completely for long time periods. If the system is under isotropic tension, small and local force imbalances already result in oscillatory behavior of the network. This feature can be described using the so called tensegrity model, which postulates the interplay of tension and stiffness being the basic and sufficient units for

assembling high order structures (Ref.[65]). Moreover, we will briefly discuss a closely related model of active gel behavior (Ref.[69]).

This thesis is structured in the way that each chapter has its own introductory and discussion part, which we refer to for detailed interpretation of the experimental results. The final discussion and outlook at the end of this thesis will recapitulate the most important findings and present a short outlook of possible directions for future research regarding the apical cell cortex organization, regulation and characterization of non-confluent epithelial cells.

Chapter 2

Materials and Methods

2.1 Molecular Biology

2.1.1 Strains

Bacterial Strains

***Echerichia coli* strain** Top10 (Invitrogen) was used for all molecular cloning procedures. Top10 is very similar to the *E.coli* strain DH10B (Invitrogen) which is a derivative from the original *E.coli* strain K12: F^- *endA1 recA1 galE15 falK16 nuG rpsL* Δ*lacX74*Φ *80lacZ*Δ *M15 araD139*Δ *(ara,leu)7697mcrA*Δ *(mrr-hsdRMS-mcrBC)*λ^-

Mammalian Strains

MDCK epithelial model cell line of class II, a derived sub-clone from the heterogeneous parent line MDCK. MDCK II cells were bought from ATCC. Species: *dog*

HeLa epithelial model cell line derived from adenocarcinoma cancer from cervix tissue. Cells were kind gift of Prof. A.Ullrich group (MPI Biochemistry). Species: *human*

MCF 7 epithelial model cell line derived from adenocarcinoma cancer from breast tissue. Cells were kind gift of Prof. A.Ullrich group (MPI Biochemistry). Species: *human*

PancI epithelioid carcinoma model cell line derived from pancreas cancer of duct tissue. Cells were kind gift of Prof. R.Faessler group (MPI Biochemistry). Species: *human*

U2OS epithelial model cell line derived from osteosarcoma cancer from bone tissue. Cells were kind gift of Prof. R.Faessler group (MPI Biochemistry). Species: *human*

Cos7 fibroblast model cell line derived from transformed SV40 cell line from kidney tissue. Cells were kind gift of Prof. A.Ullrich group (MPI Biochemistry). Species: *Cercopithecus aethiops*

NIH-3T3 fibroblast model cell line derived from NIH/Swiss strain from embryo tissue. Cells were kind gift of Prof. A.Ullrich group (MPI Biochemistry). Species: *Mus musculus, mouse*

Transfected mammalian strains

Strain	Plasmid No.	Cell Type	Selection (μl/10ml)	Transfection
LA-GFP-H6-8	RWM142	MDCK	Hygromycin (60)	stable
β-actin-H6-6	pAC-β-actin-GFP1 -Hyg-Cm (library CK)	MDCK	Hygromycin (60)	stable
MHCA-GFP-H6-1	RWM130	MDCK	Hygromycin (60)	stable
MLC-GFP-H8-1	RWM132	MDCK	Hygromycin (80)	stable
MHCA-MLC-H6P2-4	RWM130 (GFP) RWM155 (mCherry)	MDCK	Hygromycin (60) Puromycin (20)	stable
MHCA-LA-H6P3-1	RWM130 (GFP) RWM137 (mCherry)	MDCK	Hygromycin (60) Puromycin (30)	stable
HeLa-MLC-GFP-H6-1	RWM132	HeLa	Hygomycin (60)	stable
HeLa-MLC-GFP-H6-7	RWM132	HeLa	Hygomycin (60)	stable
U20-MHCA-GFP	RWM131	U2O	none	transient
MCF7-MHCA-GFP	RWM131	MCF7	none	transient
COS7-MHCA-GFP	RWM131	COS7	none	transient
NIH-3T3-MHCA-GFP	RWM131	NIH-3T3	none	transient
PancI-MHCA-GFP	RWM131	PancI	none	transient

Table 2.1: List of transfected mammalian cells

2.1.2 Molecular Biology Kits

- Agarose Gel Extraction Kit (Jena Bioscience) for DNA-fragment isolation
- Agarose Gel Extraction Kit (Promega) for DNA-fragment isolation
- Qiagen®Plasmid MiniKit (QIAGEN) for plasmid minipreparation
- Qiagen®Plasmid MaxiKit (QIAGEN) for plasmid maxipreparation
- Ezna^{TM}Plasmid MiniKit for plasmid minipreparation
- Mycoplasm Detection Kit (Jena Bioscience) for mycoplasm checks

2.1.3 DNA handling

All DNA handling using molecular biology kits were performed according to instructions provided by (1) Jena Bioscience, (2) Promega, (3) Qiagen®Plasmid MiniKit/MaxiKit (QIAGEN), (4) Ezna^{TM}Plasmid MiniKit, and (5) Mycoplasm Detection Kit.

2.1.4 Plasmid constructs RWM list

The following plasmids were either bought from Clonetech company, addgene library, or the plasmid constructs were cloned by Dr. R.Aufschnaiter (RWM65/66/98/124/) or by C.Klingner (RWM130/131/132/133/135/137/142/155/156).

Name	Insert	Vector	Resistance (bacteria)	Source
RWM49	empty	pAcGFP1-C1	kanamycin	from Clonetech
RWM50	empty	pAcGFP1-N1	kanamycin	from Clonetech
RWM51	empty	pAcGFP1-Hyg-N1	ampicillin	from Clonetech
RWM52	empty	pAcGFP1-Hyg-C1	ampicillin	from Clonetech
RWM65	empty	pAcGFP-Hyg-Cm	ampicillin	modified MCS: NotI cutting site inserted
RWM66	empty	TagRFP-T-Hyg-Cm	ampicillin	modified TagRFP exchange RWM65
RWM98	Lifeact-mCherry	mCherry-T-Hyg-N1	ampicillin	modified Lifeact-mCherry intoRWM66
RWM124	empty	pmCherry-Hyg-N1	ampicillin	fluorophore change in RWM51
RWM125	empty	pmCherry-Hyg-Cm	ampicillin	modified RWM65 new fluorophore
RWM130	NMHCA-GFP1	pAcGFP1-Hyg-Cm	ampicillin	NMHCII-A from RWM139 via pJet
RWM131	NMHCA-eGFP	pAcGFP1-Hyg-Cm	ampicillin	fluorophore/linker change in RWM130 (RWM139)
RWM132	MLCB-eGFP	pAcGFP1-Hyg-N1	ampicillin	MLC-eGFP in RWM 51
RWM133	pH2B-mCherry	IRES-puro2	ampicillin	addgene-21045
RWM135	pH2B-mCherry	pEFIRES-p	ampicillin	h2B-mCherry from RWM133 into RWM136
RWM136	empty	pEFIRES-p	ampicillin	from Marek Cebecauer
RWM137	Lifeact-mCherry	pEFIRES-p	ampicillin	Lifeact-mCherry from RWM98 into RWM133
RWM139	eGFP-NMHCA	pEGFP-C3	kanamycin	addgene-11347
RWM140	eGFP-NMHCB	peGFP-C3	kanamycin	addgene-11348
RWM142	pEGFP-Lifeact	pAc-GFP1-Hyg-N1	ampicillin	formerly RWS797
RWM155	pmCherry-MLCB	pEFIRES-p	ampicillin	pmCherry-MLCB from RWM156 into RWM135
RWM156	pmCherry-MLCB	pmCherry-Hyg-N1	ampicillin	MLCB via PCR into RWM124

Table 2.2: List of used and cloned plasmid constructs

2.1.5 Plasmid constructs not inserted in RWM list

Name	insert	Vector	Source/Cloning
pAc-GFP-βactin-Hyg-Cm	GFP-β-actin	RWM65	by C.Klingner
YFP-Rac1	YFP-Rac1	eEYFP-C1	addgene 11391
YFP-Rac1-N17	YFP-Rac1-T17N dom.negative	eYFP-C1	addgene 11395
YFP-Rac1-L61	YFP-Rac1-Q61L const.active	eYFP-C1	addgene 11401
pcDNA-eGFP-RhoA-wt	eGFP-RhoA-wt	pcDNA3-eGFP	addgene 12965
pcDNA-eGFP-RhoA-T19N	eGFP-RhoA-T19N dom.negative	pcDNA3-eGFP	addgene 12967
pcDNA-eGFP-RhoA-Q63L	eGFP-RhoA-Q63L const.active	pcDNA3-eGFP	addgene 12968
pmCherry-Rac1-Hyg-Cm	pmCherry-Rac1	RWM125	by G.Beck
pmCherry-Rac1-T17N-Hyg-Cm	pmCherry-Rac1-T17N	RWM125	by C.Klingner
pmCherry-Rac1-Q61L-Hyg-Cm	pmCherry-Rac1-Q61L	RWM125	by C.Klingner
pmCherry-RhoA-wt-Hyg-Cm	pmCherry-RhoA-wt	RWM125	by G.Beck
pmCherry-RhoA-T19N-Hyg-Cm	pmCherry-RhoA-T19N	RWM125	by G.Beck
pmCherry-RhoA-Q63L-Hyg-Cm	pmCherry-RhoA-Q63L	RWM125	by G.Beck

Table 2.3: List of cloned plasmid constructs not in RWM list

2.1.6 List of used Primers

Subsequent primers have been used for PCR reactions at a concentration of (1μM) or for DNA sequencing at a concentration of (5pM).

name	sequence	description
RWS229	gatcctgcagtttaaatcaatttgtaatagcttatttgg	Abp140-3'-1000-PstI
RWS927	ccagctcgaccaggatgg	3'-EGFP-seq
RWS1227	ccattgacgcaaatgggcg	5'-CMV-seq-pEGFP-N
RWS1415	gcaagtaaaacctctacaaatgtgg	3'-Seq-fori
RWS1432	ccttacaagaacctgccc	5'-NMHCII-A-1
RWS1433	gggcatcccagaagagg	5'-NMHCII-A-2
RWS1434	ggttccccaaagccacc	5'-NMHCII-A-3
RWS1435	ccagggcttccccaac	5'-NMHCII-A-4
RWS1436	caggaattagaagagatctgcc	5'-NMHCII-A-5
RWS1437	ggaagacctggagtctgag	5'-NMHCII-A-6
RWS1438	gaagctgagcctgagcac	5'-NMHCII-A-7
RWS1439	ccctagagcagcaggtg	5'-NMHCII-A-8
RWS1499	cgaactcgtgtccgttg	3'-mRFPruby-Sequencing
RWS1629	cttaagagcgcctgtgctatgtc	5'-AflII-Mars

RWS1630	cttaagggagctggagctggtgcaatgggcaagcttaccatg	5'-AflII-Mars-v2
RWS1631	tgcaccatctgtcactctgttaacctc	5'-MGSO
RWS1632	gggagcaaacaggattagataccct	3'-GPO
RWS1701	caggaaacagctatgac	3'-M13-rev
RWS1816	acgagaagcgcgatcacat	5'-GFP-seq-C-term
RWS1863	cacggggacgtggttttcc	5'-puro-check
RWS1930	actgtcgacatggcacagcaagctgccgataag	5'-SalI-MHCIIA-for
RWS1931	actgcggccgcttattcggcaggtttggcctcagc	5'-NotI-MHCIIA-rev
RWS2011	atcaagcttatgtcgagcaaaaaagcaaagaccaagacc	5'-MLCB-HindIII
RWS2012	atcgtcgaccagtcatctttgtctttcgctccgtgc	3'-MLCB-SalI
RWS2013	atcgctagcgctaccggtcgccacc-atggtgagcaagggcgaggagc	5'-paGFP-MCSpart
RWS2014	atcagatctgagtccggaacctcctccacc-cttgtacagctcgtccatgccgagagt	3'-paGFP-MCSpart

Table 2.4: List of used primers

2.1.7 Enzymes and proteins

Enzyme/protein	Source
Bovine serum albumin	Sigma
Phusion DNA Polymerase	Finzymes
Restriction enzymes	New England Biolabs
Taq DNA polymerase	New England Biolabs
Taq DNA polymerase	Core facility MPI Biochemistry
T4 DNA ligase	New England Biolabs

Table 2.5: List of used enzymes and proteins

2.1.8 Chemicals and reagents

Description	Source
Acetic acid	Sigma
Agarose	Invitrogen
Ampicillin	Carl Roth GmBH
Alexa Fluor 488 phalloidine	Invitrogen
Alexa Fluor 568 phalloidine	Invitrogen
Ampicillin sodium salt	Carl Roth GmBH
ATP	Sigma
Bapta-AM	Life Technologies
Bapta-AM	Sigma
Blebbistatin	Sigma

BM-Cyclin	Roche
Bradykinin	Sigma
Calyculin A	Sigma
Dabco	Carl Roth GmBH
Dimethyl sulfoxide (DMSO)	Sigma
Dimethyl sulfoxide (DMSO)	EuroClone
Deosynucleotide solution mix	New England Biolabs
Difco Bacto Agar	Becton Dickinson
Difco Bacto Tryptone	Becton Dickinson
Difco Yeast Extract	Becton Dickinson
DTT	Fermentas
dNTP set, 100mM solution	Fermentas
EDTA (Titriplex)	Merck
EGTA	Carl Roth GmBH
Gadolinium cloride hexahydrate	Sigma
Geneticin	Carl Roth GmBH
Gene Ruler^{TM}DNA ladder mix	Thermo Scientific
Gelatin	Sigma
Glutaraldehyde	Alfa Aesar
Glycerin 86% (w/v)p.a.	Carl Roth GmBH
Hygromycin B	Roche
Incidin Spezial	EcoLab
Ionomycin	Sigma
Latrunculin A / B	Enzo
Lipofectamine 2000	Invitrogen
Mowiol	Carl Roth GmBH
dNTP set, 100mM solution	GE Healthcare
Paraformaldehyde 37% (w/v)	Alfa Aesar
Penecillin/Streptomycin	PAA
Puromycin	Sigma
Saponin	Sigma
Sodium chloride	Merck
SDS	Carl Roth GmBH
Tris-HCl	Merck
Rhodamine-phalloidine	Invitrogen
Triton-X-100	Carl Roth GmBH
Trypsin-EDTA	PAA
Y27632	Sigma

Table 2.6: List of chemicals and reagents

2.1.9 Buffers and solutions

All subsequent buffers and solutions were provided by Technical Assistent G.Beck.

Description	Recipe
Alexa488-phalloidine staining solution	6.6μM alexa-phalloidine in methanol
Ampicillin solution	10mg/ml Ampicillin in sterile ddH_2O
6xLoading Dye	50% (w/v) sucrose 0.25%bromphenol-blue in TE buffer
EDTA solution pH8.0	0.5M EDTA Na_2EDTA x 2H_2O pH 8.0
Geneticin solution	200mg/ml Geneticin in sterile ddH_2O
Hygromycin B solution	50mg/ml Hygromycin in sterile PBS
10xLigase buffer	50mM $MgCl_2$ 660mM Tris-HCl 10mM DTT 10mM ATP pH7.5
Kanamycin solution	25mg/ml Kanamycin in sterile ddH_2O
10xPBS buffer	92mM NaH_2Po_4 147mM K_2PO_4 27mM KCl 1.39M NaCl pH7.2
Puromycin solution	1mg/ml in sterile ddH_2O
Potassium phosphate buffer (10x)	1M KH_2PO_4 pH7.0
rhodamine-phalloidine staining solution	6.6μM rhoadmine-phalloidine in methanol
10xTBS buffer	50mM TrisHCl 150mM NaCl pH7.5
10xTBE buffer	440mM Tris Base 440mM Boric Acid 10mM EDTA pH8.0
10xTBS buffer	50mM Tris-HCl 150mM NaCl pH7.5
1M Tris buffer	619mM Tris-HCl 38mM Tris Base pH8.0

Table 2.7: List of buffers and solutions

2.1.10 Media and plates

Bacterial media and plates

Bacterial media and plates were provided by Technical Assistant G.Beck.

Description	Recipe
LB medium	1% (w/v) Bacto tryptone 0.5% (w/v) Bacto yeast extract 0.5% (w/v) NaCl in sterile ddH_2O
YT medium	0.8% (w/v) Bacto tryptone 0.5% (w/v) Bacto yeast extract 0.5% (w/v) NaCl in sterile ddH_2O
YT plates	0.8% (w/v) Bacto tryptone 0.5% (w/v) Bacto yeast extract 0.5% (w/v) NaCl 1.5% Agar in sterile ddH_2O

YT plates + Ampicilline	0.8% (w/v) Bacto tryptone 0.5% (w/v) Bacto yeast extract 0.5% (w/v) NaCl 1.5% Agar in sterile ddH_2O + 100μg/ml Ampicillin
YT plates + Kanamycin	0.8% (w/v) Bacto tryptone 0.5% (w/v) Bacto yeast extract 0.5% (w/v) NaCl 1.5% Agar in sterile ddH_2O + 40μg/ml Kanamycin

Table 2.8: List of bacterial medium and plates

Mammalian medium

All mammalian medium was bought from LifeTechnologies^{TM}Gibco company.

Description	Catalog-No.
DMEM(1x)-GlutaMax^{TM}-I	31966-047
Fetal Bovine Serum	10270
HBSS (with calcium/ magnesium)	14025-092
HBSS (no calcium/ magnesium)	14170070
EpiLife®	11187-10
Opti-MEM®	13985-047

Table 2.9: List of used mammalian medium

2.2 Molecular Biology Protocols

2.2.1 E.coli culturing

E.coli strains were cultured using YT plates or in liquid using shaker at 200rpm at 37°C. For plasmid extraction, culture was grown over night in YT medium. Strains were stored for short times on plates at 4°C or as glycerol stock in 50% glycerol at -80°C.

2.2.2 Transformation of E.coli

50-100μl of rubidium chloride competent *E.coli* cells were thawed on ice before 5μl DNA-plasmid (about 1μg DNA) premixed with 5 μl ddH_2O or ligation mix were added. Mixture was incubated on ice for 30 minutes followed by a heat shock at 42°C for 2 minutes. Subsequently cells were incubated on ice for another 2 minutes before 150 μl of YT was added to cells. Mixture was incubated at 37°C for 30 minutes followed by plating the cells out on YT plates containing the appropriate selection marker ampicillin or kanamycin. Plates were incubated over night at 37°C.

2.2.3 Restriction Digest of DNA

For restriction digests of double stranded DNA restriction endonucleases (New England Biolabs, NEB) were used in combination with recommended buffer solutions NEB 1-4. Digests were incubated at 37°C for 1-3 hours prior to separation or analysis on TBE-agarose gel electrophoresis.

2.2.4 Ligation of DNA fragments

Double stranded DNA was ligated using T4 DNA ligase by NEB. Linear inserts were ligated to open linear backbone vector DNA strand at molar ratios of vector to insert between 1:3, 1:5 or 1:10. Reaction was incubated for 1 hour at room temperature. Reaction mixture protocol as follows:

Reagent	Volume
linearized vector	50-100ng
insert DNA	3/5/10 times equal molar amount of vector
T4 DNA ligase	$\sim$ 1 unit
10x ligase buffer	1μl
ddH_2O	added to 10μl total volume

Table 2.10: Table of DNA ligase reaction

2.2.5 Agarose gel electrophoresis

Separation and analysis of fragmented DNA was achieved by performing gel electrophoresis. Agarose gel was prepared at concentration of 1% agarose in 1xTBE buffer. For small DNA fragments agarose gel was prepared at concentration of 1.5-2% agarose in 1xTBE buffer. 1:8000 ethidium bromide was added to liquid agarose gel for intercalating into DNA strands making visualization under UV lamp possible. DNA samples were mixed with 20% volume of 6x DNA loading buffer and pipetted into agarose gel pockets. Subsequent separation was achieved by applying electric field within 1xTBE buffer at 90-120 Volt for 15-25 minutes. Gel bands were visualized using GeneFlash gel imaging system (Syngene BioImaging).

2.2.6 DNA sequencing

All DNA sequencing was performed by the Core facility of the MPI Biochemistry on ABI Big Dye 3.1 sequencing chemistry and ABI-3730 (Perkin Elmer) setup. For DNA sample preparation, following mixture was prepared to total volume of 7.5μl:

Reagent	Volume
DNA plasmid	2μl (300ng)
Sequencing primer	1μl (1:10 diluted in ddH_2O - 5pM)
ddH_2O	4.5μl

Table 2.11: Table of DNA sequencing sample preparation

2.2.7 Polymerase chain reaction - PCR

Polymerase chain reaction (PCR) was used to amplify DNA fragments. The PCR reaction requires one 5'-primer and one 3'-primer targeting the beginning and end of the amplification DNA cassette. The reaction was carried out using a PXE 0.2 Thermal Cycler (Thermo Electro Corporation). Subsequently to PCR, products were analyzed by agarose gel electrophoresis.

Standard PCR protocol

To validate DNA insertion standard PCR was performed using standard Taq polymerase provided by the Core facility of MPI Biochemistry. This polymerase has an activity of 1000base pairs(bp) per minute though incorporated single DNA base errors were high at about 1:1000bp. PCR samples were prepared to final volume of 50μl as follows: The PCR

Reagent	Volume
10x Taq buffer	5μl
dNTPs	1μl (0.2mM)
primer 5'-forward	0.5μl (1μM)
primer 3'-reverse	0.5μl (1μM)
template DNA	1μl (300ng)
Taq-polymerase	0.5μl (2 units)
ddH_2O	41.5μl (to 50μl volume)

Table 2.12: Table of standard PCR sample preparation

reaction cycle was programmed as follows:

Step	Cycle	Time	Temperature
Initial denaturation	1x	10min	95°C
Denaturation		30sec	95°C
Annealing	35x	30-60sec	56°C
Elongation		1min-3min	72°C
Final elongation	1x	10min	72°C
Storage	1x	∞	4°C

Table 2.13: Table of standard PCR reaction cycle

High Fidelity Phusion PCR protocol

To amplify insertion cassettes that should not have any included bp errors due to polymerase issues we used high fidelity Phusion®polymerase (New England Biolabs). The polymerase has a 50 fold higher fidelity compared to Taq polymerase and an activity of about 1000bp/30seconds. Reaction mixture and cycle were adopted accordingly to 50μl total volume:

Reagent	Volume
5x Phusion®HF reaction buffer	10μl
dNTPs	1μl (0.2mM)
primer 5'-forward	0.5μl (1μM)
primer 3'-reverse	0.5μl (1μM)
template DNA	1μl (300ng)
Phusion®-polymerase	1μl (2 units)
ddH_2O	36μl (to 50μl volume)

Table 2.14: Table of Phusion®PCR sample preparation

The PCR reaction cycle was programmed as follows:

Step	Cycle	Time	Temperature
Initial denaturation	1x	5min	98°C
Denaturation	35x	60sec	98°C
Annealing		10-30sec	56°C
Elongation		15-30sec	72°C
Final elongation	1x	10min	72°C
Storage	1x	∞	4°C

Table 2.15: Table of Phusion®PCR reaction cycle

2.3 Cell Culture

2.3.1 Cell culture

Culturing and Passaging

All model cell lines were grown in 25cm^2 tissue culture flasks (Falcon Company) at 37°C and 5% CO_2 in Dubellco's Modified Eagle medium (DMEM-Glutamax^{TM}-I) supplemented with 10% fetal bovine serum (FBS). No penecillin/streptomycin was added to cell culture. Wildtype cells were grown without selection marker, all stable transfected cells were kept under selection pressure with corresponding selection antibiotic, 300-400μg/ml hygromycin (Roche) or 200-300μg/ml puromycin (Sigma). Cells were passaged to new flask at a dilution of 1:6 every 48-72 hours. For splitting cells, medium was discarded with vacuum pump, washed once with 1XPBS and treated with 1XTrypsin-EDTA for 15 minutes at 37°C. Detached cells were diluted with additional 3ml of DMEM and spun down at 2000rpm for 2 minutes in centrifuge. Supernatant was discarded, cell pellet dissolved in fresh DMEM and 1-2ml passaged to new 25cm^2 flask containing appropriate selection marker and DMEM medium.

Frosting - Defrosting

For frosting cells, cell pellet after trypsination and centrifugation step was diluted in 1ml 90%FBS 10%DMSO mixture and frozen at -80°C in cryo-tubes. For defrosting cells, the aliquot was warmed to 37°C for 1-2 minutes in water bath. Subsequently, 1ml of DMEM was added and cells spun down at 2000rpm for 2 minutes. Supernatant was discarded, the cell pellet diluted in 6ml DMEM and passaged to 25cm^2 flask with appropriate selection marker.

Transient and stable transfection

For **transfection procedure**, cells were seeded at 10.000-100.000 cells in 12 well plates 24 hours prior to transfection. The transfection procedure was conducted as in the provided protocol of Lipofectamine 2000 (LF2000) using 2-3μg of DNA, premixing steps of DNA and LF2000 in 100μl Opti-MEM medium, mixture of both samples and incubation for 30 minutes at room temperature, and finally adding DNA-LF2000 mix to cells priorly washed once with Opti-MEM and kept in Opti-MEM for 4 hours at 37°C. Afterwards cells were washed twice with 1xPBS and incubated in DMEM for 24 hours.
For **transient transfections**, cells were then passaged to 8-well μ-slide ibidi dish or 35mm μ-ibidi-bottom dish for further analysis under microscope within 24-48 hours.
For **stable transfection**, cell were passaged after 24 hours of incubation post transfection to 10 cm culture dishes, incubated for further 24 hours and subsequently treated with appropriate amount of selection marker for up to 2 weeks. Medium was changed every three days. After cell death of all untransfected cells due to antibiotics treatment and growth of small cell clone colonies, clone colonies were scraped of the culture dish with 1ml pipette and passaged to 24well or 12 well culture dish. Afterwards, cell clones were amplified in cell number and passaged to 6 well dish, and finally to 25cm^2 flask. Clones were characterized using

fluorescence microscopy to discard clones exhibiting phenotypic effects or low fluorescence signal.

2.3.2 Preparation for microscopy

For **imaging** of non-confluent cells, 200μl of cells were seeded in 8-well μ-slides (ibidi) or 500μl in 35mm μ-ibidi-bottom dish at a concentration of 2x10^4 cells per ml. Cell density was determined using a Neubauer counting chamber. Cells were always imaged 48 hours after seeding. For observation of confluent monolayers, cells were seeded at 4-5x 10^5 cells/ml. Cells were incubated for 3-4 days before imaging.
For **wound healing assays**, 6x10^4 cells were seeded on both sides of a 35mm μ-dish wound healing culture insert (Ibidi) and incubated for 24 hours. After removal of insert, cells were again incubated for 12-24 hours and subsequently imaged.
For **shear flow experiments**, 5x10^3 cells were seeded in μ-slide$^{0.2}$ Luer flow chamber (Ibidi), incubated for 48 hours and afterwards connected to the Ibidi pump system with perfusion set containing DMEM medium. Pump and medium reservoir were kept at 37°C. Cells were then subjected to 20dyn/cm^2 oscillatory shear stress at 0.2Hz.
For **fibronectin coated pattern experiments** 2x10^4 cells were incubated in DMEM for 24 hours in Cytoo^{TM}chamber (Cytoo^{TM}) mounted with 20x20mm STARTERS CYTOOchip containing four micropattern geometries at various dimensions.

Drug treatments

For drug experiments cells were prepared as for normal non-confluent cells (preceding section) with 200μl in 8-well μ-slides (ibidi) at a concentration of 2x10^4 cells per ml. For drug treatment appropriate amount of drug was premixed in additional 100μl DMEM medium at 37°C for a final volume of 300μl. For imaging, cells were mounted to microscope, control cells measured, warmed premix was added to one 8-well dish and subsequently measured. For long time incubation of drugs, premix was added to one 8-well and then incubated at 37°C for defined time before imaging.

2.3.3 Antibody/phalloidine staining and western blot analysis

All antibody stainings and Western blot analysis were performed by group member Dr. A.Aufschnaiter. Phalloidine staining was performed by C.Klingner.

Antibodies for immunoflourescence and western blot analysis were: rabbit anti non-myosin IIA (Novus Bio NB600-1083) and mouse anti non-muscle myosin IIA antibody (Abcam ab55456). The antibodies were obtained from the Developmental Studies Hybridoma Bank developed under the auscpices of National Institute of Child Health and Human Development, and maintained by the Department of Biology at the University of Iowa (Iowa City, IA) (Ref.[79]).

For immunofluorescence stainings, cells were grown on glass coverslips, fixed with 3.2% paraformaldehyde in 1xPBS for 20 minutes, washed in PBS, permeabilized in 0.3% Triton-X

100 in 1xPBS for 5 minutes, and blocked with 1.25% gelatin and 0.05% saponin in 1xPBS for 20 minutes before incubation with primary antibody for 1 hour. After washing in PBS and incubation in secondary antibodies (Alexa-Fluor®goat anti-rabbit/mouse, Invitrogen A11008/A11029) for 1 hour in 1.25% gelatin and 0.05% saponin in 1xPBS, cells were washed again in 1xPBS before mounting in Mowiol/Dabco (Roth)(Ref.[79].

For phalloidine stainings, cells were fixed in 4% paraformaldehyde in 1xPBS for 30 minutes at room temperature. Subsequently, cells were incubated in 0.1% Triton-X 100 in 1xPBS for 2 minutes, subsequently washed once in 1xPBS and 2U of Alexa488-phalloidine (66nM) or rhodamine-phalloidine (66nM) were added premixed in 1xPBS for 1 hour. Cells were afterwards washed three times using 1xPBS and subsequently kept in 1xPBS for further analysis and imaging.

For western blot analysis, equal amounts of cell lysates were separated by SDS-Page, transferred to Immobilon^{TM}-P-membrane (Serva), blocked and afterwards incubated in primary antibody in the presence of 5% skim milk in TBS-T over night and labeled with HRP-coupled secondary antibody (Ref.[79]).

2.4 Microscopy

2.4.1 Standard bright field/epifluorescence cell imaging

For standard check of cell culture, cell counting during passaging, as well as for basic checks against possible phenotypical characteristics we used a standard Zeiss AxioVert 40 CFL inverted microscope equipped with white light source and 10x A-Plan Zeiss objective. The microscope was additionally equipped with filter sets for detection of green and/or red fluorescence and a mercury short arc lamp (HBO) mounted in a HBO50 power supply attached to the microscope to supply white light for basic fluorescence microscopy. This setup was therefore used to basic tests of flourescence signal existence during stable transfection procedure.

2.4.2 Scanning electon microscopy sample preparation

For scanning electron microscopy (SEM), cells were incubated for 45 minutes in 0.1M potassium phosphate buffer containing 2.5% glutaraldehyde. After three subsequent washing steps in 0.1M phosphate buffer, each 10 minutes long, cells were dehydrated by successive steps of incubation in 20-40-60-80-99% ethanol (EtOH, 99% Sigma). Each step endured 10 minutes. Cells were subsequently kept in 99% EtOH over night. For further dehydration and ethanol-CO_2 exchange, a critical point dryer (CPD; Polaron E3000) was used along with standard drying protocol. Cell surface was then sputter-coated with gold (Cressington 108auto) to a total thickness of 6nm gold and imaged either on a TopconSM300 SEM at 10-15kV or on a LEO DSM 982 SEM at 8kV.

2.4.3 Combined AFM fluorescence microscopy

For combined atomic force and fluorescence microscopy of live cells we used as AFM a Nanowizard III setup of JPK company with an integrated fluid chamber to measure live cell behavior. As cantilever we used 1μm polystyrene microsphere cantilevers of Novoscan company. The AFM setup was mounted to a standard high resolution Leica SP8 TCS inverted confocal fluorescence microscope equipped with a 63x immersion oil objective of Leica. Details regarding combined setup and force curve analysis performed within the collaborating group of Prof. H.Oberleithner can be found in J.Fels *et al.* (Ref.[33]).

2.4.4 Widefield fluorescence Microscopy

For fluorescence microscopy we utilized two prototypic setups of FEI/Till Photonics company being setup as total internal reflection fluorescence (TIRF) microscopes. For wide field fluorescence microscopy we set the TIRF angle to 0° in center position resulting in the standard wide field beam progression. The components of the two setups are listed below:

Component	Supplier	Description
Microscope core unit	Till Photonics	iMIC stand unit (inverted)
Objective lense	Olympus	Olympus 1.45 NA 100x (oil)
Control unit	Till Photonics	ICU
TIRF angle control	Till Photonics	Galvanometer-drive 2-axis scan head
Excitation laser 1	Coherent, Saphire	DPSS laser 75mW at 488nm
Excitation laser 2	Cobolt, Jive	DPSS laser 75mW at 568nm
Light source DIC	Till photonics	LED lamp
Light source epi-fluorescence	Till Photonics	Polychrome unit with monochromator
Laser combiner/switch	Till photonics	AOTF unit
Camera 1	Andor	Andor iXON DU-897 EM CCD
Camera 2	Imago	Imago QE CCD
Climate control	MPI Biochemistry work shop	temperature control unit with heating block
Software	Till Photonics	Live-Acquisition

Table 2.16: Table of first widefield/TIRF microscope setup

The second microscopy setup was in the last three months of the thesis updated with a by Rapp OptoElectronic company supplied open beam pulsed ultraviolet laser for ablation experiments. Features of the novel ablation system will therefore appear in the following list. Most experiments of this thesis were performed on this microscope setup.

Component	Supplier	Description
Microscope core unit	Till Photonics	iMIC stand unit (inverted)
Objective lense 1	Olympus	Olympus 1.40 NA 100x (oil)
Objective lense 2	Olympus	Olympus 0.75 NA 40x
Control unit	Till Photonics	ICU
TIRF angle control	Till Photonics	Galvanometer-drive 2-axis scan head
Excitation laser 1	Cobolt, Calypso	DPSS laser 75mW at 491nm
Excitation laser 2	Cobolt, Jive	DPSS laser 150mW at 561nm
Light source DIC	Till photonics	LED lamp
Light source epi-fluorescence	Till Photonics	Polychrome unit with monochromator
Laser combiner/switch	Till Photonics	AOTF unit
Camera	Imago	Imago QE Sensicam CCD
FRAP unit	Till Photonics	third galvanometer controlled mirror (Polytrope)
Ablation laser unit	Rapp OptoElectronic	DPSL 355/14 laser ablation unit with controller box
UV laser	Rapp OptoElectronic	pulsed 355nm Yag laser/ 14mW average power/ 70μJ per pulse/ 200Hz frequence
Climate control	Solvent Scientific	Plexiglas^{TM}heating chamber/heater/ heat control unit adopted for iMIC stand
Software	Till Photonics	Live-Acquisition

Table 2.17: Table of second widefield/TIRF microscope setup with ablation setup

2.5 Image Processing and Analysis

2.5.1 Image filtering

Fiji usage

For image processing two different methods were used. For contrast-adjustment, image zoom for presentation purposes as well as for basic filtering procedures we used Fiji open source program (Ref.[149]). For simple image denoising, we used Fiji 'Subtract background' plugin with a pixel radius of 50.
For kymograph analysis we used Fiji by first defining a region of interest (ROI) line for a image sequence and subsequently used the line scan function 'Reslice' (Image→Stack→Reslice) without interpolation and output spacing of one pixel.
For projections of images, Fiji 'Image Calculator' (Processing→Image Calculator) was used

and images were projected using 'Max' operation for maximum projection.
For mean intensity measurements in FRAP experiments (chapter 4.7), ROI rectangles were defined according to (Fig. 4.10) and subsequently measured using 'Measure' function of Fiji (Analyze → Measure) with predefined measurement of 'mean gray value'. Obtained lists were subsequently analyzed using Origin8.0

Matlab based filtering

For more detailed image analysis we routinely filtered images using Matlab (Mathworks Inc., Natrick, MA) program based algorithms and functions. As the standard filtering procedure we used first a block matching 3D filter (BM3D), developed by Dabov *et al.* (Ref.[24]) and provided as function tool box in Matlab for denoising images. Block size was 5x5 pixels, images were normalized by its maximum intensity value before filtering, and Matlab program code as follows:

```
I_norm=(I_double/(max(max(I_double))));
[~,I_filtered]=BM3D(1,I_norm,5);
I_16uint = uint16(I_filtered .* 65535);
```

Second, we applied a local top-hat filter (radius 5 pixel). Program code:

```
R=5; SE = strel('ball', R, R, 0);
I_final = imtophat(I_16uint,SE);
```

For confocal microscopy images during combined AFM - fluorescence microscopy we had to adopt the filtering procedure, namely the filter parameters, due to different microscope resolutions. Filter program code as follows:

```
I_norm=(I_double/(max(max(I_double))));
[~,I_filtered]=BM3D(20,I_norm,50);
I_16uint = uint16(I_filtered .* 65535);
```

The subsequently applied local top-hat filter was changed to:

```
R=5; SE = strel('ball', R, R, 10);
I_final = imtophat(I_16uint,SE);
```

2.5.2 Matlab based actin structure analysis

In chapter 3.2.3 we present an automized image analysis approach to measure apical actin structure differences over time and position. We here present briefly the Matlab algorithm work flow.

Program step	Description ('Matlab functions')
Binarizing	'im2b' using 2 times mean image value as threshold
Thinning	'bwmorph(thin)' to obtain oject skeleton
Pruning	on pruning step -'bwmorph(endpoints)' to erase single pixel branches
Cleaning image	'bwmorph(clean)' to delete single pixel objects
Label objects	'bwlabel' to label all remaining objects in image
From here each labeled object is analyzed seperately	
Border check	check if object touches image border, if so discard
Elongation check	take only object when more than 5 pixels defined
Classification	classify if analyzed object is linear or branched using 'bwmorph(endpoints)'
Linear object	when linear then monitor length, persistence length (bending parameter) and classify in bent/ mixed/ straight class
Branched object	when branched object get longest linear core structure by iterative pruning steps until two endpoints followed by reconstruction of longest core structure using starting endpoints
Core structure analysis	analyze core structure by monitoring length, persistence length (bending parameter) and classify in bent/ mixed/ straight class
Output	output all parameters including number of measured objects (object density)/length distribution/classification distribution/ flag list monitoring amount of analyzed versus discarded objects

Table 2.18: Table of actin structure analysis algorithm workflow

Subsequently, all output data was further evaluated and statistically analyzed using Orign8.0 program. Flagging each program step to overview amount of discarded objects led to the finding that overall the mean analyzed objects number per time and position point was stable though object density changed (data not shown).

2.5.3 Pearson temporal image correlation analysis

Details regarding temporal image correlation analysis are presented in chapter 3.3.2. For temporal image correlation analysis we used the 'corrcoef' function of Matlab comparing the reference image with all subsequent images.

2.5.4 Signal correlation spectroscopy

For auto- and cross-correlation of signal traces (as presented in chapter 6-8) we used the 'cov' Matlab function the following way:

```
C=cov(signal1,signal2);
CorrCoeff=C(2)/(std(signal1)*std(signal2));
```

Time shifting and other implementations were build around this correlation function.

2.5.5 Optical flow analysis

We describe in detail the workflow and general function of optical flow calculation. We adopted an existing Matlab program code, developed from Visesh Chari, which is free to download at the Matlab Central server (FileID17500) under hyperlink:

```
http://www.mathworks.com/matlabcentral/fileexchange/17500-high-
accuracy-optical-flow
```

2.5.6 Statistics

All statistical analysis was performed using Origin8.0 (OriginLab Corp., Northampton MA, USA) analysis tools. For hypothesis testing we utilized a Students two-sample t-test for independent samples mean with null hypothesis ($mean_1 - mean_2 = 0$) and alternative hypothesis of ($mean_1 - mean_2 <> 0$) which relates to two-tailed two-sample t-test.

Chapter 3

Apical actin organization and dynamics

3.1 Introduction

The cytoskeleton is a key player in the detection, transmission, and generation of forces in mammalian cells. Three main components of the cytoskeleton fulfill the different tasks: (1) microtubules, (2) intermediate filaments, and (3) actin structures. While microtubules span the cytoplasm and are capable of resisting compressive stresses (Ref.[8]), intermediate filaments are assumed to act as mechanical stress absorbers (Ref.[54]). Actin structures, the third cytoskeletal component, are multifunctional. Various different actin structures are involved in mechanically stabilizing cells, generating and remodeling cell shape, as well as taking part in morphogenetic processes such as cell polarization, cell motility, and cell differentiation (Ref.[91]).

In the last decades a multitude of distinct cellular actin structures have been described. Filopodia (Ref.[150]), lamellipodia (Ref.[55]), stress fibers (Ref.[113]), cortical networks (Ref.[143]), endocytic actin patches (Ref.[36]) as well as podosomes and invadopodia are exemplary actin filament structures involved in crucial cellular processes. Actin filament assembly to bundles and networks and their linkage to the extracellular matrix or neighboring cells via adhesion structures give the cell the ability to control and remodel its shape. The required mechanical force for such processes is either generated directly by actin polymerization or through interaction with myosin motors (Ref.[92]).

Epithelial cells (ECs) organize into adherent groups forming boundary layers that define tissue compartments in multicellular organisms. As such boundaries the cell tissue layers must bear or generate significant mechanical stresses and forces, e.g. during organelle remodeling, growth or other developmental events. It is therefore of great interest to understand the structural, regulatory and dynamical aspects of cortical cytoskeleton organization that enable ECs to sustain or exert such forces.

Individual cells within the cell sheet monolayer are polarized along a basal-apical axis with distinct actin structures in different cellular regions. At the basal surface, actin forms stress fibers, antiparallel bundles of actin, that connect the cell to its substrate via focal adhesion complexes (Ref.[113]). The cortical actin network, a less defined meshwork of short actin filaments coupled to cortactin, occludin, ZO 1-3 and other important membrane-actin associating proteins is localized in the cortical region between the basal and apical zone. The meshwork mechanically couples cellular tight junctions and crucial cell-cell connections with other parts of the cytoskeleton and is thereby involved in signal transduction, transmembrane receptor

organization, membrane dynamics or paracellular ion transport (Ref.[175],[50]). Underneath the apical surface lies another very prominent actin structure in polarized ECs, the circumferential ring. This actin ring is linked to adherens junctions to stabilize cell-cell contacts and to provide the cells ability of force transmission within a cellular sheet (Ref.[50],[132]).

The apical surface of polarized epithelia is decorated by microvilli (MV). These membrane protrusions consist of actin filament bundles perpendicularly extending 1-3μm out to the cell surface. In fully polarized epithelia up to 15000 MV per cell are aligned next to each other (Ref.[27]) forming the typical brush border. The brush border MV are interconnected at their bases by a dense meshwork of actin, spectrin and myosins called the terminal web (Ref.[10],[56]).

In the following chapter, we use quantitative live-cell imaging to characterize the spatial organization and dynamics of MV in Madin-Darby canine kidney (MDCK) cells, a standard and widely used model cell line for polarized epithelia. We compare confluent to non-confluent cells regarding their MV distribution and behavior. We find that the apical surface of confluent cells is, as already described, covered by arrays of short and static MV. However, non-confluent cells differ significantly from the known classical situation as they exhibit highly dynamic protrusions. These dynamic protrusions are often more elongated, oriented parallel to the cell membrane rather than perpendicular and exhibit complex and spatially correlated patterns of reorganization. Using drug treatments we can deduce myosin II, the actin related motor protein, to be the driving force for the spatial reorganization.

3.2 Confluency depending actin structure differences

3.2.1 Fluorescence microscopy reveals actin structure differences

In order to assess the confluency dependent apical actin organization, MDCK cells were transfected with the f-actin marker Lifeact-GFP (Ref.[138]). While for confluent epithelial cells the commonly known dotted microvilli structure became visible (Fig. 3.1, left), performing single cell fluorescence microscopy (FM) on non-confluent cells revealed elongated actin structures (Fig. 3.1, right). Moreover, these elongated structures frequently appeared bent, interconnected and, in contrast to classical microvilli structures, parallel to the cellular membrane.

As usual for classical bright field microscopy a fair amount of background signal appeared in the images due to physical and biological reasons. On one hand, the large component of the point spread function (PSF) in the direction of z leads to additional fluorescence marker excitation close to the focus plane. On the other hand, non specifically bound fluorescence marker in the cytosol additionally increases the background signal artifact. To overcome background signaling we incorporated a Matlab based filtering process into all our analysis (see chapter 2.4). Moreover, we optimized the image acquisition procedure by scanning three focus planes per time point, each 1μm apart from each other. After filtering procedure, the three focus planes were maximum projected and color coded to obtain additional 3D information. Example images for confluent and non-confluent cells are depicted below(Fig. 3.2).

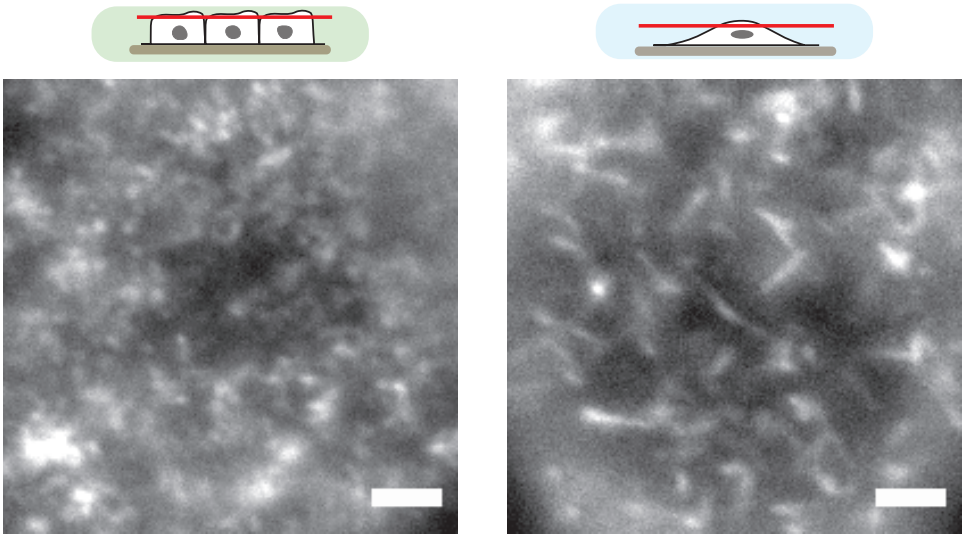

Figure 3.1: Single focal plane of apical actin organization of confluent (left) and non-confluent (right) cells labeled with Lifeact-GFP. non-confluent cells exhibit elongated and frequently bent membrane parallel actin structures. Scale bar: 2μm

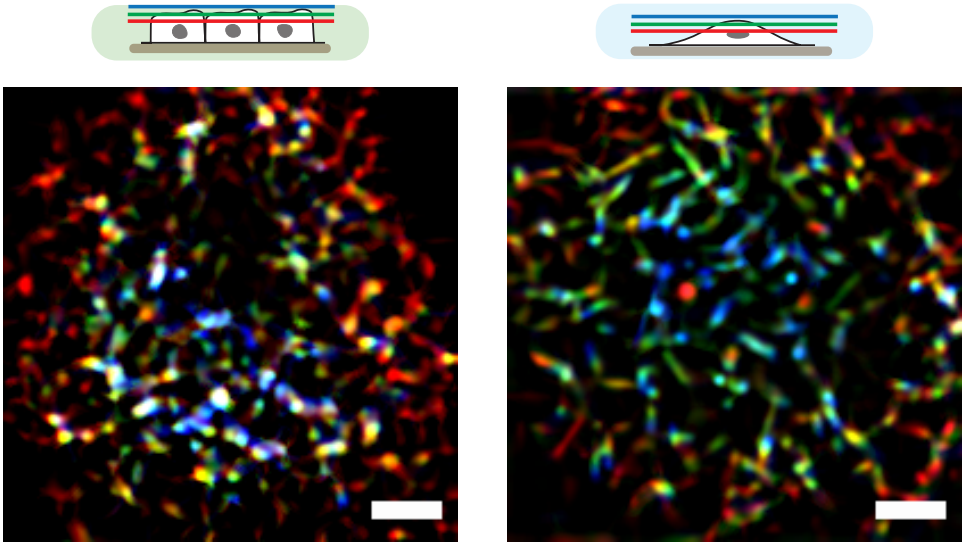

Figure 3.2: Color coded 3D image projections spanning approximately 1.5μm visualizes apical actin distribution for confluent and non-confluent cells and reveals distinct structural differences. Scale bar: 2μm

We color coded the focus plane closest to the substrate in red, followed by green and blue being the topmost focus plane (see schemes Fig. 3.2). For non-confluent cells the actin structures appeared elongated with continuously changing colors (Fig. 3.2 right) whereas the color coded images of confluent cells comprised multiple white spots (Fig. 3.2 left). The described white spots in this color overlay of all three basic colors resulted from structures localized at the same position in all three focus planes, leading to the presumption that these structures were actin filled microvilli perpendicularly sticking out of the apical membrane. Hence, non-confluent cells exhibited more elongated and membrane-parallel actin structures compared to confluent cells.

As control, we checked for possible artifact due to Lifeact-GFP in the cells. We confirmed the elongated actin structures by either expressing actin-GFP (Fig. 3.3 left) or by labeling f-actin in fixed cells using atto488-phalloidin (Fig. 3.3 middle). As an additional outcome of this control experiments, the comparison of non-confluent and confluent cells stained with phalloidin confirmed the structural difference of apical actin (Fig. 3.3 middle and right).

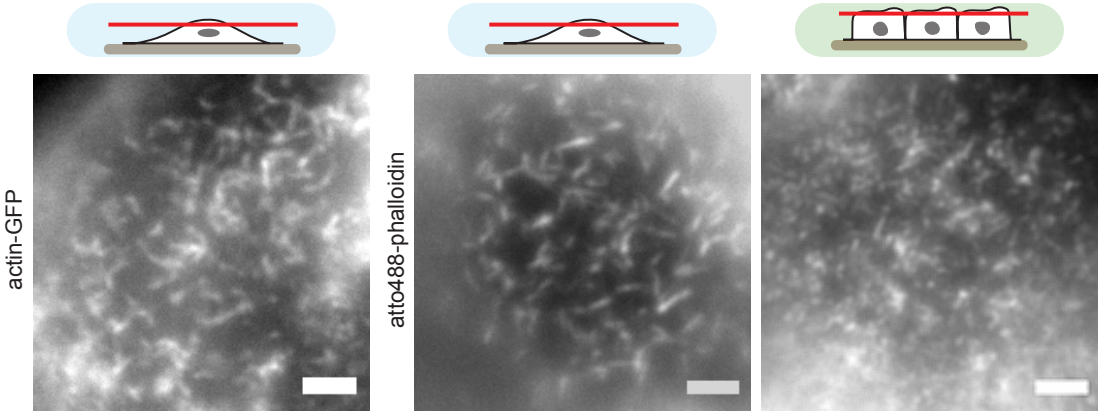

Figure 3.3: Control experiments using actin-GFP (left) or atto488-phalloidin (middle, right) confirm apical actin differences for non-confluent (left, middle) versus confluent cells

3.2.2 SEM analysis confirms topological differences

Comparing the fluorescence images of confluent to non-confluent cells led to the finding, that the apical actin structures can change significantly. However, we were puzzled by the question how the apical actin is located in non-confluent cells. Are the elongated actin filaments inside of the cell membrane, incorporated in the cellular membrane or are these microvilli-like structures protruding out of the cell?

To answer this question we performed scanning electron microscopy (SEM) to identify the apical actin localization. For cell fixation we used critical point drying (CPD) technique (e.g. Ref.[7]), which maintained the cell surface topology except for small drying artifacts (Fig. 3.4,

left). These freeze ruptures could probably be circumvented by optimizing the CPD protocol, e.g. by careful ethanol pre-drying steps and precise temperature control. However, the ruptures did not impede with the outcome of the experiments.

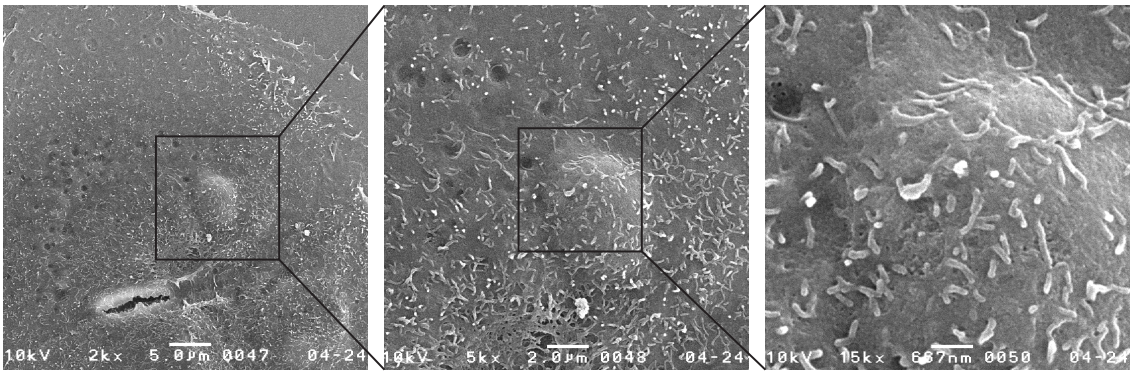

Figure 3.4: Exemplary result of CPD and gold sputtered cell surface of non-confluent cell visualized by SEM. Cell surface topology is maintained (middle, right) except for small freeze ruptures (left). Scale bar: 5μm (left), 2μm (middle), 667nm (right)

Using the standard fixation protocol we compared confluent and non-confluent cell topology. We thereby revealed that in both cases microvilli protrusions were present (Fig. 3.4 and 3.5). Hence, large parts of the fluorescent actin structures in non-confluent cells can presumably be related to microvilli-like structures.

We further wanted to clarify if the microvilli-like structures of non-confluent cells were protruding perpendicular from the cell membrane or if these structures were oriented parallel to the plasma membrane. We therefore reoriented the sample with respect to the electron beam to reach an inclination angle of $\alpha = 70°$. The comparison of confluent versus non-confluent cells revealed that in both settings a significant part of microvilli were oriented perpendicular to the membrane (Fig. 3.6) and additionally, a considerable amount of membrane parallel protrusions could be identified. We were unable to rule out the possibility that these membrane parallel structures resulted from fixation artifacts due to e.g. gold sputtering or critical point drying (see chapter 2.3).

To further investigate the orientation of the protruding actin based structures we optimized two crucial steps of the experiment. First, we changed the SEM and used a higher resolution microscope down to 100nm in cooperation with the LMU group of Prof. J.Rädler. Second, we optimized the CPD procedure by flushing seven times with liquid CO_2 and slowly changing pressure. These changes led to an apparent improvement of cell topology maintenance (Fig. 3.7). At a resolution of 100nm (Fig. 3.7, right) we could even identify single perpendicularly protruding microvilli in non-confluent cells that stabilized their perpendicular orientation by leaning against each other. Moreover, the ability of microvilli to form vesicles at their tip could be observed as proposed recently (Ref. [109]). Nevertheless, both perpendicular and

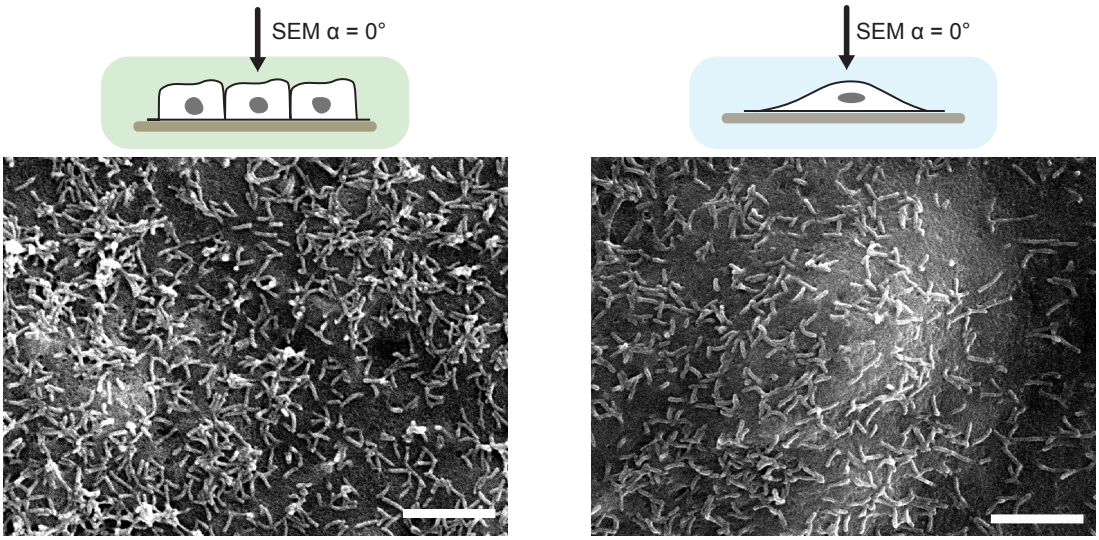

Figure 3.5: Comparison of cell surface topology of confluent (left) and non-confluent cell (right), imaged using SEM, reveals the presence of microvilli. Scale bar: 2μm

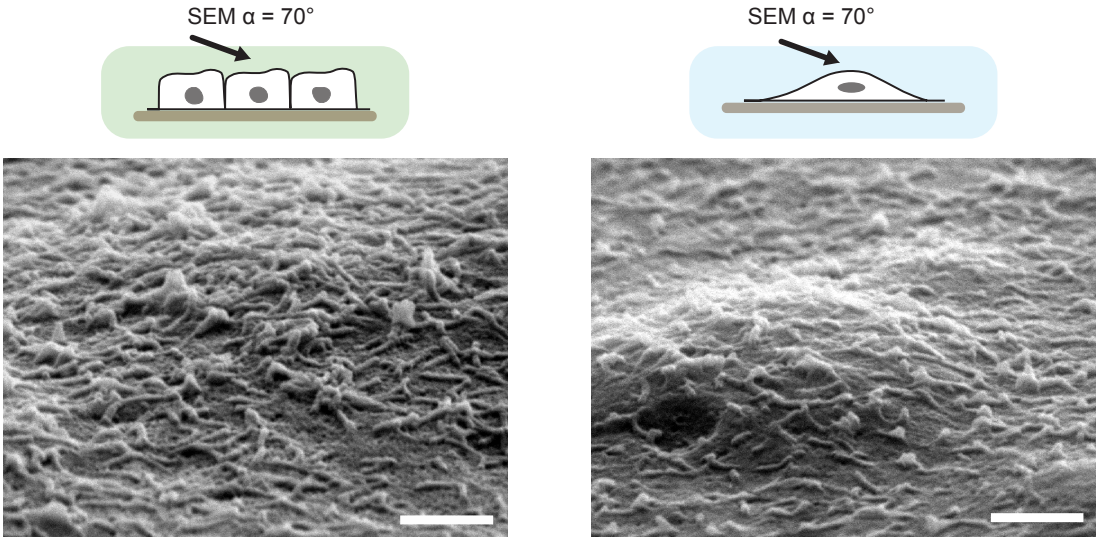

Figure 3.6: Inclined angle SEM analysis reveals microvilli for confluent (left) and non-confluent cells (right) that are protruding out of the cell surface as well as being membrane parallel oriented. Scale bar: 2μm

membrane parallel oriented microvilli protrusions were still visible (Fig. 3.7,middle). Hence, SEM experiments did not deliver the clarifying results regarding microvilli orientation.

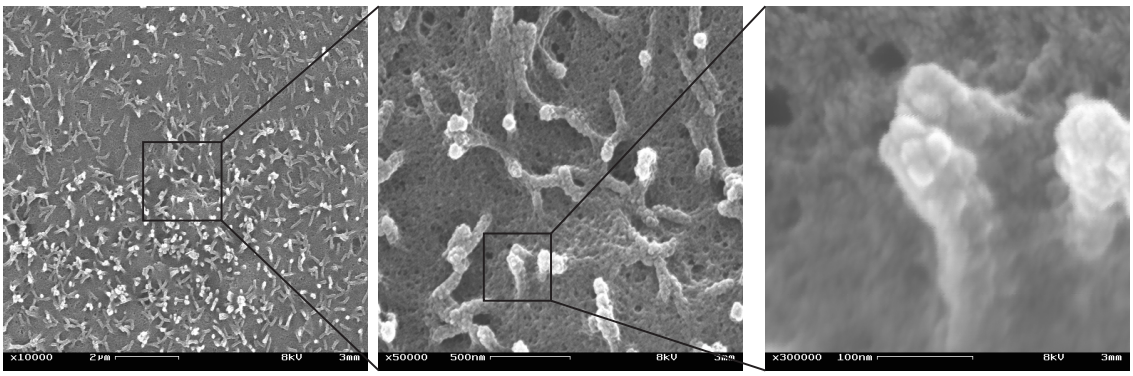

Figure 3.7: High resolution SEM images of non-confluent apical cell topology reveals that even after optimized fixation procedure perpendicular as well as membrane parallel microvilli protrusions are visible. Scale bar: 2μm (left), 500nm (middle), 100nm (right)

Apart from membrane orientation we observed distinct differences between confluent and non-confluent cells, namely the number of microvilli at the cell surface. As visible in Fig. 3.5, the amount of microvilli structures increased visibly when comparing cell surfaces after 48 hours (Fig. 3.8, left), 72 hours (Fig. 3.8, middle), and seven days after seeding (Fig. 3.8, right). We later confirmed this finding by a systematic screen using fluorescence microscopy with subsequent automatized Matlab based image analysis.

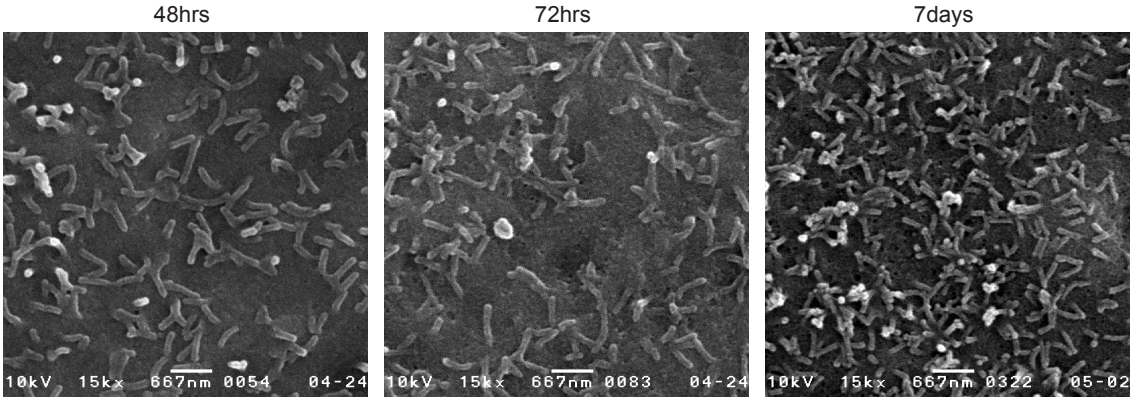

Figure 3.8: SEM images of cell surface topology from cells 48 hours (left), 72 hours (middle) or seven days (right) after cell seeding depict time dependent increase of microvilli. Scale bar: 667nm

We continued our topology analysis by measuring $n = 100$ microvilli structures using images of

five different cells at either confluent or non-confluent state. When comparing the confluency depending microvilli length, a slight but statistically significant increase in length was detected for non confluence related protrusions (Fig. 3.9, left). Moreover, we adopted the so called bending parameter (BP) which is usually used for polymer chain length description. The BP is defined as the end-to-end point length of a structure divided by its contour length:

$$\mathrm{BP} = \frac{\sqrt{(x_N - x_1)^2 + (y_N - y_1)^2}}{\sum_{i=1}^{N-1} \sqrt{(x_{i+1} - x_i)^2 + (y_{i+1} - y_i)^2}} \tag{3.1}$$

Here, x and y denote the respective pixel coordinates of the analyzed structure skeleton. We classified a BP smaller than 0.9 to be a bent structure. Considering this classification, non-confluent cells exhibited more bent protrusions compared to the number of bent microvilli of confluent cells (Fig. 3.9, right).

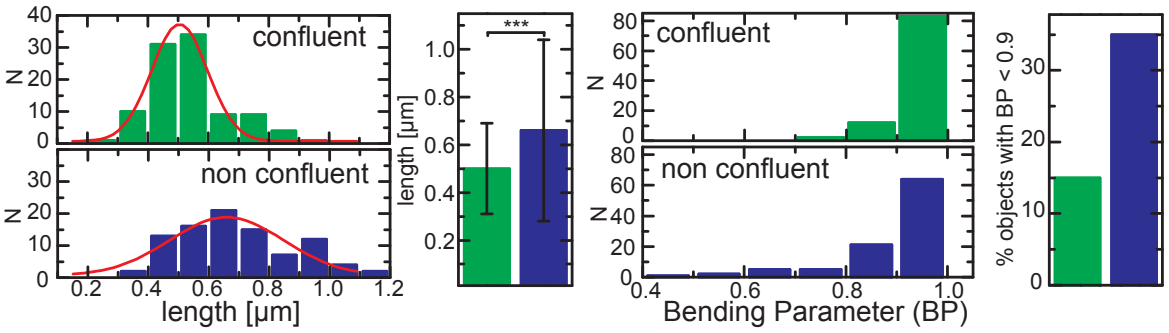

Figure 3.9: Length and bending parameter analysis of confluent versus non-confluent microvilli depicts difference in elongation and bending for microvilli of non-confluent cells.

In conclusion, the cell surface topology study using SEM revealed that both, non-confluent and confluent cells exhibited microvilli structures though non-confluent cells had significantly less apical protrusions that were more frequently elongated and bent.

3.2.3 Topological variations dependent on cell position and confluence state

Due to the outcomes of fluorescence images and SEM analysis regarding the confluency depending differences in microvilli object density and structure, we continued the characterization by conducting a systematic screen. For this purpose we monitored wildtype MDCK cells in 24 hours steps up to 96 hrs after cell seeding. At each 24 hour time point we fixed one cell containing 35mm Ibidi culture dish using the standard paraformaldehyde fixation procedure followed by atto488-phalloidin staining. For the subsequent image acquisition of the cells we categorized cells depending on their position into four classes (Fig. 3.10, left and middle): first class, single cells, second class, border cells of small cell islands (up to 50 cells), third class, cells of small islands completely surrounded by neighboring cells, and fourth class,

confluent cells of large cell islands (more than 50 cells). We accounted class one and two as non-confluent whereas class three and four were regarded as confluent situation.

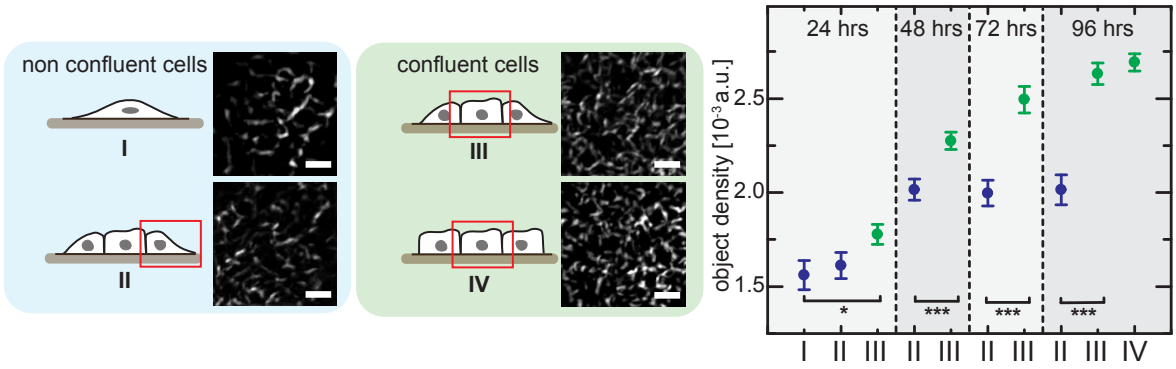

Figure 3.10: Position classification and large scale cell screen using automized object density detection to demonstrate cell position (left) and time after seeding (right) dependency

After maximum projection of three planes covering the apical region of each cell and normalization of the output by using only 200x200 pixel cut image parts (12.8x12.8μm) we performed the automized image analysis as described in chapter 2.5.2. Surprisingly, we found a clear correlation between the position as well as confluency to the microvilli object density (Fig. 3.10, right). While for the non-confluent cells of class one and two the amount of microvilli remained constant for 48 hours after a short increase within the first 48 hours after seeding (Fig. 3.10, right blue), we registered a constant increase of object density (number of identified objects over image surface) for confluent cells of class three and four (Fig. 3.10, right green). This result clearly indicated that the apical cell cortex topology is depending on the position of the cell as well as the existence and maturation state of cell-cell contacts.

Apart from the object density per cell we automatically analyzed in parallel three additional parameters of every object (chapter 2.5.2). As a first parameter, we calculated the BP of every object per frame. Subsequently, we calculated the mean BP_{mean} from all BP per frame and classified every frame into one of three categories depending on the predominantly present apical structures: strongly bent cell structures with $0 < BP_{mean} \leq 0.4$, mixed cell structures with $0.4 < BP_{mean} \leq 0.7$, or straight cell structures with $0.7 < BP_{mean} \leq 1$. Due to this categorization we were able to follow the change from frequently bent to straight microvilli arrangement. By calculating the relative percentages per dataset a steady increase of straight classified cell cortex structures from zero to over 20 percent was observable (Fig. 3.11, left cyan category). Moreover, non-confluent cells appeared to have more frequently strongly bent structures (Fig. 3.11,left black category) even though after 72 hours this tendency was not observable for unknown reasons.

Additionally, we registered two more parameters, namely the length and number of endpoints for each object (Fig. 3.11, right). Both parameters showed no significant changes for the whole

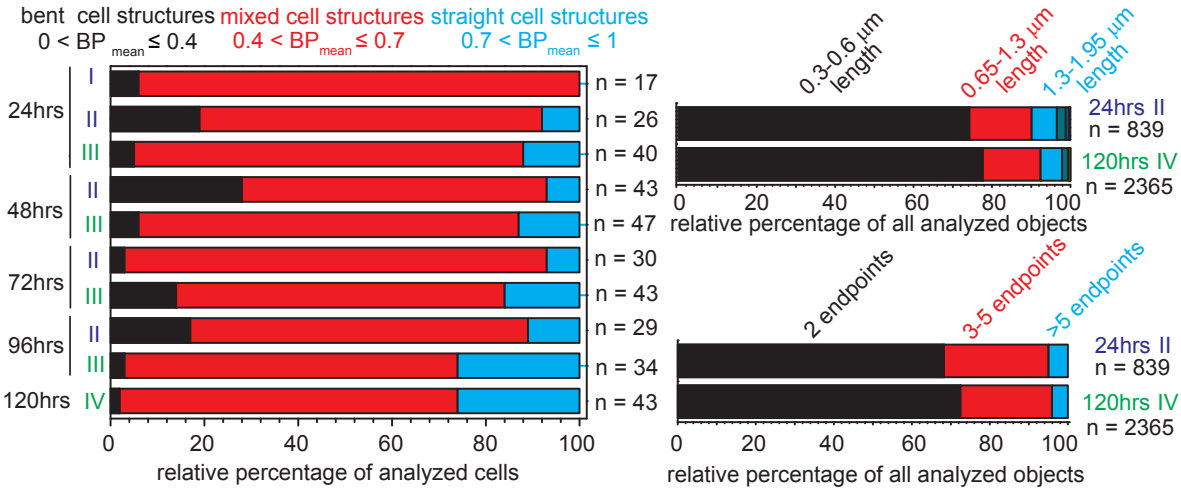

Figure 3.11: Mean bending, object length and number of object endpoints analysis demonstrating position dependent change of apical actin structures over time. n equals number of cell surfaces automatically analyzed (left) or number of objects (right).

time range as can be seen from the exemplary comparison of non-confluent cells 24hours posterior to seeding and at the edge of small islands (category II) with confluent cells after 120 hours. Over 90 percent of all objects were smaller than 1.3μm (Fig. 3.11, right upper) and more than 70 percent had no more than two endpoints (Fig. 3.11, right lower). Notably, the 100nm length difference we detected in the SEM data (Fig. 3.9) could not be determined by this light microscopy based approach due to the diffraction limit. Moreover, very stringent exclusion criteria regarding the automized analysis of objects, such as e.g. exclusion of detected objects smaller than five pixels, might have led to an additional loss of sensitivity in length measurement.

In conclusion, the systematic screening in combination with automized image analysis validated the finding, that the cell cortical microvilli number and topology changed depending on the position of the cell and the state of confluency which is directly correlated to the existence and maturation of cell cell contacts.

3.2.4 Oscillatory shear flow experiment illustrates membrane parallel microvilli arrangement

Having demonstrated the time and position dependent structural differences of non-confluent to confluent apical actin structures we retried to gain information about protruding versus membrane parallel microvilli now using light microscopy instead of SEM. We set up an oscillatory shear flow experiment using Ibidi flow chambers and the Ibidi pump system and seeded cells to mechanically interfere with the apical membrane. We switched the 20 dyn/cm^2 strong medium flow direction every 6 seconds and monitored two focal planes per time point with $\Delta t = 1$sec and $\Delta z = 2\mu$m.

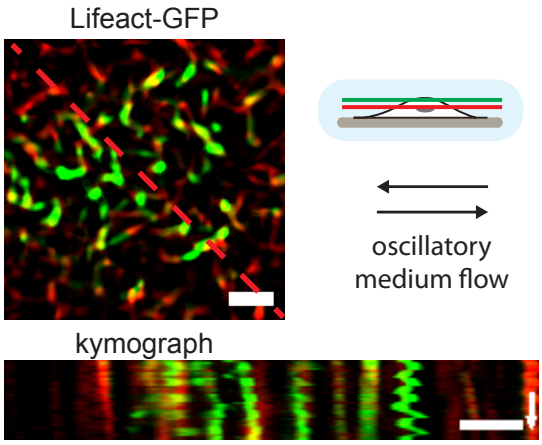

Figure 3.12: Oscillatory shear flow experiment demonstrates that parts of non-confluent microvilli structures are protruding from cell (green) thereby pivoting while other actin based structures remain static (red). Static structures presumably have membrane connection. Scale bar: 2μm, time arrow: 20sec.

Interestingly, the shear flow approach revealed that some parts of the microvilli-like structures were protruding out of the cell membrane, therefore pivoting back and forth upon medium flow direction change (Fig. 3.12, left and kymograph green), whereas large fractions of the apical actin structures remained static (Fig. 3.12, left and kymograph red). This finding indicated, more precisely than the previous SEM analysis, that large fractions of the apical actin were either membrane bound protrusions or these structures were even located within the cell though in close proximity to the membrane as microvilli-like precursors. Here, only high resolution transmission electron micrographs of apical sections could lead to a clarifying answer regarding the positioning of apical actin bundles. These experiments should be part of future investigations.

3.2.5 Wound healing and HGF experiments reveal a physiological relevance

In the previous sections we defined the confluency state by controlling the number of cells seeded before experiment (chapter 2.3.2). However, in the physiological context epithelial cells are usually forming confluent cell sheet monolayers (Ref.[117]) and are hardly ever present as small islands or single migrating cells only. It was therefore of high interest to check for the change of apical actin in the physiological situation of wound healing. If the results described above were correct then a scratch in a confluent cell sheet monolayer would have to result in a change of apical actin structures of migrating border cells at the scratch.

Even though the obtained results of such wound healing experiments were not as obvious as expected we could observe a change from dotted to more elongated apical actin structures when comparing the cell cortex of cells close to and away from the wound scratch (Fig. 3.13). Cells close to the scratch turned into migratory state with its typical actin based basal lamellipodia protrusions (Fig. 3.13, middle basal, arrows) (Ref. [126]). These migrating

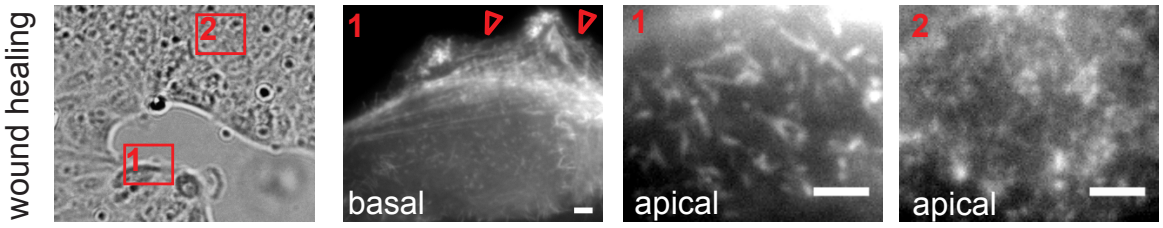

Figure 3.13: Physiological wound healing assay revealing apical actin structure change upon wound closure. Border cells at wound (1) exhibit elongated actin bundles and migration related lamellipodia at basal plane while cells away from wound have dotted confluent related actin distribution(2).

cells frequently exhibited the elongated microvilli structures related to non-confluent situation (Fig. 3.13, middle apical). In contrast, cells in distance to the monolayer scratch did not change their apical actin (Fig. 3.13, right).

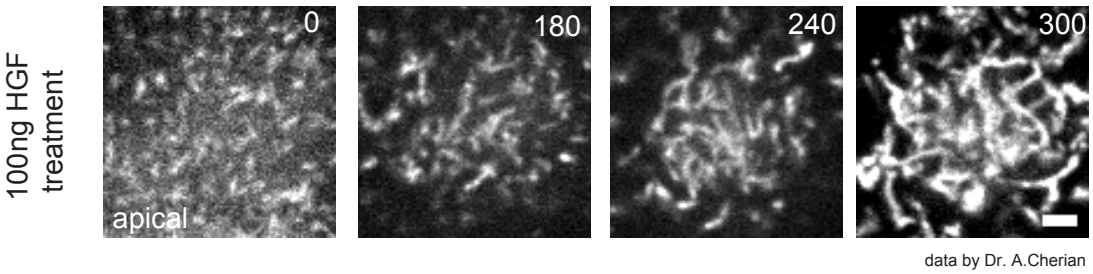

Figure 3.14: Dotted apical actin distribution of confluent cell (left) changes to highly elongated actin bundles upon HGF treatment (right). Scale bar: 2μm time in minutes (data acquired by Dr. A. Cherian).

In addition, we tested the change of apical microvilli structure in a drug experiment using hepatocyte growth factor (HGF). As HGF triggers the morphological change from epithelial to mesenchymal cell state (Ref.[165]) including increased cell motility we expected a change in microvilli structure (Ref. [68],[117]). Indeed, Dr. A. Cherian, a group member, could detect a significant effect on the cell cortical structure and behavior of HGF treated cells (Fig. 3.14). After five hours of 100ng HGF treatment, the apical actin structures were extensively elongated and appeared to have increased in numbers. As HGF is however known to interfere with multiple signaling pathways and changes the overall cellular behavior (Ref. [136]) we did not extend these drug experiments.

In conclusion, even in physiologically more relevant experiments on cell sheet monolayers compared to the artificial confluency dependence caused by varying seeding numbers of cells, the difference of apical actin structures was distinguishable. Moreover, HGF substantially influenced the actin based microvilli topology within five hours.

3.3 Confluency depending actin dynamics

3.3.1 Fluorescence time lapse movies reveal differences in apical actin dynamics

To continue the systematic comparison of confluent and non-confluent apical cell cortex organization we performed time lapse experiments using stably Lifeact-GFP transfected MDCK cells. Surprisingly, not only the apical actin structure changed upon increase of cellular confluency (chapter 3.2) but also its dynamical behavior exhibited distinct differences. We used kymograph analysis, a line scan (Fig. 3.15, red lines) per time point stacked to an image with time axis perpendicular to spatial position, for a first visualization of the dynamical differences. While for confluent cells the dotted actin structures exhibited only slow motion pattern and minimal spatial rearrangement (Fig. 3.15, left and kymograph), the membrane parallel and more elongated actin filaments on non-confluent cells underwent extensive cortical reorganization (Fig. 3.15, right and kymograph).

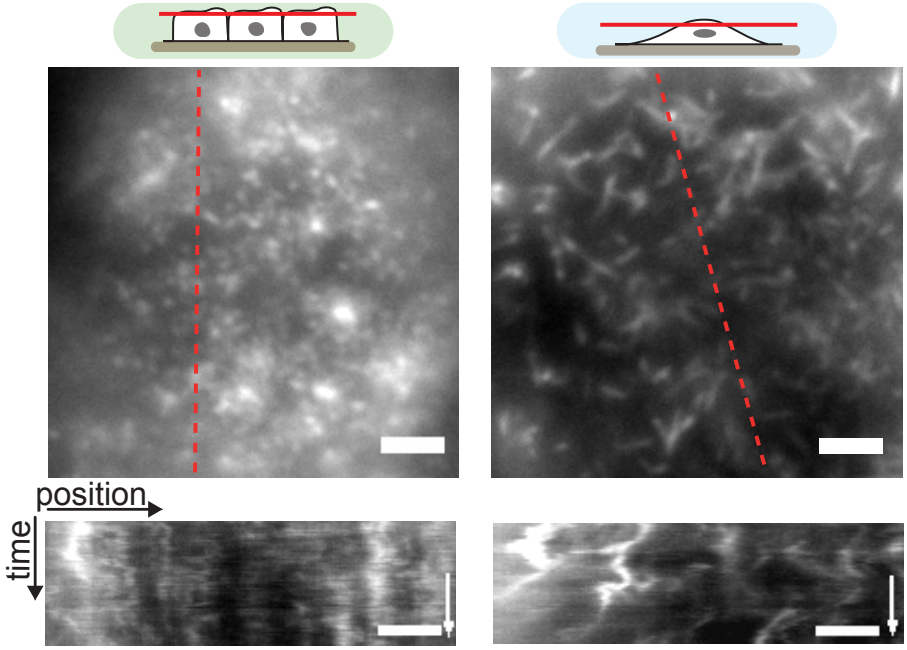

Figure 3.15: Distinct dynamical actin reorganization differences for static confluent (left) versus highly dynamic non-confluent cells (right). Kymographs depict dynamic variation. Scale bar: 2μm time arrow: 300 sec.

We set out to more carefully characterize the cortical actin dynamics using image analysis methods such as e.g. mean intensity tracking, object endpoint analysis and object center of mass tracking. However, with all these approaches we were unfortunately unable to characterize the dynamic behavior in detail. Key point for this lack of success was the highly dynamic reorganization of actin structures which made a large scale object based dynamics analysis impossible. Some of the constantly and simultaneously appearing morphological changes of the microvilli-like structures are depicted in Fig. 3.16. Apical actin structures frequently underwent bending (Fig. 3.16, first panel), fusion and rupture of filaments (Fig. 3.16, second

panel), pivoting of protruding microvilli (Fig. 3.16, third panel) as well as complete lateral translation of multiple actin structures within the cell cortex (Fig. 3.16, fourth panel). Especially fusion and rupture events led to severe problems using object based automized image analysis methods.

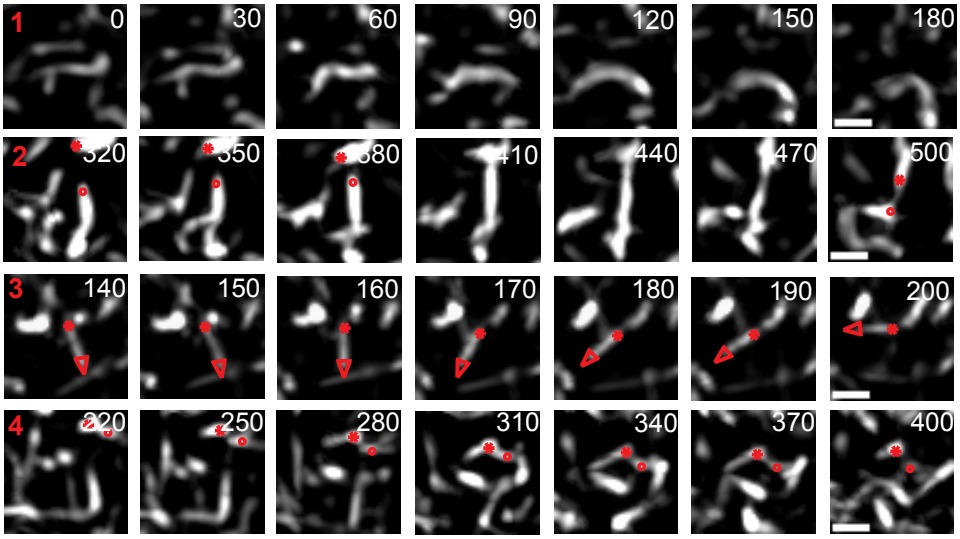

Figure 3.16: Morphological changes appearing during actin reorganization include bending (first panel), fusion and rupture (second panel), pivoting of protrusions (third panel), and lateral translation of actin structures (fourth panel). Scale bar: 1μm time in seconds.

3.3.2 Quantitative image correlation analysis maps actin dynamic differences

As all object based approaches to characterize apical actin dynamics failed due to the above mentioned problems we continued to analyze time lapse movies using various image correlation methods. These correlation methods are by now commonly used powerful tools in fluorescence microscopy to gain insights in temporal, spatial or spatiotemporal characteristics such as e.g. reorganization times, transport properties, co-localization of fluorophores and possible interactions of these components (Ref.[82]). The main advantage compared to other techniques is the pixel-wise intensity variation based analysis. Thus object predefinition or recognition is not a prerequisite for these approaches.

In the course of this thesis we mainly used Pearson correlation function (PCF) for analysis of temporal reorganization. Furthermore we used spatial correlation function (SCF) and temporal correlation function (TCF) (Ref.[3]) for the analysis of velocity vector fields obtained by spatio-temporal image correlation spectroscopy (STICS) (Ref.[53]). These STICS velocity field calculations as well as SCF and TCF analysis were conducted by Dr. P. Diesinger of the collaborating bioinformatics group of Dr. M. Bathe from Massachusetts Institute of Technology (MIT). All calculations and computer based results not obtained by me will be marked clearly throughout this thesis.

Pearson correlation analysis reveals dynamical differences

We first used in Matlab calculated PCF of various time lapse movies to map characteristic correlation times. We used the following correlation function for Pearson coefficient (r(τ)) calculations between two frames U(x,y,t) and V(x,y,t+τ):

$$r(\tau) = \frac{cov(U,V)}{\sigma_U \cdot \sigma_V} \tag{3.2}$$

$$= \frac{\sum_{i=1}^{n} \delta U_i(x,y,t) \cdot \delta V_i(x,y,t+\tau)}{\sqrt{\sum_{i=1}^{n} \delta U_i(x,y,t)^2} \cdot \sqrt{\sum_{i=1}^{n} \delta V_i(x,y,t+\tau)^2}} \tag{3.3}$$

$$\delta U_i = (U_i - \langle U_i \rangle) \tag{3.4}$$

Here, the subscript i denotes the pixel (x, y) of the image and brackets denote averaging of all image pixels. The Pearson coefficient r(τ) ranges between $[0, 1]$. Comparing the first image of a time lapse movie U(x,y,0) with each consecutive frame V(x,y,t) of the movie using the PCF results in a time dependent decay of r(t). This decay over time depends on the dynamics and therefore structural reorganization of actin over time. Fitting an exponential decay function

$$f(t) = A \cdot \exp^{\frac{t}{\tau_c}} + y_0 \tag{3.5}$$

to the Pearson coefficient decay curve r(t) results in a characteristic correlation time τ_c describing how fast the system reorganizes. We calculated this correlation time τ_c for various actin dynamics movies (n=16) of non-confluent cells with $\Delta t = 2$sec or $\Delta t = 10$sec. The time lapse acquisition of microvilli behavior for confluent cells was much more difficult due to the above mentioned reasons of increased background signal resulting in a decreased signal-to-noise ratio. However, we were able to calculate the correlation time for n=6 time lapse movies of confluent cells for comparison ($\Delta t = 10$sec). All movies were de-noised using Matlab filters prior to PCF analysis as described in chapter 2.5.1. Comparing the mean characteristic correlation times of cortical actin dynamics revealed a significant difference in reorganization speed (Fig. 3.17, right).

While for non-confluent cells $\tau_c = (54 \pm 25)$ seconds (mean± standard error) the cortical reorganization of confluent cells is slower with a characteristic correlation time of $\tau_c = (103 \pm 57)$ seconds. Large errors in this analysis method probably result from a strong signal-to-noise dependency of the analysis. Strong intensity fluctuations due to low signal-to-noise ratios result in a faster r(t) decrease over time as the PCF is sensitive to background signaling due to increasing standard deviations (see equation 3.2 and Ref.[2]).

In conclusion, computational PCF analysis confirmed that non-confluent cells show faster structural apical actin reorganization compared to confluent microvilli motion.

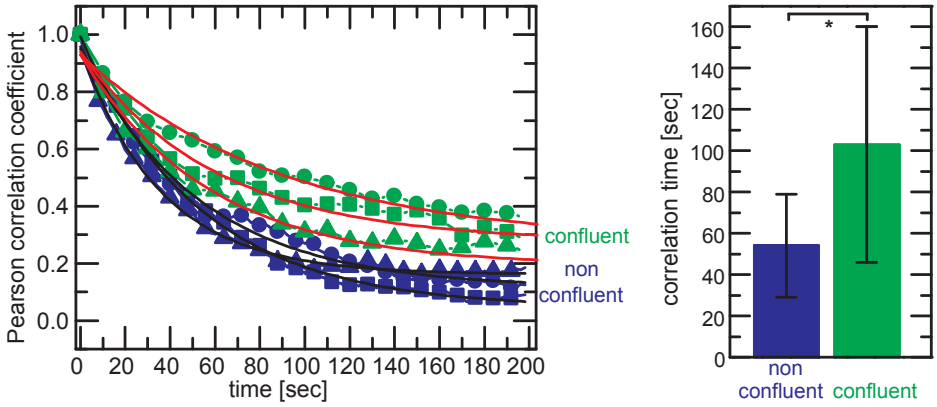

Figure 3.17: Temporal Pearson correlation analysis depicts significant differences in correlation times between non-confluent (blue, n=16) and confluent cells (green, n=6). Three exemplary r(t) curves of non-confluent (blue) and confluent (green) (left). Right: mean±standard error (SE).

STICS analysis defines correlation length

In the course of our cooperation with MIT, Dr. P. Diesinger analyzed the correlation length of actin dynamics using STICS analysis. STICS combines the spatial correlation based on spatial information of a two dimensional image with the time-dependent reorganization dynamics measured by temporal correlations (Ref.[53]). Based on time-lapse movies of non-confluent actin reorganization and using uniform grids, Dr. P. Diesinger calculated spatially and temporally variable velocity fields by performing STICS analysis on neighboring sub-image series in space and time (Ref.[3]). Based on these velocity vector fields, he used the spatial correlation function (SCF) (Ref.[3]) to extract a characteristic correlation length scale, R_0 (Fig. 3.18, left) defining area of correlated motion. The SCF of a vector field with velocity vectors v(x,y,t) of the STICS grid position (x,y) and time t is given by:

$$SCF(R(\epsilon,\eta)) = \left\langle \frac{\sum_j \delta v_j(x,y,t)\cdot\delta v_j(x+\epsilon,y+\eta,t)}{\sum_j \delta v_j(x,y,t)\cdot\delta v_j(x,y,t)} \right\rangle_{\varphi,t} \tag{3.6}$$

$$\delta v_j(x,y,t) = (v_j(x,y,t) - \langle v_j(x,y,t)\rangle_j) \tag{3.7}$$

Here, angle brackets denote averaging over all directions and time, and summation is taken over all positions j. By subtraction of mean velocity vector of field (see equation 3.6) mean STICS velocity field drift is reduced to zero. To extract a characteristic correlation length scale, the SCF(R) was fitted to single exponential decay (see equation 3.4).

In cooperation with Dr. P. Diesinger we applied these STICS analysis on neighboring sub-image series in space and time of actin reorganization time lapse movies. With n=11 we found the characteristic correlation length to be $R_0 = (3.3 \pm 0.9)\mu$m (Fig. 3.18, right) meaning that within 3μm the dynamics were correlated and therefore mechanically coupled.

As the nearest neighbor velocities on the STICS grid had overlapping averaging windows in space and time, resulting in oversampling, we only fitted the exponential SCF(R) decay

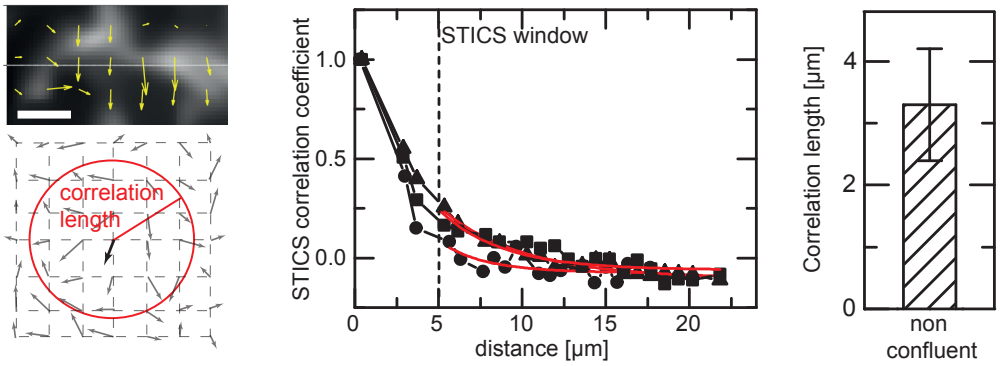

Figure 3.18: Spatial STICS analysis for actin dynamics correlation length reveals mechanical coupling on 3μm length scale. mean± standard deviation (SD) n=11.

outside the STICS window (Fig. 3.18, middle). Unfortunately, we were not able to apply this STICS analysis to confluent cell cortical reorganization for the above discussed reasons of low signal-to-noise ratios.

3.3.3 Actin turnover rate identification using FRAP

As a last step to characterize specific dynamical features of the non-confluent apical actin structures we deduced the turnover rate of the apical actin structures in non-confluent cells. For that purpose we had to establish stable cell lines expressing actin-GFP. As Lifeact-GFP is an indirect marker for filamentous actin with constant turn over (Ref.[138]) it is not suitable for fluorescence recovery after photobleaching (FRAP) experiments, the standard technique for protein turnover rate identification. However, after successfully establishing stable actin-GFP cell lines in MDCK cells we were faced with the observation that the cell clones exhibited strong phenotypic effects (Fig. 3.19). In contrast to Lifeact-GFP or phalloidin staining of actin (Fig. 3.3, 3.19), actin-GFP clones frequently showed rosette-like microvilli structures (Fig. 3.19, middle) or only very few dotted structures at the apical side (Fig. 3.19, right). While the large part of non-confluent actin-GFP cells appeared to have phenotypic morphological changes only some of the cells showed the elongated, membrane parallel and dynamic actin structures described above (Fig. 3.3).

Regardless of the phenotypes, we briefly tested the range of actin turnover at the apical side of non-confluent cells. Using FRAP as the experimental setup we bleached small apical regions including microvilli like actin structures (Fig. 3.20, left white boxes). However, we were not able to identify a characteristic time scale of actin turnover regarding these microvilli structures. To obtain a rough turnover time estimate we simply subtracted a reference signal (Fig. 3.20, red boxes) for photobleaching correction from the mean intensity signal of the FRAP region (Fig. 3.20, right inset, black minus red curve) and normalized. However, the FRAP data appeared inconsistent. While some actin structure intensity recovered rather quickly within about $10-20$ seconds (Fig. 3.20, right blue curve and upper panel left) other

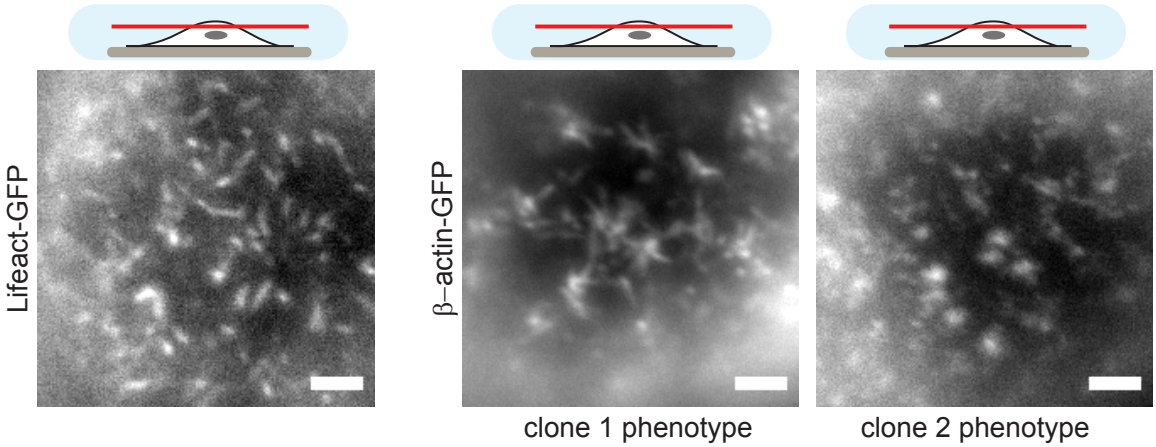

Figure 3.19: Phenotypic artifacts of stably actin-GFP transfected MDCK cells include rosette-like apical actin formation (middle) or sparse, dotted actin distribution even for non-confluent cells (right).

bleached structures showed no or only very slow actin turnover rates of more than 60 seconds (Fig. 3.20, right green curve).

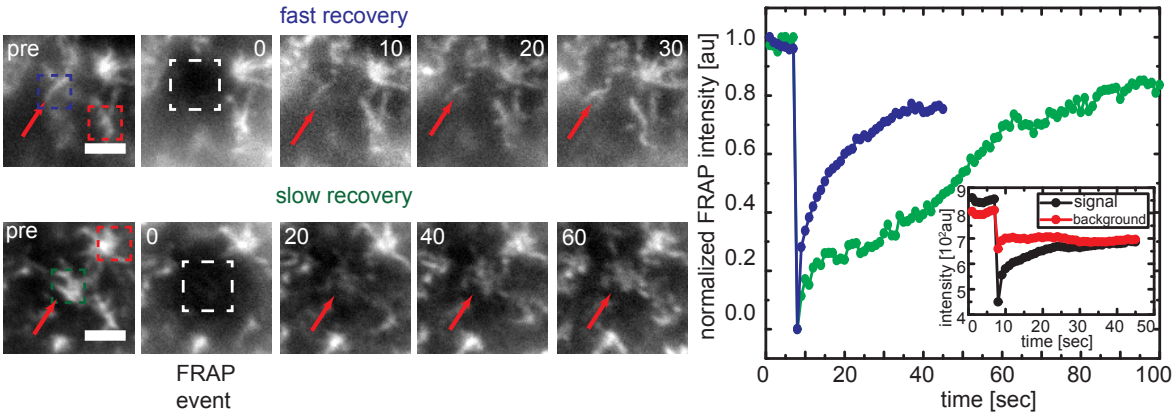

Figure 3.20: Exemplary FRAP measurements for apical actin turnover rates narrows turnover rate between $10-60$ seconds. Scale bar: 1μm, time in seconds.

Considering the fact that these actin-GFP cell line clones exhibited strong phenotypical morphological changes in apical actin structures we did not extend the measurements of actin turnover rate. The inconsistency of FRAP data however made the identification of a characteristic timescale impossible. Nevertheless, actin structures appeared to have turnover rates between 10 to 60 seconds.

3.4 Actin structure dynamics are driven by motor protein

The key question considering actin reorganization was however still elusive. What is driving the actin dynamics? Mainly, two possibilities of actin based motion are usually taken into account: (1) treadmilling of actin filaments (Ref.[120]) or (2) regulation of actin dynamics by its motor protein class of myosin (Ref.[94]).

Treadmilling of actin filaments produces pushing forces as actin monomers are polymerized at one end of the actin filament while being depolymerized at the other filament end with similar rates. In our case, this effect could be ruled out as the major driving mechanism since we frequently observed the reorganization and rearrangement of whole filament structures perpendicular to their elongation axis (Fig. 3.16 first and third panel).

We therefore directly tested for the second driving mechanism of the myosin motor protein class. In detail, we tested myosin dependency by using 50μM of a drug called blebbistatin, that specifically inactivates non-muscle myosin II activity by blocking the adenosine triphosphatase (ATPase) function and thereby slowing down phosphate release (Ref.[160],[84],[95]).

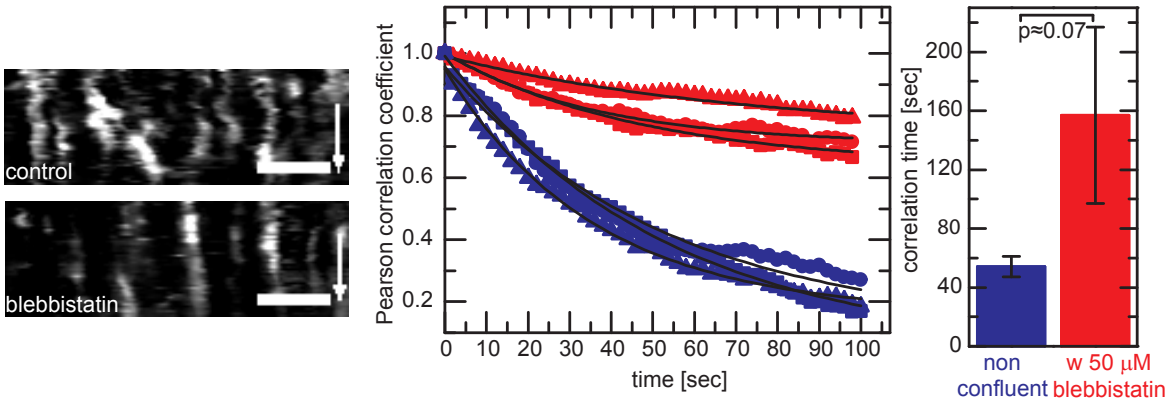

Figure 3.21: Apical actin dynamics is myosin motor dependent as demonstrated by inhibition of motion by 50μM blebbistatin using kymograph (left) and Pearson correlation analysis (right). Scale bar: 2μm, time arrow 300sec, n=12 movies for blebbistatin treatment (right), mean±SE.

As predicted, we monitored a decreased actin reorganization speed. Kymograph analysis of time lapse movies acquired from blebbistatin treated versus control cells depict the effect of decreased actin structure motility (Fig. 3.21, left). Moreover, we analyzed n=12 time lapse movies from 15 minutes drug pre-incubated cells using again Pearson correlation analysis (chapter 3.3.2). The characteristic correlation time was significantly enhanced to $\tau_c = (156 \pm 60)$ seconds (mean± standard error) compared to a control set of cells already analyzed in Fig. 3.16. The large error in correlation time for blebbistatin treated cells presumably resulted from the known effect of partial blebbistatin photo-inactivation (Ref.[142]). Nevertheless, the reorganization speed of actin was strongly reduced by the inhibition of myosin activity, which prompted us to focus subsequently on the non-muscle myosin motor.

3.5 Discussion

In this chapter we have shown that the apical surface of non-confluent epithelial cells is covered by elongated and flexible MV that undergo complex, myosin II driven lateral displacement. The frequently membrane parallel MV exhibit coordinated motion on a 60sec time scale and 3μm length scale. Different to MV of confluent epithelial cells we often found bent apical actin structures, that sometimes even fused together forming long and complex arrangements. These MV like elongated protrusions disappear when the cell reaches a higher state of confluency by building cell-cell contacts with neighboring cells. Vice versa, these apical structures emerge whenever confluent cells loose their cell-cell contacts, for example during wound healing or a growth factor induced epithelial-mesenchymal transition.

Why has this profound change in apical structure and dynamics not been described previously? The main reason for this gap in MV related research is presumably the fact that epithelial cells are hardly ever in a non-confluent situation compared to the typical situation of highly specialized brush-border epithelium. That is why the focus has so far been put on polarized and confluent EC with the prototypical MV array organization(Ref.[56],[90],[135]). Moreover, until now most studies on MV have tackled important questions regarding the MV protein composition and constitution while dynamic analysis of these structures have only played a minor role (Ref.[10], [11]). However, scanning electron micrographs and fluorescence images have already shown bent and elongated microvillar structures in epithelial cell culture (Ref.[13],[20]). More recently ezrin, as an actin-membrane-linker protein and its adapter EBP50 have been shown to localize to bent apical protrusions (Ref.[37],[89]). In developmental biology apical protrusions with the characteristics of bent MV have been reported during the epithelia reorganization of developing *Drosophila melanogaster* embryos (Ref.[132]). All these results from various model systems and biological backgrounds indicate, that these elongated apical protrusions serve a distinct purpose. Unfortunately, in the course of this study we were not able to deduce a specific function for the elongated MV neither by molecular biology nor by biophysical approaches. This lack of clarifying experimental results constrains the discussion to speculations and hypothesis about functional aspects of these structures.

In general, MV function has for long time only been acknowledged as a structural component to increase the cell-surface area for optimized nutrition uptake. However, in recent years these apical structures have been implicated in various additional cellular tasks including regulation of energy metabolism, gating of ion flux, generation and modulation of membrane potential, Ca^{2+} signaling and storing as well as mechanoreception (Ref.[90]). As we only observe the elongated membrane-parallel MV on non-confluent cells undergoing migration we hypothesize that these structures are acting as mechanosensors, alike filopodia structures within the basal cell region. The rapid turnover rate and fast lateral reorganization of the actin bundles indicate that, as for filopodia in the basal region, the environment is constantly scanned for potential cell neighbors. Moreover, the group member Dr. R. Aufschnaiter could show by laminar shear flow experiments (not shown) that the elongated MV disassemble on short time scales uponnon-confluent calcium influx. Hence, a Ca^{2+} mediated signaling and storage would also be a putative feature of the identified actin structures. It will be of high interest to ascertain these potential roles as cellular antennas in future experiments.

Chapter 4

Apical Myosin II Organization and Dynamics

4.1 Introduction

Vast amounts of cellular regulatory processes are dependent on physical forces, either pushing or pulling. As for the cytoskeletal proteins there are three key players responsible for the application of force: (1) kinesins, motor proteins related to microtubules, (2) dyneins, which move along microtubules as well, and (3) myosins, the motor proteins working in concert with actin. While kinesins and dyneins are known to serve as motor proteins in transport mechanisms along tracks of microtubules (Ref.[57],[75]), intermediate filament specific motor proteins are not known so far. Polarity of filaments is a prerequisite for directed motion of molecular motors and intermediate filaments are not known to be polar (Ref.[177]). Myosins as the third motor protein superfamily play a crucial role in almost all cellular processes that require physical forces or translocation. These very adaptable proteins can walk along, propel the sliding of or produce tension on actin filaments (Ref.[171]).

While some myosins act as transporters by binding cargo to their C-terminal end, the majority of myosins form small filaments by linking their C-terminal ends so that the head parts at the filament poles can tether two actin filaments (Fig. 4.1)(Ref.[115],[58]). Most of the myosins are members of class II which is a pool for so called conventional myosins. Within this class myosins are separated depending on their location either in muscle cells, named then muscle myosins, or they belong to the group of non muscle myosins (Ref.[29]).

As we investigate the cytoskeletal structure and dynamics of epithelial cells we focused on non-muscle myosin II (NMMII). These NMMII complexes are hexamers composed of myosin heavy chain dimers (MHC) and two pairs of myosin light chains (MLC), namely one pair of regulatory light chains and one pair of essential light chains (Fig. 4.1) (Ref.[171]). The diversity of myosin isoforms results from different MHCs in different cell types. In all vertebrates over 15 different myosin isoforms are known (Ref.[22]). However, in mammalian cells only three isoforms encode three different non-muscle MHCs, commonly referred to as MHC-A, MHC-B and MHC-C (Ref.[22] and Ref. therein). In MDCK cells, the mostly used model cell line of this study, only MHCA and MHCB are present (Ref.[174]). Both isoforms have different properties and functions and can therefore not easily been replaced by another. While MHCA has a higher adenosine triphosphatase (ATPase) activity, the duty ratio of MHCB is higher and its ADP removal kinetics take longer (Ref.[83],[85]). Myosin IIA should therefore be better suited for rapid remodeling and adaptive contractile activity, whereas myosin IIB can act as a stabilizing factor, resistant to high tension, due to its stronger link to actin (Ref.[94]).

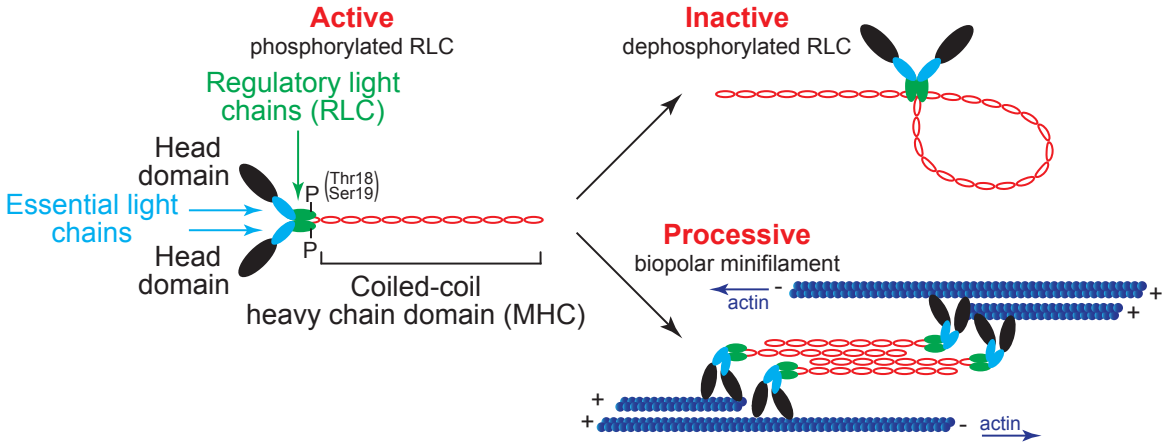

Figure 4.1: Schematic view of non muscle myosin II structure and function in concert with actin filaments.

In the course of this study we mainly focus on the characteristics of MHCA to understand its role in cell cortex maintenance. First results on MHCB, gained by the group member N. Zwing during her bachelor thesis (Ref.[185]), indicate similar localization and behavior of the myosin isoforms though detailed dynamic outcomes are not yet present. Morphogenesis and cellular shape transformation are crucial steps not only in developmental processes of whole tissue (Ref.[103]) but also e.g. during wound healing processes and cell migration of single cells(Ref.[171]). For all these processes mechanical force, or more precise, mechanical tension is essential to control cell shape. NMMII are fundamental units for the creation of contractile forces, as they can assemble to highly processive bipolar machineries, namely minifilaments (Fig. 4.1), that generate contractility in concert with cortical actin networks (Ref.[92]).

Here, we describe a previously unidentified isotropic NMMII network spanning the whole innercellular apical cell cortex of non-confluent ECs. The myosin network exhibits highly dynamic reorganization and coordinated motion. When ECs grow to higher confluency with an increasing number of cell neighbors the network disappears thus resulting in a changing apical myosin distribution to the previously described dotted structure. Myosins then interconnect MV at their base to the terminal web (Ref.[57],[174]). We can show that this isotropic myosin network keeps the apical cortex under tension and that it ruptures upon treatment with a actin filament severing drug (LatB), which confirms the dependency of the myosin network on actin filament structure. Importantly, this network is not unique to the MDCK model cell line but is present in various different cell types including carcinoma, osteosarcoma, fibroblast-like and fibroblast model cell lines.

4.2 Myosin structure differences depend on confluency

One crucial outcome of our apical actin organization investigation (chapter 3.4) was the dependency of actin reorganization on the activity of non muscle myosin II motor proteins (Fig. 3.20). We therefore continued our investigation by focussing on the localization, arrangement and dynamic behavior of myosin II. After the establishment of stable MDCK cell

lines labeling either MHCA-GFP or MLC-GFP (chapter 4.1) we once again used live cell fluorescence microscopy for detailed analysis.

Apical actin organization was significantly different when comparing non-confluent to confluent cells (Fig. 3.1). We therefore continued our investigation by focussing on localization, arrangement and dynamics. We hypothesized, that myosin localization should as well vary depending on the confluency state of the cell. We were however surprised that we not only observed modest myosin organization differences, as for actin microvilli organization, but a complete change of structure. For confluent cells the typical and already described dotted structure (Fig. 4.2, left), related to myosin localization within the terminal web at the microvilli bases, was observable (Ref.[56],[174]). In contrast, for non-confluent MDCK cells we found a previously not described extensive isotropic myosin network spanning the complete apical cell cortex (Fig. 4.2, right).

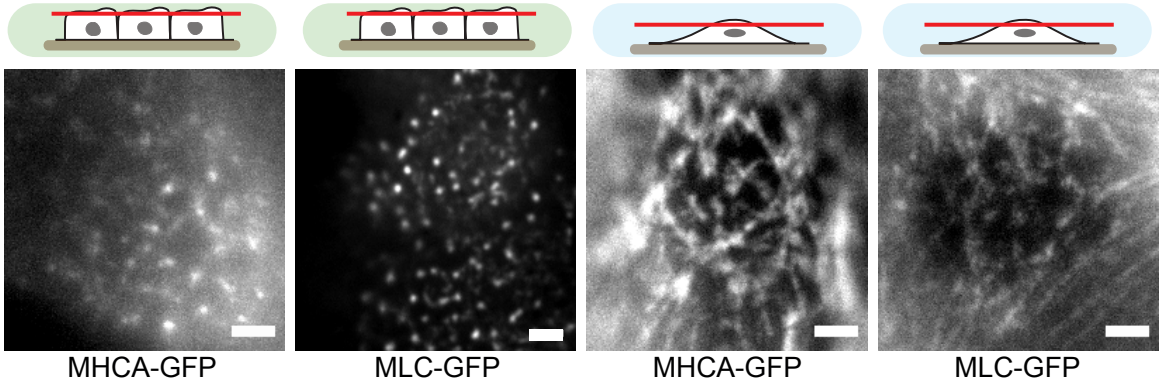

Figure 4.2: Confluent (left) versus non-confluent (right) apical myosin distribution. Extensive isotropic network of MHCA or MLC spans complete apical cell cortex for non-confluent cells (right). Scale bar: 2μm.

4.3 Biochemical myosin localization test and cell model screening

For live cell imaging using fluorescently labeled proteins it is a prerequisite to check if the additionally transfected protein constructs lead to possible artifacts including protein overexpression or false protein localization within the cell. To check for these artifacts, Dr. R. Aufschnaiter performed various experiments including western blots (Fig. 4.3, left) to check for expression levels as well as antibody staining for endogenous localization of proteins (Fig. 4.3, right). The unpublished data presented here was acquired and kindly provided by Dr. R. Aufschnaiter.

The Western blot analysis (Fig. 4.3, left) clarified that MHCA-GFP, additionally incorporated into the genome, was not expressed in such high amounts that overexpression artifacts occur as the band intensities of MHCA plus MHCA-GFP (left lane) were comparable to the control band of MHCA only.

Using antibody staining for endogenous MHCA on either untransfected (Fig. 4.3, middle) or stably MHCA-GFP transfected cells (Fig. 4.3, right) we moreover observed equivalent

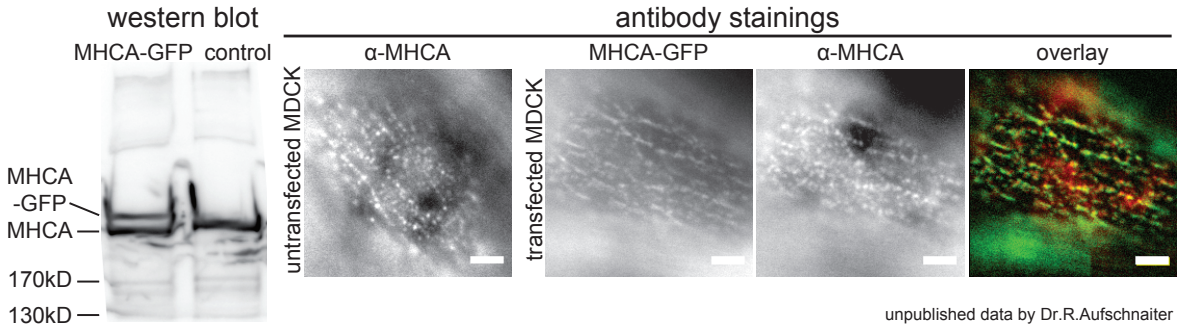

Figure 4.3: Western blot (left) and antibody staining of non transfected (middle) or MHCA-GFP transfected cells (right) confirm correct MHCA localization and wild type-like expression level (left). Scale bar: 2μm.

isotropic networks. Colocalization experiments of MHCA-GFP and the MHCA antibody staining additionally resulted in high degree of signal overlap. Hence, the insertion of MHCA-GFP did not result in artifacts on the expression and localization level.

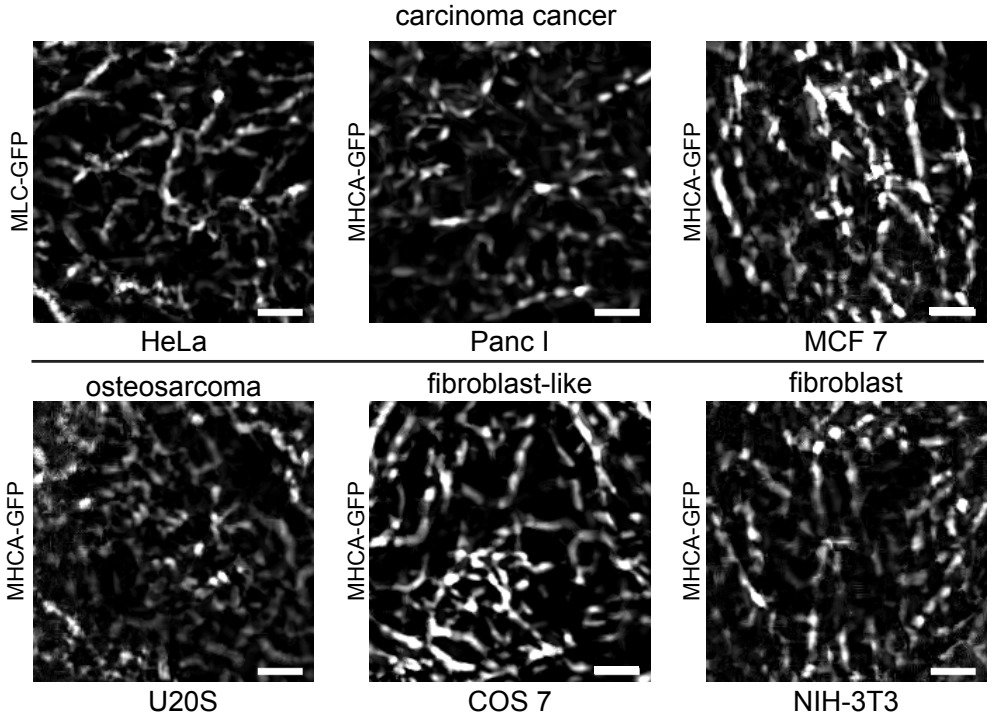

Figure 4.4: Cell model screen confirms widespread isotropic myosin network existence as it can be found in carcinoma, osteosarcoma and fibroblast(-like) cell models.

Secondary, we screened various epithelial-like and epithelial cell lines to identify if this newly found isotropic myosin network is specific for MDCK cells or if it is present in other cell lines as well. We tested carcinoma cancer cells with epithelial morphology (HeLa, PancI

and MCF7), one osteosarcoma cell line (U2OS) as well as one fibroblast-like (COS7) and one fibroblast cell line (NIH-3T3) by transiently transfecting these cell lines with MLC-GFP (HeLa) or MHCA-GFP (other cell lines) (Fig. 4.4).

Strikingly, all of these model cell lines derived from very diverse cellular backgrounds were apically enclosed by the myosin network structure. This key finding led us to the conclusion that the apical myosin network structure seems to be a general cellular mechanism to keep the apical cell cortex of non-confluent cells under tight mechanical control. Having identified the important fact that the apical network is a general cellular cytoskeletal structure we continued our investigation mostly on MDCK cells as we had already established stable MHCA-GFP and MLC-GFP cell lines.

4.4 Wound healing assay reveals physiological importance

As one aspect we had to address the question if this network is an artifact of seeding only low numbers of epithelial cells to maintain non-confluent situation or if this network is as well reconstituted during wound healing. We therefore performed again a wound healing assay now using stably transfected MHCA-GFP cells. After confluency was reached and the spacer was taken out we monitored cells at the border of the wound as well as cells within the following cell sheet (Fig. 4.5).

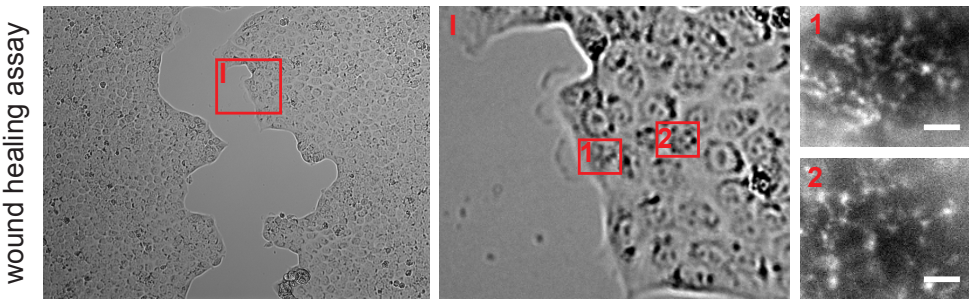

Figure 4.5: Physiological wound healing assay reveals apical myosin change to more network-like structures for cells at wound (1) compared to confluent cells (2). Scale bar: 2μm.

Even though the differences were not as obvious as for the experimental procedure of low versus high numbers of cell seeding we still found distinct changes in the apical myosin localization. While cells close to the wound though within the cell sheet show the dotted myosin structure as for confluent situation (Fig. 4.5, right (2)), border cells regained at least partially the isotropic network (Fig. 4.5, right (1)). Why the cells were not able to fully reassemble the isotropic network is still to be elucidated. We hypothesize, that switching from confluent to non-confluent state without fully intact cell-cell contacts takes more than 24 hours as proteins related to one of these states have to be either expressed or disassembled. For the wound healing assay however, we had to image cells already after 12 hours as the wound closure happened within 24 hours. Further investigations regarding the network dependency on protein expression levels should clarify this issue.

4.5 Network structure variations and substrate geometry dependence

In the course of investigation we noticed that different non-confluent cells exhibited myosin network structures with varying arrangements. We hence classified the networks into three most commonly observed classes. The small fraction of cells not showing any of these network arrangements were not considered. The apical myosin network of non-confluent cells was arranged either in a three basal fixing point fashion (Fig. 4.6, left), in a polarized manner with only two basal anchorages (Fig. 4.6, middle) or cells exhibited an equatorial myosin ring within the cell cortex (Fig. 4.6, right arrows) that was attached to the basal region at various places. For the third class, no extensive and highly ordered isotropic network was distinguishable above the equatorial ring.

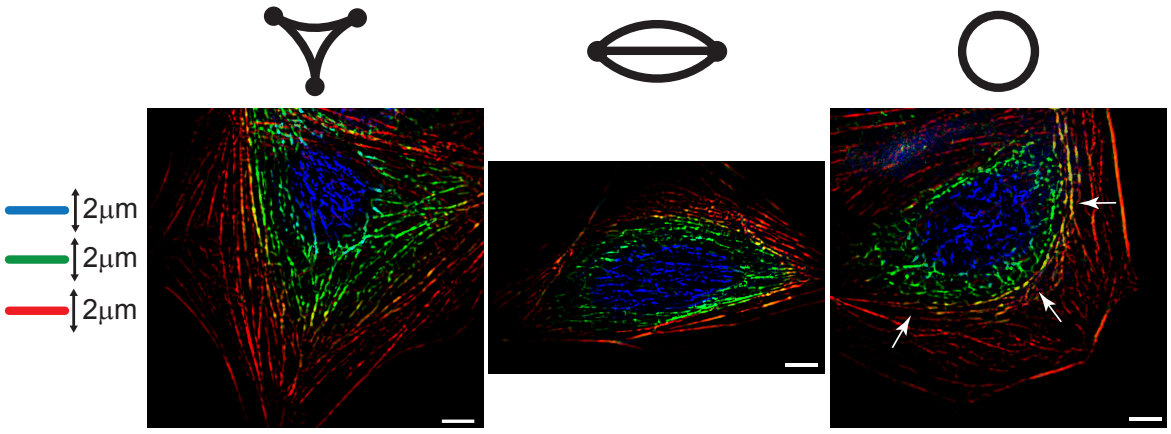

Figure 4.6: Myosin network classification with either three fixations at basal plane (left), two fixation points (middle), or existence of equatorial ring (right) fixed at various basal positions. Color overlay spanning 6μm in depth. Scale bar: 5μm.

To acquire these images we adopted our measurement in the way that we scanned through the cell at six focal planes, each 1μm apart from the other, and subsequently maximum projecting two by two focal planes of the filtered images and finally color coding the overlay of the maximum projected planes (Fig. 4.6, scheme). By using this method we were able to visualize the complete apical membrane surface up to 6μm in depth.

Since the arrangement of the apical network seemed to be dependent on the basal fixing points at the cell bottom we subsequently probed the dependency of the network structure on the basal plane appearance or restriction. For that purpose we used Cytoo micropattern chips containing patterns of various geometries (Y, crossbow, H and disc) with a size of $700 - 1600\mu m^2$. The micropatterns were fibronectin coated while the surrounding area was passivated to inhibit cell attachment. After checking all pattern sizes we were surprised that whenever cells were restricted to a certain basal region they almost or completely lost the apical myosin network structure.

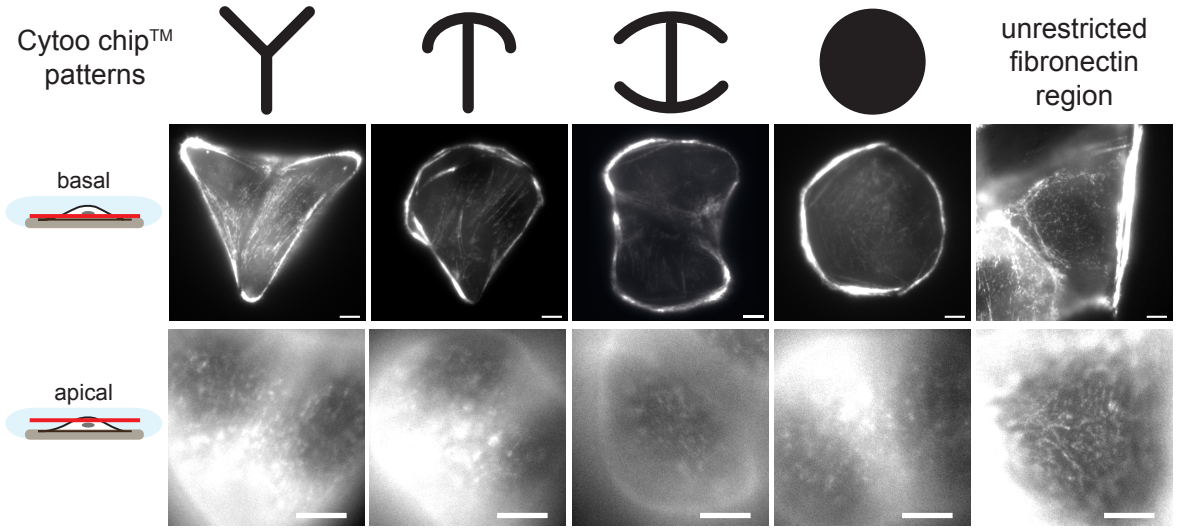

Figure 4.7: Cells seeded on fibronectin coated micropatterns with various geometries lead to myosin network disassembly. Disassembly irrespective of fibronectin coating as cells on chip boarder exhibit network structure (right). Scale bar: 5μm.

As exemplary shown for medium sized patterns all cells attached correctly to the substrate and strong stress fiber formation was observable (Fig. 4.7, upper panel). However, the cortical network was little or not present due to the basal plane restriction and the inability of the cell to migrate (Fig. 4.7, lower panel). This was a good finding as we directly observed a mechanosensing property of the apical myosin network. On the other hand it was surprising that even for the Y-shape pattern, that nicely mimics the class of three fixing points (Fig. 4.5), no extensive network was observable.

The possibility of a cellular response to fibronectin coating could be excluded, since cells attaching to adhesive fibronectin coated separation bands between the geometry blocks of the Cytoo chips exhibited the usually observed network structure (Fig. 4.7, right). In these band regions cells were still able to migrate in at least one direction. In conclusion, the formation of an apical myosin network must be directly associated with the cellular basal plane appearance and the cells ability to migrate.

4.6 Temporal and spatial correlation analysis of myosin network

Apart from the structural details regarding the myosin network we performed time lapse image acquisition to characterize dynamical network properties. To retrieve dynamical information of large cortical parts we again scanned through the cell at three focal planes 1μm apart and maximum projected the filtered time series on top of each other (Fig. 4.8, color coded left). Analyzing the dynamical behavior of cortical MHCA and MLC in non-confluent cells using kymographs, we observed fast rearrangements (Fig. 4.8, kymographs) in accordance to actin reorganization (Fig. 3.15). In comparison, myosin dotted structures of confluent cells

rearranged only slowly (data not shown). It was, however, very difficult to acquire reliable data of confluent myosin dynamics as presumably only small fractions of motor proteins were recruited to the cell cortex leading to fast photobleaching effects.

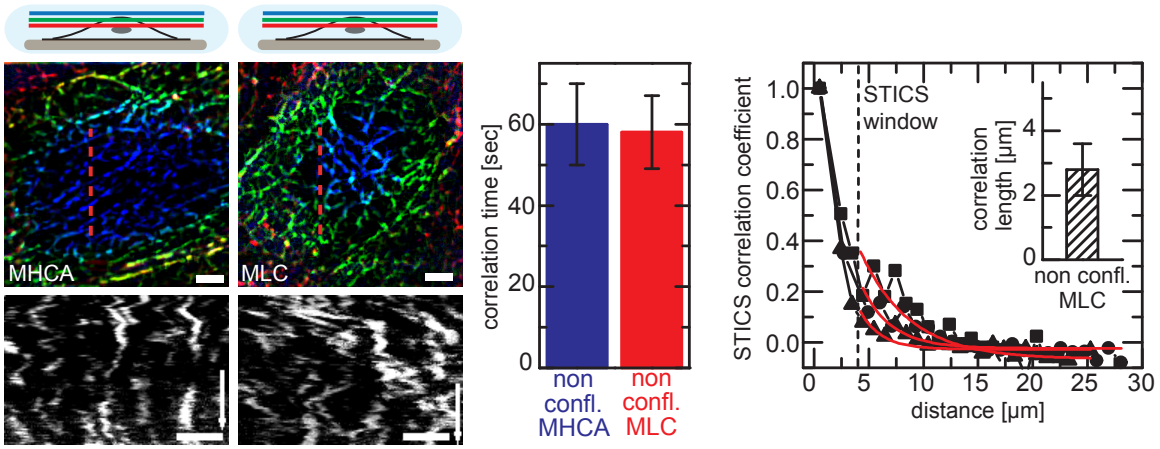

Figure 4.8: Isotropic myosin network reorganized highly dynamic in non-confluent cells as demonstrated by kymograph (left) and PCF analysis (middle). Temporal correlation time similar to actin with (60 ± 10) sec for MHCA and MLC and spatial correlation length similar with $(3 \pm 1)\mu$m (right, obtained by Dr. P.Diesinger). Scale bar: 2μm time arrow 400 sec.

Subsequently, we performed quantitative image correlation analysis to map myosin dynamics. Not only PCF analysis of non-confluent MHCA and MLC dynamics resulted in actin comparable (see Fig. 3.17) characteristic time scales of about (60 ± 10) seconds (Fig. 4.8, middle), but also STICS analysis, performed by Dr. P. Diesinger, led to similar results of a $(3 \pm 1)\mu$m characteristic correlation length scale (Fig. 4.8, right and inset) as for actin dynamics (see Fig. 3.18). These findings already indicated the interdependence of actin and myosin structures that will be discussed in detail in the following chapter 5.

4.7 Dynamics functionality test of MHCA and MLC tagging

Before continuing our dynamics analysis we had to ascertain the proper dynamic functionality and cellular positioning of the expressed fluorescently labeled protein constructs MHCA-GFP and MLC-mCherry regarding their dynamic behavior. For that reason we established stable cell lines containing both constructs, MHCA-GFP and MLC-mCherry, using two antibiotic selection markers hygromycin and puromycin (chapter 2.3.1). As these two myosin motor subunits must be in close proximity for proper myosin function we assumed a complete colocalization and identical dynamic behavior. As expected, both proteins almost perfectly colocalize in stably double transfected cells. Moreover, MHCA-GFP and MLC-mCherry show identical dynamical patterns in kymograph analysis (Fig. 4.9).

This finding, in combination with the correlation analysis results of MHCA-GFP and MLC-GFP (Fig. 4.8) and antibody stainings (Fig. 4.3), led to the conclusion that all used myosin

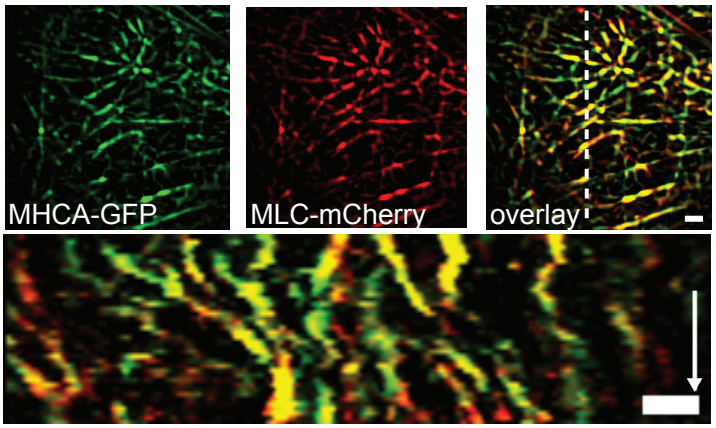

Figure 4.9: MHCA-GFP and MLC-mCherry stable transcected cells. Functionality test depicts almost perfect colocalization as well as identical dynamical patterns thereby confirming correct construct function. Scale bar: 2μm time arrow 300 sec.

constructs localize properly and are functional regarding their dynamics at the cortex of non-confluent cells. We therefore continued our in depth analysis mostly using stable MHCA-GFP transfected cells.

4.8 Myosin turnover rate identification using FRAP

The confirmation that MHCA-GFP transfected cells showed no dynamics or localization phenotype prompted us to execute FRAP experiments again. While we only stated rough estimates for actin turnover rates due to actin-GFP artifacts we were now able to obtain more reliable data on MHCA recovery rates. We hence applied a more sophisticated FRAP analysis method based on double normalization of FRAP data (Ref.[124]).

Briefly, we took into account photobleaching effects during experiment as the turnover rates of MHCA was in the range of several seconds. We therefore measured mean intensities over time at three different regions of interest (ROI) in the cell: (1) 13x13μm whole cell ROI marked in green, (2) FRAP region ROI marked in blue, and (3) 1.65x1.65μm base intensity ROI marked in red outside the cell (Fig. 4.10, left). To deduce the ratio between whole region versus FRAP region intensity before FRAP event at t_{FRAP} we calculated the mean pre-FRAP intensities:

$$I_{\text{wholeROI-preFRAP}} = \frac{\sum_{t=0}^{t_{\mathrm{FRAP}}-1} I_{\text{wholeROI}}(t)}{\mathrm{n}_{\text{preFRAP images}}} \tag{4.1}$$

$$I_{\text{frapROI-preFRAP}} = \frac{\sum_{t=0}^{t_{\mathrm{FRAP}}-1} I_{\text{frapROI}}(t)}{\mathrm{n}_{\text{preFRAP images}}} \tag{4.2}$$

Furthermore, we subtracted the background ROI $I_{\text{backgROI}}(t)$ (Fig. 4.10, red curve) intensity from the mean ROI intensities $I_{\text{wholeROI}}(t)$ (Fig. 4.10, green curve) and $I_{\text{frapROI}}(t)$ (Fig. 4.10, blue curve), respectively. The normalized FRAP curve was subsequently calculated by:

$$I_{\text{FRAP-norm}} = \frac{I_{\text{wholeROI-preFRAP}}}{I_{\text{frapROI-preFRAP}}} \cdot \frac{(I_{\text{frapROI}}(t) - I_{\text{backgROI}}(t))}{(I_{\text{wholeROI}}(t) - I_{\text{backgROI}}(t))} \tag{4.3}$$

As a final step we normalized $I_{\text{FRAP-norm}}$ to zero minimum and 1 as maximum, respectively (Fig. 4.10, inset black curve).

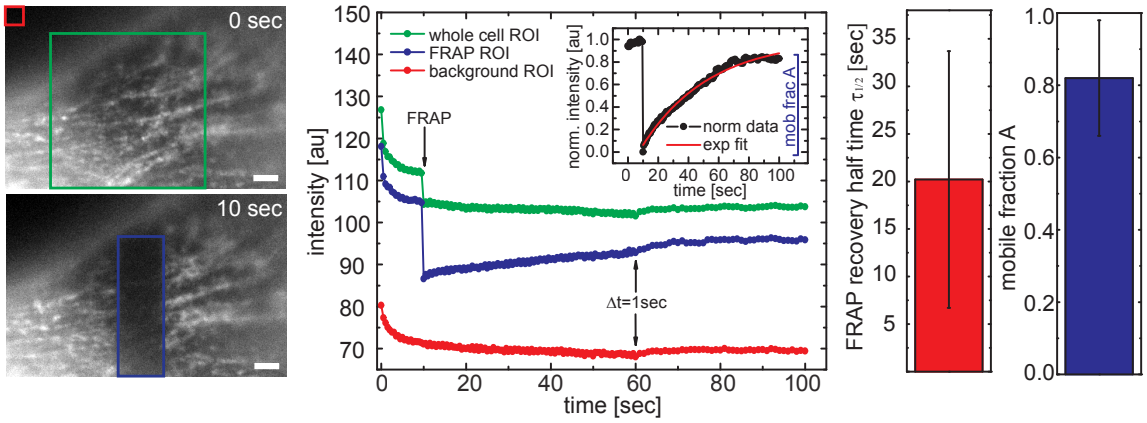

Figure 4.10: FRAP experiments of apical myosin network to deduce myosin turnover rate lead to recovery half time of $\tau_{1/2} = (20.2 \pm 13.5)$ sec and mobile fraction of $A = (0.8 \pm 0.2)$. Scale bar: 2μm, n=12, mean±SD.

Before presenting FRAP results several remarks concerning the intensity traces need to be stated that had effects on the outcome. First, within the pre-FRAP images the signals already dropped significantly presumably due to cytosolic background signal bleaching. Taking the mean pre-FRAP intensities (equations 4.1-4.2) rather than intensities at $t = 0$ sec was therefore indispensable. Moreover, it was necessary to change the Δt between consecutive frames from $\Delta t = 0.5$ seconds to $\Delta t = 1$ seconds after 60 seconds to reduce photobleaching effects. This led, however, to small irregularities in the intensity traces as the remaining background signal recovered to small degree. These effects could not be circumvented or would need further measurement optimization.

Nevertheless, we were able to fit the following single exponential fit to the obtained FRAP curves (Fig. 4.10, inset red curve):

$$f(t) = A + C \cdot e^{t/\tau} \tag{4.4}$$

Subsequently, we calculated the FRAP recovery half time $\tau_{1/2}$ to:

$$\tau_{1/2} = -ln(0.5) \cdot \tau \tag{4.5}$$

Moreover, we extracted the mobile fraction part A (Fig. 4.10 inset, blue schematic) as a rough estimate from the exponential fits. Analyzing $n = 12$ cells by FRAP resulted in a

$\tau_{1/2} = (20.2 \pm 13.5)$sec FRAP recovery half time and an estimate for the mobile fraction A = (0.8±0.2) (Fig. 4.10, right). Note here again, that these results are only first approximations to define a characteristic time scale. Optimized measurements and more elaborated analysis will be needed to clearly define recovery times $\tau_{1/2}$ and make assumptions about the underlying transport processes such as e.g. diffusion, which can be determined by carefully exploiting FRAP data (Ref.[4],[158]).

4.9 Drug induced interference in myosin network dynamics

We next addressed the question if the myosin network dynamics is a direct consequence of myosin activity or if the unlikely case of passively driven network motion occurs. To interfere with myosin activity we used two drugs. First blebbistatin (50μM), which blocks the adenosine triphosphatase (ATPase) activity and thereby the gliding motility of non muscle myosin II without interfering with the myosin light chain kinase (Ref.[160]). Second, we used ML7 ((50μM)), a drug which blocks the myosin light chain kinase (MLCK) and thereby inhibiting the phosphorylation and activation of myosin light chain (Ref.[102]). For both drugs myosin network motion was blocked as demonstrated by kymograph analysis (Fig. 4.11) showing that myosin itself actively reorganized at the apical cell cortex.

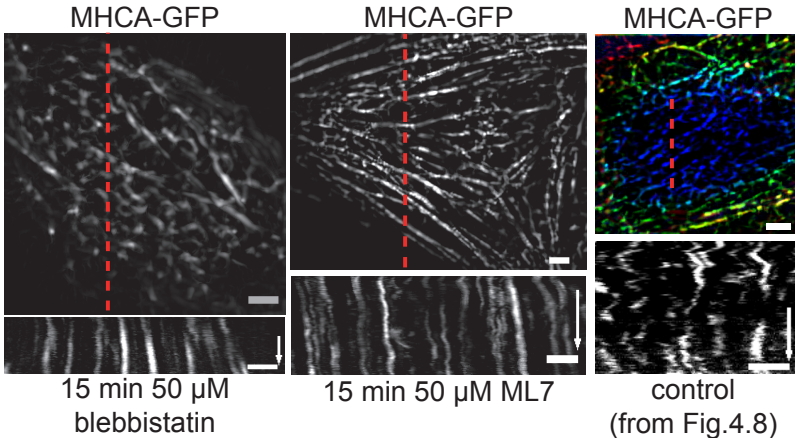

Figure 4.11: Myosin dynamics blocked by blebbistatin and ML7 drug treatment demonstrate necessity of myosin activity for reorganization. Scale bar: 2μm time arrows: 300sec.

Subsequently, we reversed the above described drug experiment (chapter 3.4). We now traced myosin network behavior while disrupting filamentous actin by using the actin monomer binding drug Latrunculin B (LatB)(Ref.[157]). Binding of LatB to actin monomers inhibits actin polymerization, which results in actin filament destabilization and eventually in actin filament rupture. Using intermediate amounts of LatB (500nM) we revealed intriguing effects.

After about six minutes of LatB treatment the cortical myosin network structure started to rupture at various positions, thereby implying that the myosin network structure is actin

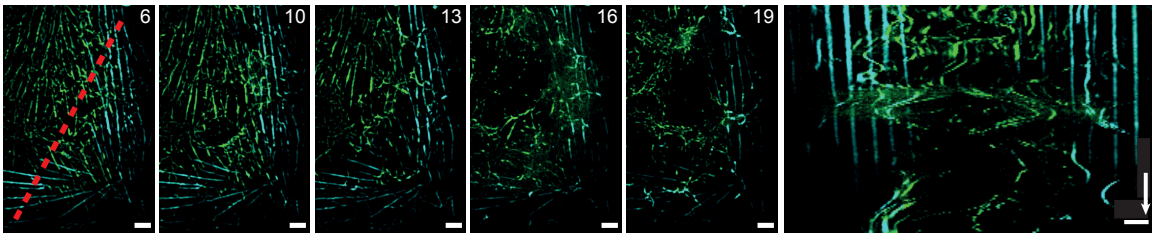

Figure 4.12: Intermediate amount of 500nM Latrunculin B drug results in myosin network destabilization followed by long lasting (10min) long range oscillatory reorganization of the apical network (green) while stress fibers at basal surface are not effected (cyan). Oscillations are visible in kymograph (right). Scale bar: 2μm, time arrow: 300sec

filament based. In addition, the myosin network ruptures resulted in long range oscillatory network rearrangements for over ten minutes rather than leading to instantaneous network disassembly (Fig. 4.12, kymograph). Surprisingly, the stress fibers at the basal side (Fig. 4.12, cyan color code) showed no sign of rupture after LatB treatment, while the complete apical cell region (Fig. 4.12, green color code) underwent large scale fluctuations. This observation gave rise to two hypotheses. First, the assumed network-incorporated actin filaments were rather thin compared to the thick basal actin stress fibers. Second and more importantly, the oscillatory fluctuations upon rupture pointed towards a prestressed myosin network under tension.

4.10 Laser ablation confirms intrinsic myosin network tension

To confirm the hypothesis of network tension we performed fluorescence microscopy using a microscope setup equipped with a UV laser cutting device. This setup allowed μm small precise and predefined cuts within the cell cortex without destroying the plasma membrane. Obtained results clearly demonstrated the existence of tension within the cortical myosin network as hypothesized (Fig. 4.13). Directly after cutting within the cell cortex (along blue line in Fig. 4.13) filaments in close proximity to the cut were pulled apart within subseconds. Performing kymograph analysis along red line (Fig. 4.13, left and kymograph right) we visualized this network rupture and loss of tension. After the instantaneous tension release, the network stabilized and within about 30 seconds new filaments assembled and network tension increased again to steady-state level as can be seen in the kymograph (Fig. 4.13, right).

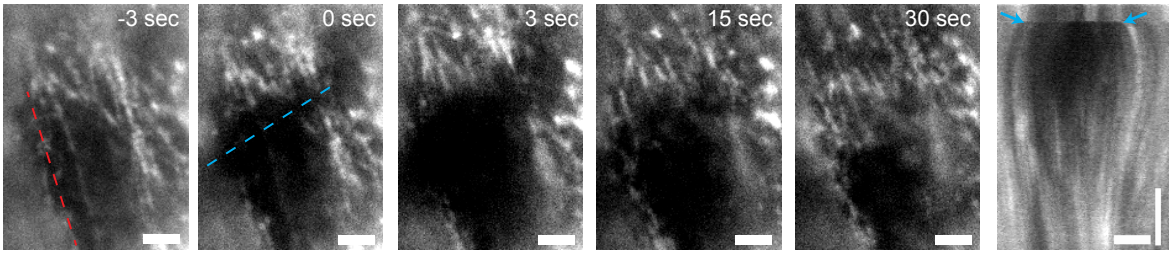

Figure 4.13: Laser ablation experiments depict intrinsic myosin network tension as small cut leads to instantaneous tension release (fast recoil kymograph) followed by steady state regain within about 30 sec (right and kymograph). Scale bar: 2μm, time arrow: 10sec, time in sec.

4.11 Discussion

In this section we described a novel myosin network structure spanning the complete apical cell cortex of non-confluent epithelial cells. This newly identified network is not only present in non-confluent MDCK cells but is presumably widely distributed among non-confluent cell lines with epithelial morphology. In detail, we revealed the existence of an apical isotropic myosin network in carcinoma cell lines (HeLa, PancI, MCF7) as well as in osteosarcoma cells (U20S) and in fibroblast-like (COS) or in fibroblast cell lines (NIH-3T3) (Fig. 4.4). Moreover, we could show that in MDCK cells the network structure reappears in wound healing assays for leader cells at the border of the wound (Fig. 4.5). We therefore conclude that this apical cytoskeletal element is universal to a majority of epithelia related cells that are in migratory state either due to immortalization to carcinoma cells, by their natural function as fibroblast cells or for normal epithelial cells during wound closure.

One important finding is the mechanosensibility of the newly identified apical myosin network to substrate restriction. Whenever cells are plated on collagen coated microfabricated patterns of defined geometry the network is disassembled or strongly reduced (Fig. 4.7). This coupling of the apical cell cortex organization to the basal cellular surface restriction is even more interesting regarding the fact that the two cellular subregions appear to be decoupled in force distribution. As shown in Fig. 4.12 we were able to induce small force imbalances in the apical network structure by application of low LatB drug dose that led to long range reorganization processes on minute time scales while the basal membrane with its related stress fibers showed no signs of changing force distributions and remained static. We therefore presume that the process leading to the disappearance of the apical network structure upon cell plating on patterns is not a direct consequence of changed force distribution in the basal plane. In contrast, this process assumingly results from cycles of mechanosensing, mechanotransduction into biochemical signals (Ref.[28]), and mechanoresponse (Ref.[172]). It will be of highest interest in future investigations to deduce the signaling pathway that induces the assembly and disassembly of the isotropic apical myosin network structure as this will hint towards the regulatory cellular function of the network.

The second important finding is the observation that the apical network is tensile. As shown in Fig. 4.13 small cuts in the network structure lead to fast tension release and opening of

a gap. In literature, cellular mechanotransduction in the context of surface tension has been intensively discussed in recent years. In brief, cells and cellular tissue need two contradicting properties at the same time: (1) a robust cytoskeletal architecture, needed for stability and mechanical resistance against mechanical stress, and (2) non-confluentcells must morphologically adopt, hence they need plasticity that allows remodeling (Ref.[91]). The cell cortical balance between robustness and plasticity is often named tensional homeostasis, for which several models have been proposed. These models discuss e.g. if cells can be described as a viscoelastic material (deformation properties time dependent) (Ref.[39],[100]), how forces propagate within cells and tissue (e.g. stress-wave propagation, tensegrity model) (Ref.[92],[173],[140]), and how cofactors such as cross-linker or motor proteins change the physical behavior of biopolymer networks (Ref.[80],[38],[166]). Large fractions of these intriguing studies have used reconstituted *in vitro* approaches to shed light on the physical properties of tensile cytoskeletal networks. In contrast, our newly identified cortical myosin network is located in its natural cellular environment and therefore ideally suited to elucidate the direct physical and biochemical response to global and local changes in the mechanical environment. Hence, we continued to more carefully investigate the apical myosin network structure, which will be discussed in chapter 6 and 7.

Chapter 5

The interconnection of apical actin and myosin networks

5.1 Introduction

In the previous two chapters we described two identified apical network structures in non-confluent ECs: (1) an actin network of microvilli like protrusions with elongated, bent and membrane parallel structure and high dynamic reorganization (chapter 3) and (2) an isotropic myosin network spanning the whole apical cell cortex (chapter 4). Actin as a cytoskeletal key player can build up high order structures such as e.g. stress fibers (Ref.[62]), filopodia or lamellipodia (Ref.[19]) with the help of formins. These dynamic actin structures use polymerization and depolymerization steps to assemble and are thus independent of the actin related motor protein myosin.

On the other hand, it has not been reported so far that motor proteins can themselves form network-like structures. Some of the motor proteins are able to assemble into so called bipolar rods or minifilaments (e.g. kinesin-5 (Ref.[1]), myosin II (Ref.[170])) on length scales of several hundred nanometers. However, these motor proteins are unable to form higher ordered structures on micrometer length scales without the help of the related cytoskeletal counterpart. Thus, the identified apical myosin network must somehow be related to filamentous actin.

As both identified networks are located in very close proximity to each other in the apical cortex region and both structures were interdependent, which we revealed by various drug experiments, we now set out to directly identify their interconnection by co-localization experiments.

5.2 MHCA - Lifeact double transfection reveals only partial co-localization

We already verified by drug experiments, namely blebbistatin treatment (chapter 3.4) on actin-labeled cells as well as LatB treatment (chapter 4.9) on myosin-labeled cells, that the two network structures were interconnected as they both ruptured upon drug treatment to interfere with the protein counterpart. Hence, we now set out to directly visualize and analyze the network interdependency. We first established stable cell lines by transfecting

MHCA-GFP plus Lifeact-mCherry, respectively. Cells were selected using puromycin and hygromycin selection markers (chapter 2.3.1) and stable cells were determined by fluorescence signal. Thereafter, networks in stable cells were visualized to monitor co-localization. Unexpectedly, the two apical structures did not overlap to a large degree but only showed partial co-localization (Fig. 5.1).

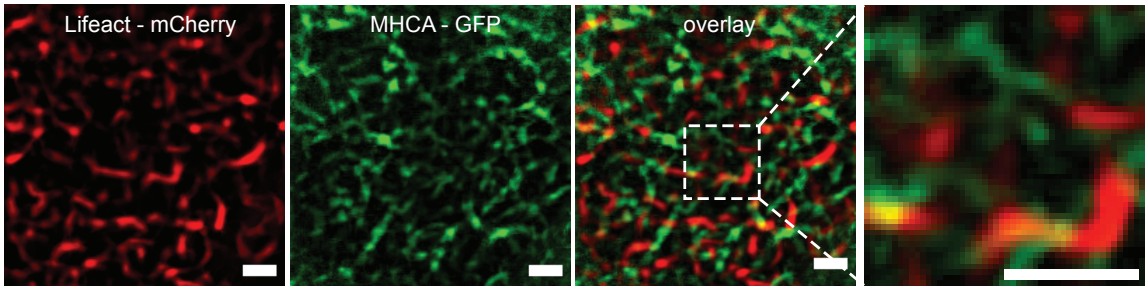

Figure 5.1: Lifeact-mCherry (left) and MHCA-GFP (middle) stably double transfected cells reveal only partial myosin-actin co-localization. Scale bar: 2μm.

It has been reported that myosin II as well as other members of the myosin class can assemble to minifilaments (Fig. 4.1) as independent structural entities up to 300 nanometer in length (Ref.[134],[170]). Nevertheless, the highly structured myosin network was unlikely self-assembling to long filaments rather than presumably aligning along actin structures.

5.3 Actin-myosin dynamics analysis verifies interconnectivity

The hypothesis that myosin aligns along actin structures was supported by the dynamics analysis of double transfected cells. Already by kymograph analysis from time-lapse movies of double transfected MDCK cells we noticed similar patterns of motion for both, myosin (MHCA-GFP) and actin (Lifeact-mCherry) (Fig. 5.2, kymograph). Even non co-localizing actin and myosin structures in proximity to each other frequently moved along in the same patterns changing direction simultaneously.

This interconnection of both networks became even more apparent when performing temporal and spatial correlation analysis. Autocorrelating each channel separately and comparing the obtained results led to similar numbers for both, temporal Pearson and spatial STICS analyses (Fig.. 5.3). As for single transfected cells (chapter 3.3 and 4.6), the correlation times were about one minute (actin: (53 ± 11) seconds, MHCA: (57 ± 20) seconds).

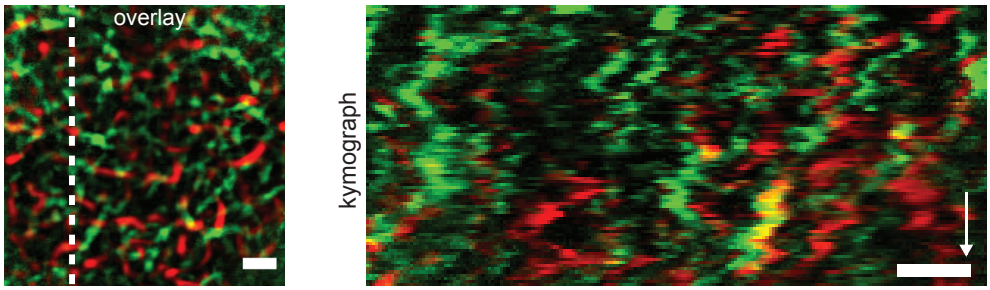

Figure 5.2: Similar actin and myosin dynamical patterns of proximal structures, analyzed by kymograph analysis, indicate mechanical interconnection. Scale bar: 2μm time arrow 400 sec.

Correlation lengths were also comparable with actin at $(2.1 \pm 0.4)\mu$m and myosin at $(3.3 \pm 0.6)\mu$m of correlated length scale. The slight decrease of actin correlation length compared to single transfected cells might be a result of fluorophore change with a resulting decreased signal to noise ratio caused by a quantum yield decrease for mCherry compared to GFP (Ref.[152]).

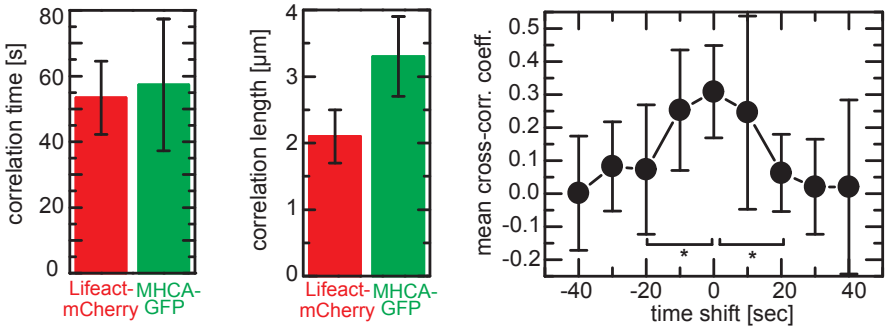

Figure 5.3: Auto- and cross-correlation analysis verifies actin-myosin interconnection. Autocorrelation results exhibit similar time and length scales (left and middle) and cross-correlation coefficients are significantly higher at zero time shift (right). n=8, mean±SD.

Apart from the autocorrelation analysis, performed for the correlation lengths by Dr. P. Diesinger, we used the calculated STICS velocity flow fields to conduct a cross-correlation analysis. The temporal cross-correlations between actin and myosin channels were quantified by Dr. P. Diesinger using the following temporal correlation function:

$$TCF(\tau) = \left\langle \frac{\sum_t \delta v_1(x,y,t) \cdot \delta v_2(x,y,t+\tau)}{\sum_t \delta v_1(x,y,t) \cdot \delta v_1(x,y,t)} \right\rangle_r \tag{5.1}$$

$$\delta v(x,y,t) = (v(x,y,t) - \langle v(x,y,t) \rangle_t) \tag{5.2}$$

Here, $v_1(x,y,t)$ and $v_2(x,y,t+\tau)$ denote actin and myosin vector field velocities, and τ denotes the temporal offset between actin and myosin fields. As an example, TCF(0) equals the mean cross-correlation of the actin and myosin motion fields without a temporal offset, meaning, the average local myosin flow is compared to the local actin motion field.

This cross-correlation analysis allowed us to ask if one network structure follows the other or if actin and myosin rearrange simultaneously without temporal offset (Fig.. 5.3, right). As already suggested by the kymograph analysis presented above, we deduced a significant increase in the cross-correlation coefficient for zero temporal offset. Hence, both structures were mechanically interconnected and moved alongside in conjunction with each other.

5.4 Latrunculin A treatment confirms actin-myosin connection

Even though we already provided strong evidence for a physical link between apical and myosin structures by image analysis methods we again performed drug experiments to visualize the networks interconnection. We now used Latrunculin A (LatA) instead of LatB (as in chapter 4.9), a more potent version of the actin monomer binding drug, to completely disrupt actin filament structures rather than only slightly interfering with the apical network. By using 2μM LatA on either stably single transfected Lifeact-GFP or MHCA-GFP cells we consequently caused a complete rupture of the apical structures within several minutes (Fig. 5.4).

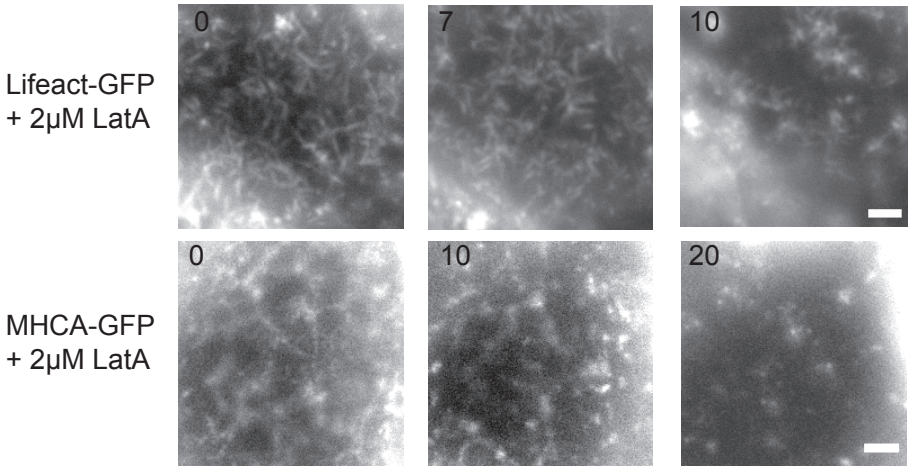

Figure 5.4: 2μM LatA leads to complete apical actin and myosin network disassembly and appearance of small patches within minute time scale. Scale bar: 2μm, time in minutes.

Both, actin and myosin, aggregated within minutes to small patches within the cell cortex. As already mentioned above, the rupture of myosin upon LatA treatment points to actin being the the structural core component of the motor protein network. We assumed that both proteins aggregated into the same patches as described elsewhere (Ref.[98]). To confirm, we repeated the drug experiment and fixed the cells at different time points after drug addition for SEM investigation. The results nicely demonstrated the direct connectivity between the actin filled MV and the prestressed myosin network. After five minutes of drug treatment, the MV were already unevenly distributed on the apical cell cortex (Fig. 5.5, middle). More

importantly, after ten minutes of LatA treatment the MV formed rosette-like patches dispersed throughout the cell cortex (Fig. 5.5, right). We strongly believe that these rosette-like patches correspond to the patches observed in fluorescence images (Fig. 5.4). However, additional experiments using fluorescence combined with SEM have to be performed to further confirm this suggestion.

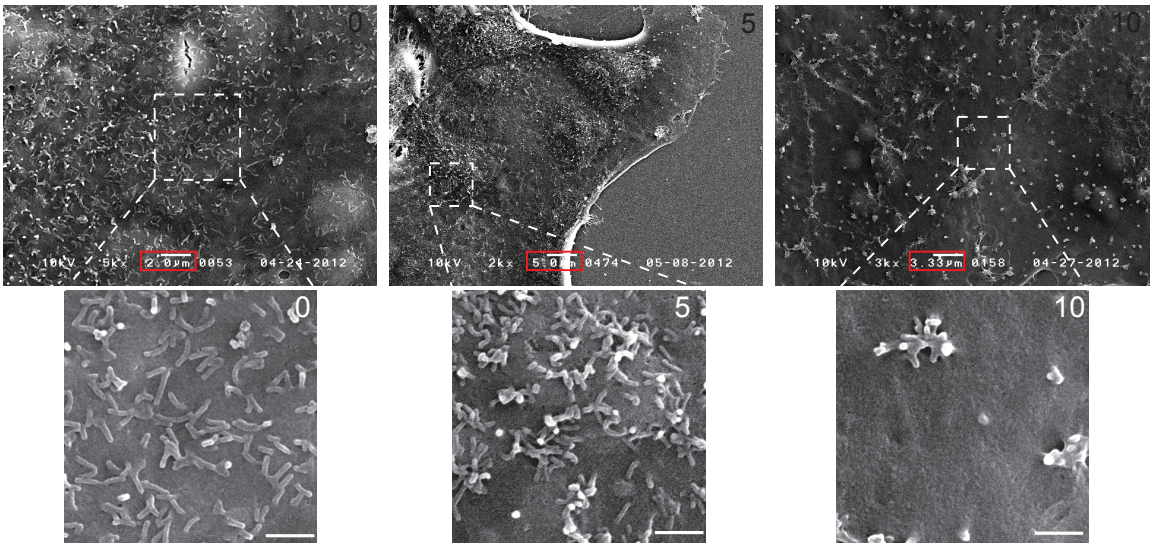

Figure 5.5: SEM analysis at various time points of 2μM LatA treatment depicts surface topology change with clustering MV protrusions presumably being aggregated due to interconnection with the collapsed underlying myosin network. Scale bar top panel: 2μm (left), 5μm (middle), 3.33μm (right), bottom panel: 2μm.

5.5 Discussion - The arrangement of apical actin and myosin

Taking into account all results described above of (1) an actomyosin network under tension, (2) actin-filled partially protruding or membrane parallel MV, (3) partial co-localization but correlated motion of actin and myosin, and (4) the SEM data on LatA treated cells allowed us to draw a hypothetical model of how apical actin and myosin structures are arranged (Fig. 5.6).

The result of only partial co-localization of actin and myosin indicates that actin forms two different network structures: (1) the visible network structure of protruding but mostly membrane parallel MV (Fig. 5.6, thick red protruding bundles) and (2) an innercellular network in close proximity to the apical cell cortex and analogous to the myosin network (Fig. 5.6, thin red membrane parallel meshwork). Why we could not identify this filamentous network remains to be elucidated. All commonly used actin markers, e.g. atto488-phalloidin, Lifeact-GFP, and actin-GFP, did not label the presumably thin actin filaments. One explanation could be that these filaments cannot be visualized against the high background signal of cytosolic actin or they are invisible due to high signals of MV actin. Dr. R. Aufschnaiter from

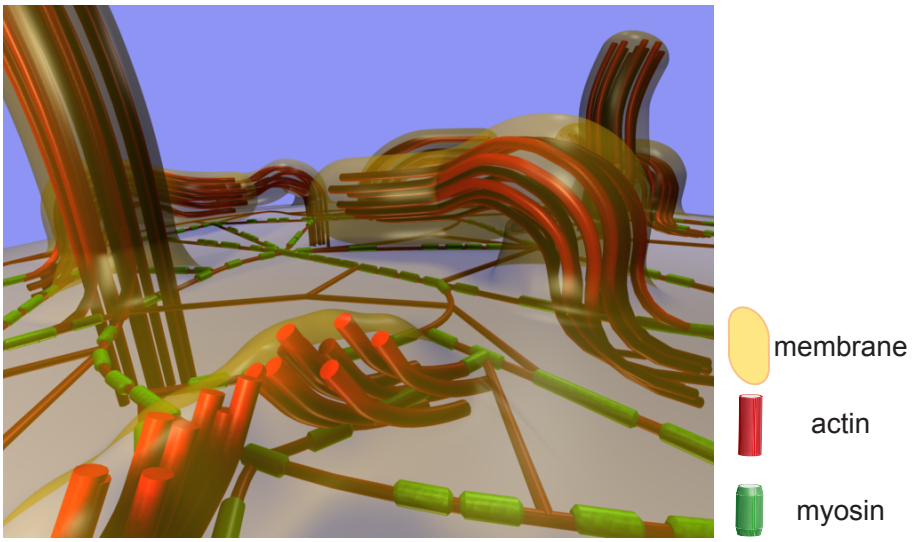

Figure 5.6: Schematic overview of apical actin and myosin network interconnection. Thick MV bundles (red: actin) protrude out of the cell membrane while innercellular, membrane parallel network of thin actin filaments is covered by myosin motors (green) and thereby kept under tension.

our group tried to suppress MV formation by knocking down ezrin of the MV related Ezrin-Radixin-Moesin (ERM) protein family (Ref.[32]) as well as EBP50, an ezrin binding protein important for proper MV formation (Ref.[89],[37]) . However, due to redundancy effects of these proteins, this approach failed. Nevertheless, LatA or LatB experiments demonstrate the existence of filamentous actin within the myosin network. To verify the assumed existence of cortical actin filaments, ultrastructural analysis will be a necessary step in future investigations.

A major finding of this work is that an extensive, isotropic network of myosin filaments spans the innercellular apical cortex of non-confluent epithelial cells. This myosin network is however discontinuously aligning along the thin actin meshwork. This feature of alternating localization proofs to be very efficient for the generation of contractile forces (Ref.[92]). Not only does this actomyosin network keep the apical surface under tension, hence under physical control, it also rearranges dynamically the network interlinked protruding MV, resulting in topology and membrane organization modifications of apical regions on micrometer length scales. This apical cortex organization constitutes a particularly interesting case of an active biopolymer network with molecular motors modifying the topology of a semi-flexible polymer mesh (Ref.[80],[81]). Most of the studies on active cytoskeletal networks have so far been carried out using *in vitro* approaches. In contrast, the myosin II probes are now optimally suited to visualize a quasi two dimensional acto-myosin network in its biological environment in a broad range of epithelial cells (Fig. 4.4). It will be of high interest in future studies to gain insights in the characteristics of these networks such as the self-organization processes of network classes (Fig. 4.6), large scale reorganizations without prominent stable reference points (e.g. focal adhesions or adherens junctions), and the role of tension versus flexibility within the network for optimal cellular adaptability to inner- and extracellular signals.

Apart from the organizational aspects concerning the newly identified apical actomyosin network the described system with the interlinked MV protrusions comes as an excellent experimental probe for ongoing discussions regarding the physical basis for MV assembly, protrusion and its broad cell dependent variability in shape. Bent apical protrusions in epithelial cells have already been seen in micrographs from the 1970s (Ref.[13],[20]). More recently, atomic force microscopy (AFM) of MDCK or melanoma apical cell surfaces has revealed ridge-like topological structures (Ref.[129],[128]). Additionally, various models have been proposed to shed light on the underlying physics leading to cell protrusions in all variations (Ref.[42],[183]). However, most studies lack a tunable system with which theoretical approaches could be tested. The here described actomyosin network with the interlinked, partially bent shaped, MV protrusions is an ideal system to address open questions. How and where do the pushing forces during MV constituting actin polymerization link into a supporting semi-flexible mesh bearing the pushing forces (Fig. 5.6, schematic front)? How is this interconnection between MV and apical actomyosin network set up regarding protein complex formation? These questions, amongst others, remain to be elucidated in future experiments. Very promising first studies on the EBP binding protein EPI64 already indicate specific microvillar subdomains at its base with very distinct protein composition (Ref.[49]).

Irrespective of its potential role in membrane organization, the apical actomyosin network is ideally positioned to act as a mechanosensory element. The network provides at the same time mechanical resistance as well as flexibility for morphological adaptations upon external mechanical or chemical stimuli (Ref.[112],[118]). Keeping the apical cell cortex under tight control is a basic necessity for non-confluent cells exposed to a more varied environment as compared to confluent cells. Furthermore, a mechanosensory function might not be limited to the cell cortex, as it has recently been proposed that mechanical forces acting on the cell nucleus directly influence transcriptional activities (Ref.([76],[77], [154],[162]). Thus, elucidating the apical actomyosin network response to local or global changes in the mechanical or chemical environment will be a very exciting path to follow in future research.

Chapter 6

Image analysis approaches for biophysical network characterization

6.1 Introduction

Ever since the discovery of the green fluorescent protein (GFP) by Shimomura *et al.* (Ref.[153]) and its determination of the characteristic emission spectrum with a sharp peak around 508nm (Ref.[71]) GFP has become a highly valuable and irreplaceable biomarker in various fields of biological research (Ref.[167],[182]). Especially cell and developmental biology have experienced tremendous progress and intriguing new insights into cellular behavior within the last decades based on GFP and fluorescence microscopy. Different to other standard techniques which involve cell fixation and staining procedures the usage of GFP allows to tag and visualize specific proteins in living cells. This live cell imaging technique opened a broad new field of research that could focus on important questions regarding e.g. cell regulatory processes, cell structure and protein localization as well as cellular response and adaptation upon external stimuli.

Along with this new biological marker, that could via cloning and transfection be inherently expressed in cells, various novel fluorescence microscopy techniques have been developed in recent years. Depending on the experimental needs a broad range of microscopy with characteristic properties is now available ranging from standard wide field, confocal, spinning disk setups (Ref.[122],[43]), specified systems such as total internal reflection fluorescence (TIRF), fluorescence recovery after photobleaching (FRAP), fluorescence resonance energy transfer (FRET) or fluorescence lifetime imaging microscopy (FLIM) (Ref.[67]) to highly sophisticated light sheet or super resolution microscopy (Ref.[63]).

Resulting from the advances of microscopy techniques the obtained experimental raw data increased significantly over the last years. The use of high definition charge-coupled device cameras (CCD) together with high resolution optical setups and technical advances to perform long time measurements eventually lead to the necessity of developing new computer based analysis tools for data mining purposes. As for that, various new image analysis methods have evolved lately ranging from simple particle tracking approaches to highly advanced image correlation spectroscopy (ICS) methods (Ref.[53], [82]) such as e.g. STICS described in chapter 3.3.2. In developmental biology for example, the use of novel image analysis techniques led to intriguing new insights of pulsatile epithelial tissue-level morphology change driven by the actomyosin cytoskeleton and leading to constriction and tissue closure during the morphogenesis of *Drosophila melanogaster* (Ref.[133],[105],[104],Ref.[155]). Moreover, only by high

definition fluorescence microscopy combined with extended image analysis, namely particle image velocimetry (PIV), Rauzi *et al.* (Ref.[132]) could show that only the tightly controlled oscillatory interplay of actin and myosin distributions can reshape cellular morphology. Notably, the oscillatory pattern of actomyosin localization and activity plays a crucial role for the proper function of these morphogenetic processes (Ref.[92]). These remarkable results, all based on advanced image analysis methods, demonstrate the importance of not only gathering fluorescence images but also using sophisticated analysis tools to extract valuable information.

Here, we present three image analysis techniques that have been developed during this thesis to study the apical myosin network dynamics: (1) highest intensity tracking, (2) incremental temporal image correlation (ITIC), a novel technique based on comparison of characteristic decay constants and (3) optical flow analysis. As results from previous chapters imply that the cortical myosin network structure plays a crucial role for cell shape regulating processes we developed these three analysis techniques to gain insights into the dynamical behavior of the cortical network. While for the highest intensity tracking approach we obtain only basic information regarding mean velocities and direction of movement the new ITIC method returns detailed and novel dynamical characterization data. We find that the myosin network structure is not reorganizing continuously but is changing between states of high and low reorganization speed. We confirm by comparison the existence of such oscillatory reorganization pattern applying the third developed tool of optical flow analysis. Moreover, we describe our method to extract comparable parameters characterizing dynamics such as mean optical flow velocity, activity potential and oscillation period from the calculated optical flow velocity vector fields. The here presented standardized version of the optical flow analysis will in the subsequent chapter 7 then be used for experimental comparison of network dynamics upon various interferences.

6.2 First approach: Highest intensity tracking

Our first approach to characterize myosin network dynamics was based on highest intensity tracking. Thus we had to set a threshold value to define highest intensity. After our standard filtering and maximum projection routine (chapter 2.5.1 and chapter 4.5), we used the threshold defining Otzu method to compute a global threshold level. Briefly, Otzu method iterates all possible threshold values to minimize the intraclass variance of background and signal pixels by assuming that there is a bimodal distribution of gray-level values (Ref. [119]). We then empirically and arbitrarily defined highest intensity to be ($I_{\text{high}} > 1.5 \cdot \text{threshold}$) and binarized the image according to this threshold.

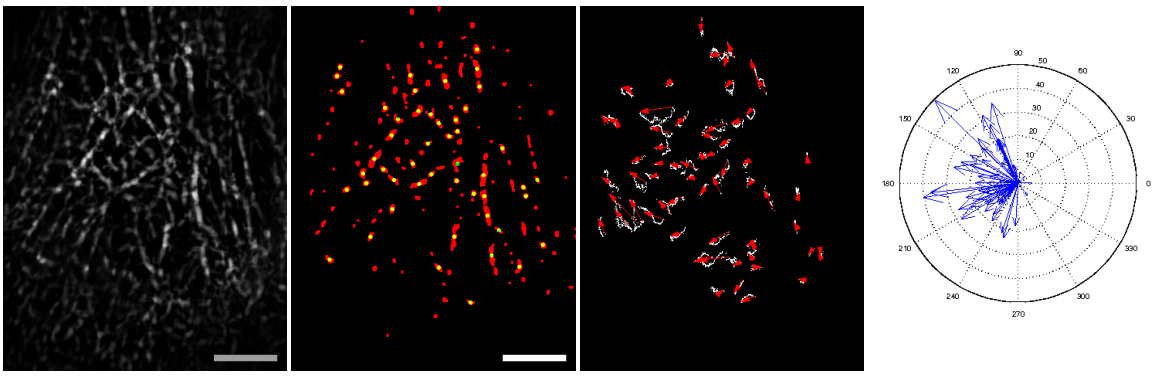

Figure 6.1: Highest intensity tracking image processing routine shown exemplary for image of MHCA-GFP cortical network (left). Binarized image of intensities higher I_{high} (red) with respective calculated center of mass (CoM, yellow dots) (middle left) as well as traces and direction of CoM movement of image sequence (middle right). Compass plot depicts CoM direction of all obtained traces (right). Scale bar: 5μm

Exemplary, a filtered and maximum projected image of MHCA-GFP (Fig. 6.1, left) as well as its highest intensity binarized versions (Fig. 6.1, middle left, red objects) depict the image processing routine. Note, that we performed one morphological opening procedure (erosion before dilation) using a 3x3 matrix of 1s to smooth object contours and break thin connections as well as thin protrusions. As a next step to follow the motion, we calculated the center of mass (CoM) for each highest intensity object (Fig. 6.1, middle left, yellow dots) that was in x- and y-dimension larger than 5 pixels. By applying this method to each frame of a time-lapse movie we obtained a sequence of center of mass motion. The CoM motion movie sequence was subsequently traced using a particle tracker plugIn of ImageJ (Ref. [147]) and the obtained traces analyzed using Matlab. Parameters such as direction of movement (Fig. 6.1, middle right, and compass) as well as displacement and mean velocity were recorded for each trace longer than 20 or 50 frames depending on the overall length of the timelapse movies and Δt between frames.

Though the algorithm worked fairly well, the highest intensity tracking had two key drawbacks: (1) its sensitivity to intensity fluctuation leading to jumping CoM points and (2) its

sensitivity to unevenly distributed signal intensity. We could not circumvent the first problem during microscopy but had to incorporate additional program instructions to counterbalance the CoM jumping behavior. The second problem we tried to eliminate by segmenting movies into smaller parts before analysis. In this case, the intensity would be less unevenly distributed leading to an increase in highest intensity objects.

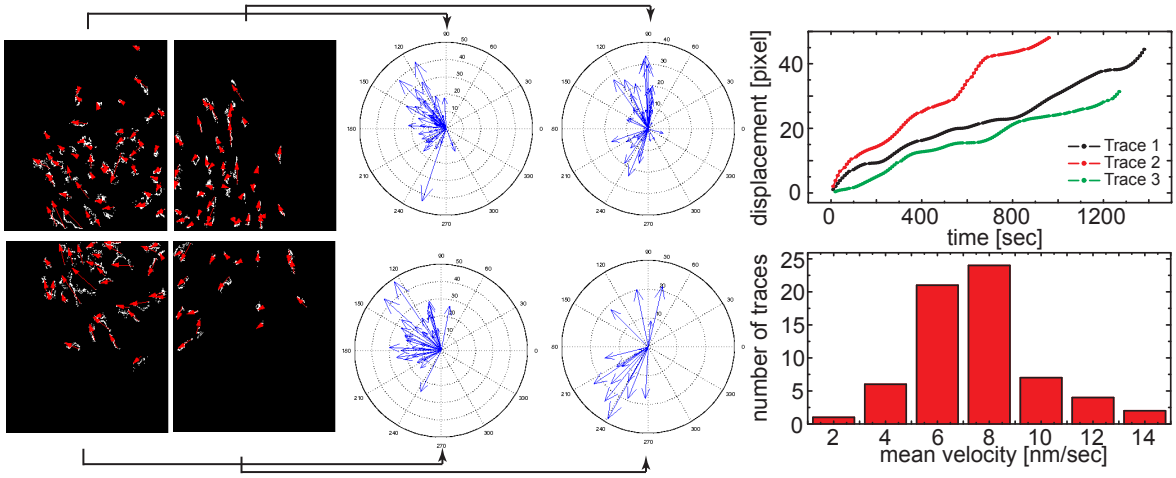

Figure 6.2: Refined version of highest intensity tracking includes segmentation of movies (left) and subsequent CoM analysis being more sensitive to direction distribution (middle).Displacement analysis (upper right) and mean velocity distribution (lower right) of CoM traces reveal stop-and-go motion and mean velocity of about 8nm/sec.

As intended, we could significantly increase the trace density by segmenting the time-lapse movie into four parts (Fig. 6.2, left) compared to the uncut version (Fig. 6.1). Furthermore, this optimization step resulted in a growing algorithm sensitivity to the direction of motion. We were now able to show that different sub-cellular regions of the cortical myosin network were moving in different directions concurrently (Fig. 6.2, middle).

Additionally we analyzed single CoM motion traces in detail by calculating the displacement over time (Fig. 6.2, right, upper panel) or the mean square displacement (not shown). Moreover, we deduced the mean velocity per trace by taking the slope of a linear fit to the obtained displacements. This resulted in a mean velocity distribution around 8nm/seconds (Fig. 6.2, right, lower panel). However, this value was strongly dependent on whether we smoothed the displacement curves (as in Fig. 6.2, right, upper panel) using a local regression function of Matlab (smooth: 'rloess') to balance out the CoM jumping, or whether we analyzed the raw data (as in Fig. 6.2, right, lower panel). In summary, this highest intensity approach was due to these reasons and a very large parameter space not as robust as necessary to perform comparable image analysis. Nevertheless, we could deduce one important finding from this approach, namely the existence of a 'stop-and-go motion' behavior visible in the displacement curves of exemplary traces (Fig. 6.2, right, upper panel). This finding will become important again in the the subsequent section 6.3.

6.3 Second approach: Incremental temporal image correlation (ITIC)

As the highest intensity tracking approach turned out not to be suitable, we developed a novel algorithm to determine motion patterns within the reorganizing cortical myosin network. Object identification based approaches appeared to be too error-prone. Hence we set up an analytical tool that could measure reorganization without the need of identifying structures. We used again the temporal image correlation with the equation for PCF (equation 3.3) and the exponential decay fitting equation f(t) (equation 3.4). As already discussed in chapter 3.3.2, the temporal correlation analysis results in a characteristic decay constant τ_i describing how fast the system reorganizes.

For our new incremental temporal image correlation approach (ITIC) we modified our algorithm in the way that we now not only calculated r(t), f(t) and τ_i for the first frame of a time-lapse movie as reference frame U(x,y,0). In contrast, we incrementally increased the reference frame and calculated the characteristic decay constant τ_i for each U(x,y,t_i) (Fig. 6.3, scheme, upper panel and work flow chart). We noticed that the exponential functions f_i(t) decayed with varying decay rates (Fig. 6.3, lower panel, left). To see differences between slow and fast reorganization we plotted the inverse characteristic decay time ($1/\tau_i$) over time t_i. Low $1/\tau_i$ values then correspond to slow reorganization while large $1/\tau_i$ values correspond to fast reorganization (Fig. 6.3, lower panel, right).

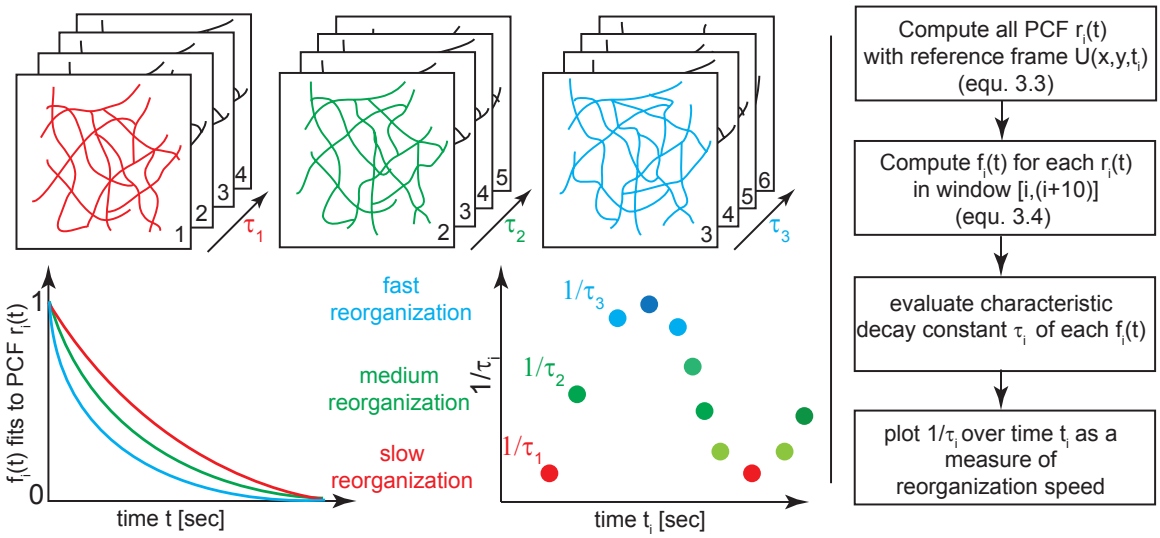

Figure 6.3: General concept and workflow of ITIC method: temporal correlation and subsequent calculation of characteristic decay constant τ_i for each frame i as reference frame (upper panel) results in comparable data when plotted as inverse ($1/\tau_i$) and over time t_i (lower panel). Slow reorganization for high *tau* values and fast reorganization marked by low *tau* values.

Considering the finding of stop-and-go motion from the previous section and assuming that this feature is not locally restricted but a global feature of the myosin network, we would

expect that the ITIC analysis curve ($1/\tau_i$ over t_i) continuously oscillates between states of slow and fast reorganization. As expected, we were able to see this oscillatory ITIC curve behavior in various cells (Fig. 6.4, middle). However, the ITIC method has the drawback of oversampling as it uses several consecutive frames of one reference frame for calculating the PCF. Though these consecutive frames will then be reference frames themselves in the next incremental step. To minimize this oversampling we only considered the flanks (Δ 10 frames) of the decay curves $f_i(t)$ for τ_i-calculation (Fig. 6.4, left). This strategy increased the error of the fit but did not change the overall ITIC curves.

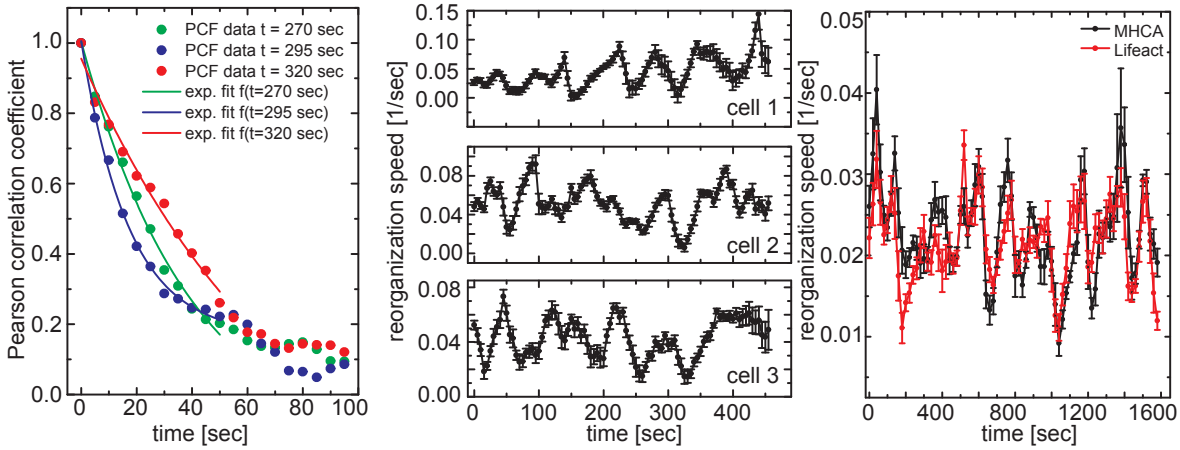

Figure 6.4: ITIC analysis applied on network images sequences reveals oscillating reorganization speed (middle). To minimize oversampling only flank of $f_i(t)$ is used for τ_i calculation (left). ITIC curves of MHCA-GFP/Lifeact-mCherry double transfected cells demonstrate similar ITIC results (right).

To ensure that we did not pick up any artificial oscillation but monitored the reorganization speed of the isotropic cortical myosin we compared the ITIC curves from stably double transfected MHCA-GFP/Lifeact-mCherry cells. Both myosin and actin dynamics followed the same pulsatile reorganization speed patterns (Fig. 6.4, right) which thereby confirms that the ITIC analysis method robustly tracks changing dynamical behavior independent of the observed structure itself. Data presented in chapter 5 show that myosin and actin appeared in different arrangements at the apical cell cortex of non-confluent cells though being dynamically linked. The close resemblance of the here deduced ITIC curves underline this interdependency of myosin and actin structure once again.

As a last step we automized the ITIC approach using Matlab instead of Origin8 for the exponential fitting procedure. Even though the exponential decay fitting algorithms of Origin8 and Matlab differ, we obtained as expected similar results for the ITIC curves (Fig. 6.5, left) regarding the position of peaks. The reason why the Matlab fitting procedure had slightly shifted peak times compared to the Origin fitting we were not able to clarify. Nevertheless, the similarity between ITIC curves was sufficient to implement large scale analysis by automatically calculating the reorganization speed curves of many cells simultaneously (Fig. 6.5, right). The obtained results infer that there is a huge heterogeneity in intensity and timing of oscillating reorganization speeds.

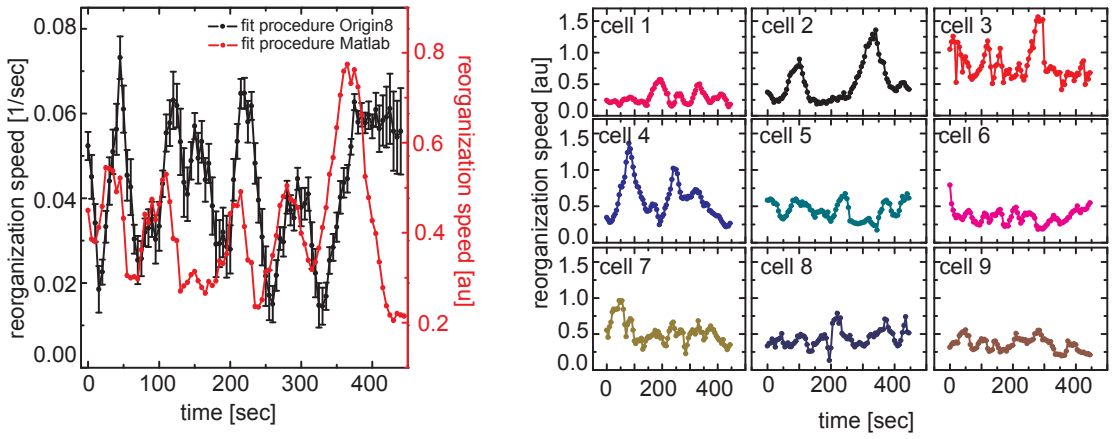

Figure 6.5: Automized ITIC analysis pipeline using Matlab resembles acquired data using Origin for fit procedure (left) though fit algorithms differ slightly. Matlab pipeline however allows for fast automized analysis of many cells thereby revealing heterogeneity of oscillation behavior (right).

6.4 Third approach: Optical flow analysis

Even though we were able to pinpoint global features of the myosin network dynamics using the ITIC approach we subsequently set out to gain further detailed information about local dynamic variations. As a prerequisite we had to develop an image analysis tool that could track the behavior of single reorganizing structures without the need of object identification. Here we identified the optical flow method to be ideally suited for the task as it computes a velocity vector in the direction of movement for each pixel of an image rather than tracking the movement of identified objects. Particle image velocimetry (PIV), the other frequently used approach for detailed flow analysis, was no alternative to us as we were not able to incorporate tracer particles in the myosin network structure. This is however a precondition to use PIV.

As this third approach of the optical flow analysis will be the underlying method for most of the following experimental results we will here describe the theory, function and adaptation for our purposes briefly.

6.4.1 Theoretical background

Optical flow estimation is in principle based on the comparison of two images that are related by a motion event between the images. The method is then used to calculate the displacement field between the two images taking into account the correspondence between pixels of the images (Ref.[12]). We will discuss briefly the first theoretical approaches of Horn and Schunck for optical flow estimation (Ref.[61],[96]) using exemplary images to illustrate the workflow.

Let I(x,y,t) be a gray value image at time t with a defined brightness pattern. At time (t+δt) this image has moved slightly and will now be described as I(x+δx,y+δy,t+δt). Now the assumption Horn and Schunck (Ref.[61]) made, is that the gray values at the points (x,y) do not change significantly. This is the so called 'gray value constancy assumption' which underlies all optical flow approaches. Based on this assumption we can now write:

$$I(x,y,t) = I(x+\delta x, y+\delta y, t+\delta t) \quad (6.1)$$

$$= I(x,y,t) + \delta x\frac{\partial I}{\partial x} + \delta y\frac{\partial I}{\partial y} + \delta t\frac{\partial I}{\partial t} + \epsilon \quad (6.2)$$

Here the right part of equation (6.1) has been expanded using first order Taylor approximation (equ.6.2). ϵ in equation (6.2) marks second and higher order Taylor terms. Subtracting I(x,y,t) on both sides and dividing by δt results in:

$$\frac{\partial I}{\partial x}\frac{dx}{dt} + \frac{\partial I}{\partial y}\frac{dy}{dt} + \frac{\partial I}{\partial t} + \Theta(\delta t) = 0 \quad (6.3)$$

$\Theta(\delta$t) as a term of order δt (assuming that δx and δy vary as δt) will approach zero in the limit of δt$\rightarrow$ 0 leading to:

$$\frac{\partial I}{\partial x}\frac{dx}{dt} + \frac{\partial I}{\partial y}\frac{dy}{dt} + \frac{\partial I}{\partial t} = 0 \quad (6.4)$$

With

$$\mathrm{u} = \frac{dx}{dt} \qquad \mathrm{v} = \frac{dy}{dt} \quad (6.5)$$

and the partial derivatives put to abbreviations I_x, I_y and I_t equation (6.4) is now in the famous formulation (Ref.[61]):

$$\mathrm{I}_x\mathrm{u} + \mathrm{I}_y\mathrm{v} + \mathrm{I}_t = 0 \quad (6.6)$$

This equation does however not constrain the flow sufficiently as it is one equation for two unknowns u and v. At this point of calculation the various now available optical flow estimation methods vary significantly depending on additional constraints put into the estimation (Ref.[12]).

For reasons of understanding we here present a simple example with arbitrary test images to demonstrate the workflow. Let us take a grayscale image (Fig. 6.6, upper panel, Im1) and rotate it slightly to mimic motion (Im2). Calculating I_t =Im1-Im2 is simple as well as taking the partial derivatives I_x and I_y (Fig. 6.6, lower panel). In simple words, the task of the optical flow algorithm is to find the correct vector flow fields u and v that transform the images I_x and I_y to image I_t. Note here that the optical flow method is very sensitive to edge detection. To illustrate this feature we plotted the intensity profile of an edge (Fig. 6.6, right, upper scheme) and its derivative intensity profile (Fig. 6.6, right, lower scheme). The same effect is reflected in the partial derivates of the test image, where edges appear as high or low intensity while smooth surfaces do not show detailed information.

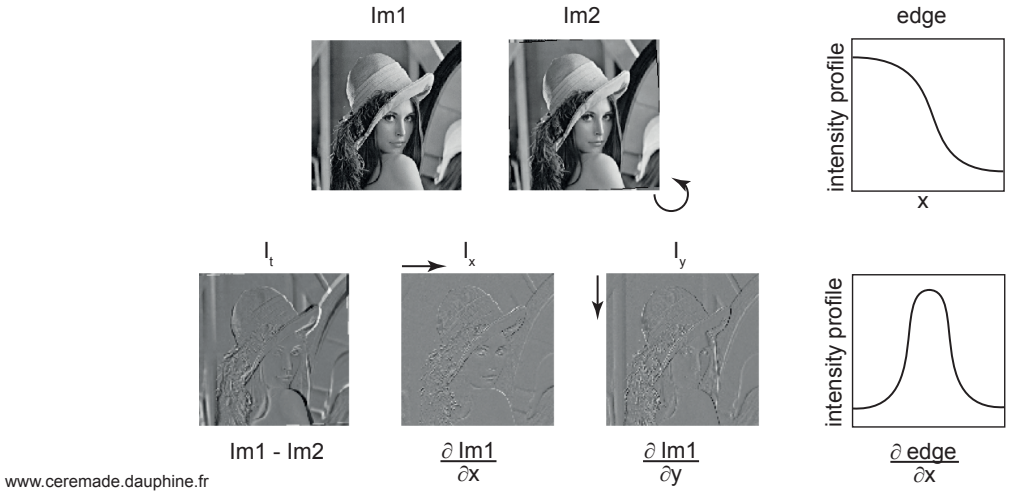

Figure 6.6: Schematic example of image treatment for optical flow analysis: Im1 and slightly rotated Im2 (upper images) are on one hand subtracted with resulting time derivative Dt as well as partial derivatives of Im1 in direction of x and y (lower images). Flow vector field define transformation to minimize image difference between Dt and Dx, Dy. Edge intensity profile and its derivative depict edge-sensitivity of optical flow.

In the course of this study we implemented and adapted an already existing Matlab algorithm, which is accessible on the MatlabCentral server (www.mathworks.com/matlabcentral/) named *High accuracy optical flow* (FileID: 17500). This algorithm, based on the work of Sand and Teller (Ref.[12],[145]), is a very sophisticated program that combines various constraints, assumptions and strategies to calculate the optical flow. It implements a coarse-fine strategy using a warping technique as well as a non-linearized, variational model to numerically evaluate equation (6.6). This algorithm is ideally suited for our purposes as it extends the gray value constancy assumption by a gradient constancy assumption that makes the method robust against gray value changes (Ref.[12]). Moreover it introduces a smoothness assumption that accounts for possible interaction between neighboring pixels and extends the computation to textureless regions. This inclusion of textureless regions is important for our analysis as the myosin network images exhibit high amounts of textureless regions that yet have to be considered in the calculations.

For very detailed information regarding the algorithm function and structure we refer to Ref.([12]) and the description of the Matlab implementation accessible at MatlabCentral server (see above). Here, we only want to briefly describe two features of the algorithm: (1) the coarse-fine approach and (2) the general work chart of the program (Fig. 6.7). The coarse-fine approach includes a very sophisticated warping technique based on the so called 'Laplacian pyramid' by constructing an image pyramid consisting of coarse (level 0) to fine (level 50) resolved images. First, the coarsest image level 0 (Fig. 6.7, left) of the pyramid is used to calculate the optical flow vector fields u,v which are then used to initialize a finer image level using a warping technique. Details about this technique, which has originally been developed for 3D movie animations, can again be found in Ref.([12],[5],[110]). Without going into detail, this warping implementation produced an incremental increase in image

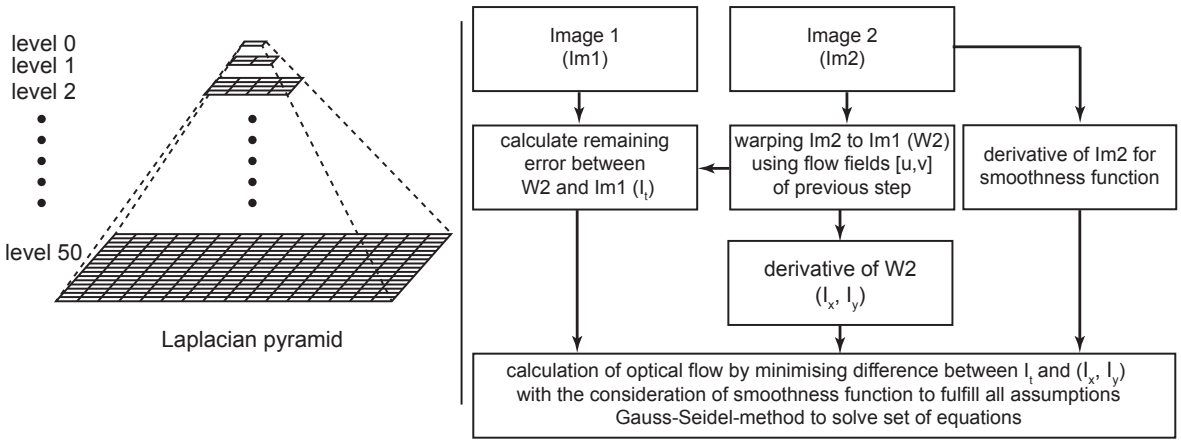

Figure 6.7: Laplacian pyramid scheme to demonstrate coarse-fine strategy (left) and workflow chart of optical flow algorithm depicting general image processing steps to calculate optical flow (right)

refinement (6.7, right W2) leading to faster convergence of the iterative algorithm for the linearized energy equations and thus resulting in a strong decrease of computation time. As we intended to use this algorithm on huge amounts of data, this strong decrease in computation time by applying the coarse-fine strategy was an important feature of the adapted program.

6.4.2 Adaptation and tests

The optical flow algorithm from the MatlabCentral server was optimized for RGB color images. As we were only dealing with gray scale images we had to adapt the program to fit our requirements. However, we did not optimize the algorithm by diminishing the three channels (RGB) back to one signal channel (gray scale). This optimization step would significantly decrease the calculation time though extensive programming would be needed.

We used the program as provided and just optimized parameters to calculate the optical flow of simple gray scale images with low amounts of detail. To test the functionality of the algorithm we first used a test stack of two binary bricks shifting horizontally against each other (Fig. 6.8, left). The resulting optical flow was locally restricted to the edges of the bricks (Fig. 6.8, left ,middle panel and Fig. 6.6). The calculated normalized rotation revealed the correct movement correlated rotation leading to clock- or counterclockwise curls (Fig. 6.8, left, lower panel).

To more closely mimic our image signals we continued the tests by blurring the binary bricks using a gaussian filter (Fig. 6.8, right, upper panel). The resulting general flow intensity behavior was comparable to the binarized bricks (Fig. 6.8, left). However, due to the gradual intensity decrease within the bricks the inner-brick regions were taken into account as part of the moving object. This is reflected by enhanced flow intensities between the pairwise two highest flow intensity regions (Fig. 6.8, right, middle panel). Moreover, the normalized clockwise rotation between the two bricks enhanced due to the smoothness function (Fig. 6.8, right, lower panel).

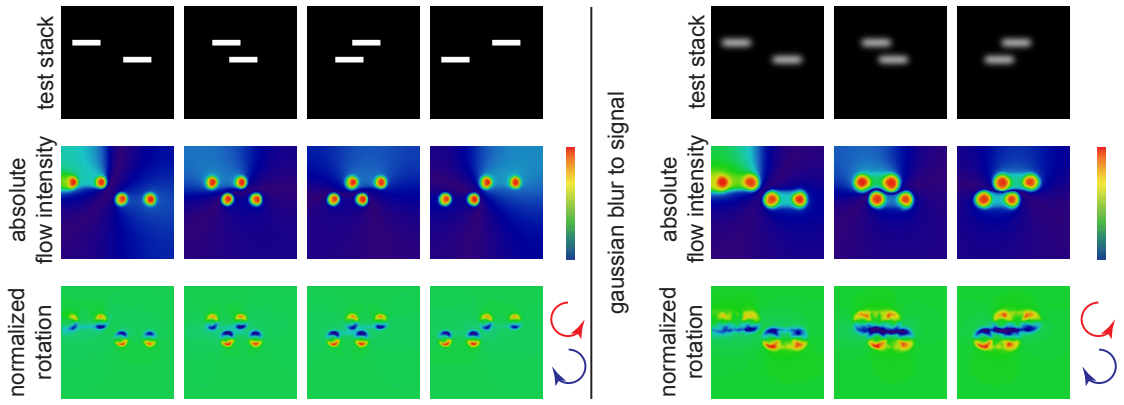

Figure 6.8: Simple optical flow test sequence using two horizontally sliding bricks. Absolute optical flow intensity is restricted to edges of bricks while normalized rotation depicts physically correct curls in flow fields (left). Additional gaussian blurring of sliding bricks results in extrapolation of flow to inner-brick regions as well as increase in rotation intensity (right)

As a further step we continued using four instead of two bricks moving against each other at varying vertical distance (Fig. 6.9, left, upper panel). The overall absolute flow intensity behavior was equivalent to the test stacks before. Importantly though, a distinct difference was detectable as the black regions between the two left and the two right bricks were now automatically estimated to follow a directed flow as well (Fig. 6.9, left, middle panel). Even without any structural information the optical flow algorithm extended the movement due to the smoothness assumption. This was a very important feature for subsequent algorithm application to deduce myosin network flow as there were also large regions without fluorescence signal in the time lapse movies. However these regions were nonetheless moving as shown by calculating the correlation length of 3μm (chapter 3.3.2 and Fig. 4.6). In addition, normalized rotation robustly reflected curl formation with increased rotation intensity between the bricks passing each other more closely (Fig. 6.9, left, lower panel).

With positive test results in hand we continued our analysis tool development by setting up a standardized workflow procedure (Fig. 6.9, right). We first distinguished between the time lapse movie differences regarding the Δt of consecutive frames. For long time scales of $\Delta t = 60$ seconds to observe long range cell cortical myosin reorganization we calculated the optical flow between consecutive frames (Fig. 6.9, right, lower path). In contrast, for short movie time scales of $\Delta t = 5$ seconds we had to introduce a slight oversampling to increase the difference between images for the optical flow calculation (Fig. 6.9, right, upper path). We empirically deduced an oversampling of one image to work best at a time scale between $\Delta t = (2 - 10)$ seconds meaning that we used the next but consecutive frame for optical flow calculation. As a final step we performed a five frames running averaging on the obtained flow intensity sequences to enhance the long lasting dynamic changes and omit appearing short time flow events due to local intensity fluctuations in the time lapse movies.

Having set the complete algorithm pipeline we finally calculated the optical flow of the apical cell cortical myosin network measured on different time scales. The flow analysis on long time

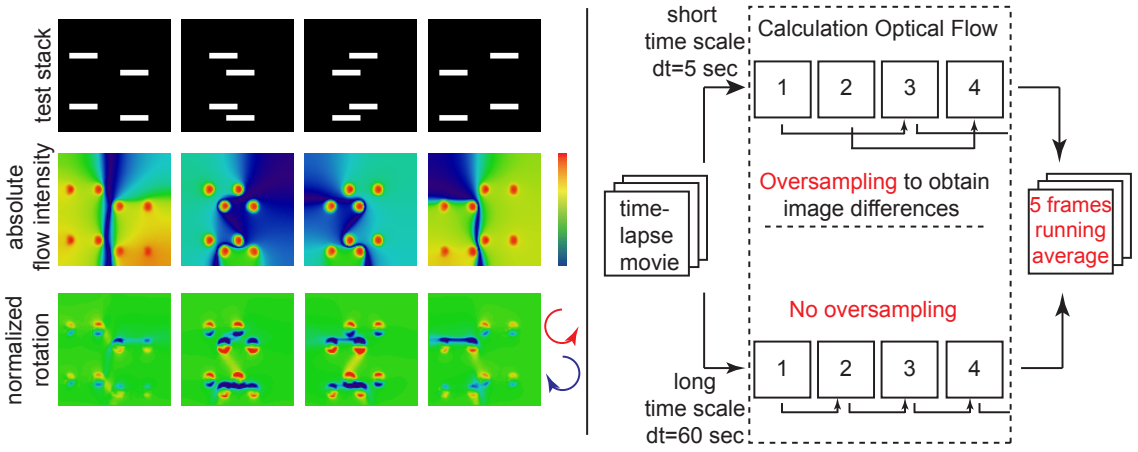

Figure 6.9: Test sequence using four bricks depicts functionality of smoothness function leading to estimation of flow in textureless regions between bricks (left). Workflow chart depicts image sequence processing including incorporated one frame oversampling for short time scale or consecutive frames flow calculation for long time scale sequences (right).

scales of $\Delta t = 60$ seconds (Fig. 6.10, up and middle) nicely depicted spatial and temporal differences in motion within the cell cortex network structure being either highly dynamic or relatively static at different time points. The normalized rotation unfortunately did not show any significant feature that we could extract for subsequent analysis (Fig. 6.10, lower panel).

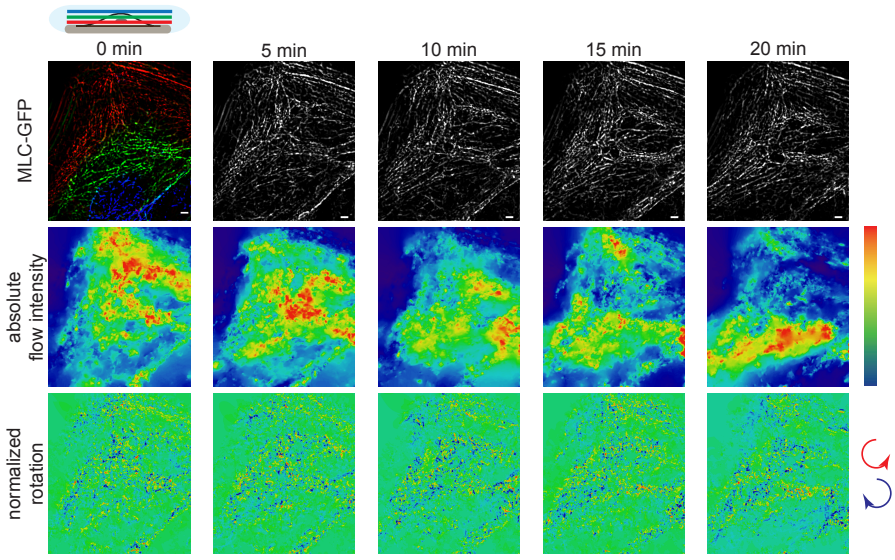

Figure 6.10: Optical flow analysis of MLC-GFP image sequence (upper panel) with $\Delta t = 60$sec between consecutive frames illustrates spatial and temporal variations of absolute flow intensity within cell cortex (middle panel). Normalized rotation does not resolve significant features of movement (lower panel). Scale bar: 2μm

We concluded from the finding of regional dynamic network differences over time (Fig. 6.10) that the global long time scale optical flow analysis had to be complemented by a local optical flow analysis on short time scales to gain further detailed information regarding dynamical reorganization. Therefore we adapted the optical flow to analyze 200x200pixel (12.8x12.8μm) cut sections of short time scale movies (Δt = 5 seconds) (Fig. 6.11, upper panel). The defined area of 200x200 pixels for each measurement of network behavior would later allow for comparison between different batches of cells during e.g. drug experiments. After cutting we calculated the optical flow with an oversampling factor of one frame, as depicted above (Fig. 6.9, right, upper path), to bypass the only marginal differences between consecutive frames on this time scale. As for the long time scales the optical flow intensity changed significantly over time and in its spatial distribution (Fig. 6.11, middle panel). Hence this analysis allowed to gather very detailed information regarding the local features of the apical myosin network dynamics.

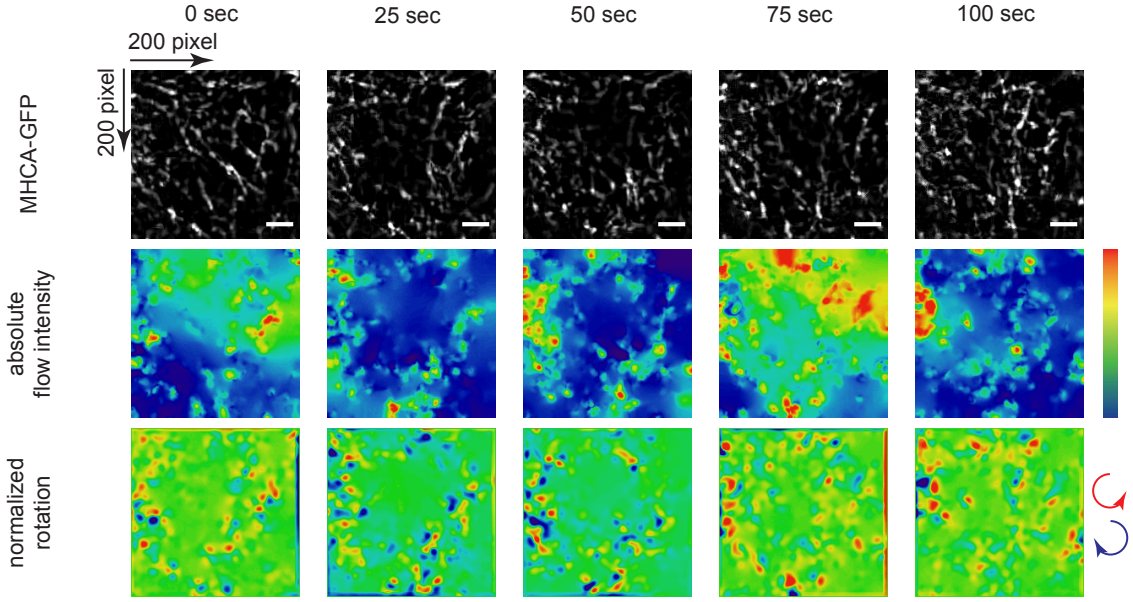

Figure 6.11: Optical flow analysis of MHCA-GFP image sequence (upper panel) with Δt = 5sec reveals detailed information regarding local features of apical myosin network dynamics as optical flow intensity differs in space and time (middle panel).Normalized rotation depicts points of curls in cortex (lower panel).Scale bar: 2μm

6.4.3 Parametrization of optical flow

Having accomplished to visualize the myosin dynamics with the two mathematically derived vector flow fields u and v (equation 6.6) we subsequently focussed on the question which parameters we could extract from the flow analysis to enable comparison between different cells and experimental situations. In a first attempt we followed the nice approach of Serra-Picamal *et al.* (Ref.[151]) to compress the absolute flow intensity sequence along either x- or

y-dimension and image by image thereby obtaining a flow kymograph (Fig. 6.12, upper panel, left). In Ref.[151] this method nicely revealed global cell sheet wave patterns, which are not directly detectable in the flow maps. In our experiments though, we lacked a defined symmetry axis necessary for that analytical approach as we could not predefine a rule for a symmetry axis alignment on an isotropic network. Hence, this compression approach appeared to be unsuitable for our purposes.

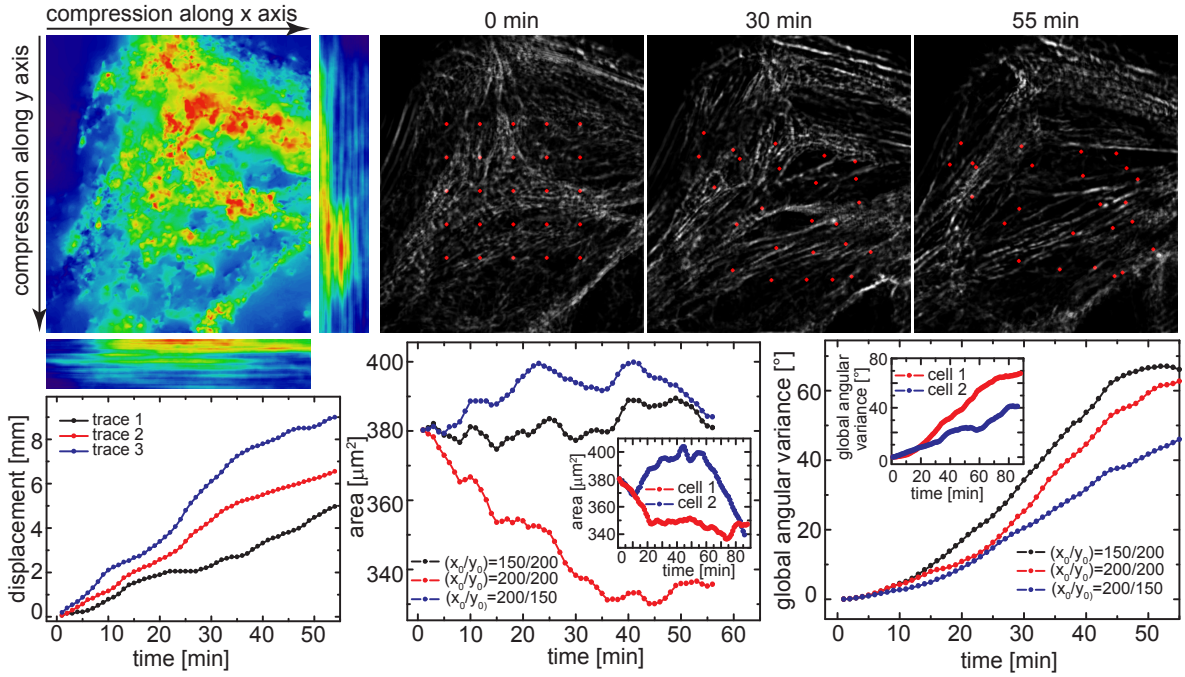

Figure 6.12: Image by image compression along either x- or y-axis leads to flow kymographs (upper left). Use of 'virtual beads' grid allows for analysis of displacement, overall grid area and angular variance over time (upper right and lower panel). Different localization of grid on flow fields leads however to strong result variations (lower panel) making these parametrization approaches unfeasible.

We furthermore tested an approach described by D.T.Tambe *et al.* (Ref.[163]) by calculating the principle stress components of maximal ($\sigma_{\max}$) and minimal ($\sigma_{\min}$) stress with their corresponding orientations from the general stress tensor. However, neither calculating the average normal stress $\bar{\sigma}$ (equation 6.7 left), the maximum shear stress μ (equation 6.7 middle) nor the rotational part ϵ, also called the strain rate (equation 6.7 right and e.g. Fig. 6.11, lower panel), exhibited significant or relevant information.

$$[htbp]\bar{\sigma} = \frac{\sigma_{\max} + \sigma_{\min}}{2} \qquad \mu = \frac{\sigma_{\max} - \sigma_{\min}}{dt} \qquad \epsilon = (\frac{\partial v_y}{\partial x} - \frac{\partial v_x}{\partial y}) \tag{6.7}$$

Therefore we continued our parametrization search by developing a method to locally probe the optical flow. We used a definable grid of so called 'virtual beads' (Fig. 6.12, upper panel, right) that picked up the absolute local flow intensity and direction to follow the movement

of the underlying network structure. The beads picked up the local flow by using a local gaussian distribution function to calculate the overall local velocity and direction at the bead position. Interestingly, this 'virtual beads' method turned out to be a very efficient control if optical flow calculations of the network dynamics were correct. Furthermore, we could extract parameters such as 'virtual bead' displacement (Fig. 6.12, lower panel, left), spread area of the whole grid over time (Fig. 6.12, lower panel, middle) and global angular variance (Fig. 6.12, lower panel, right), a measure of shear calculated by equation 6.8. Here, φ_i refers to each inner angle of the small grid rectangles.

$$(\Delta\varphi)^2 \quad = \quad \frac{\sum_i(\varphi_i - 90°)^2}{N} \tag{6.8}$$

Similar to the highest intensity tracking, the displacement curves of single exemplary 'virtual bead' traces nicely depicted the stop-go motion again, even though the time scales were different compared to Fig. 6.2, The second parameter, the overall area covered by the grid, was in principle useful to describe surface contraction or dilatation over time (Fig. 6.12, lower panel, middle). However, the parameter was not a robust measure as we could produce differing outcomes depending on the initial placement of the grid using the upper left grid position (x_0/y_0) as the reference point. Moreover, comparing the area traces of different cells revealed diverse behaviors (Fig. 6.12, lower panel, middle inset).

The same difficulties of insufficient parameter robustness occurred for the global angular variance that measured shear of the initially rectangular grid. Varying grid position as well as cellular differences resulted in strong parameter variation (Fig. 6.12, lower panel, right and inset). Hence, the 'virtual bead' approach could not deliver as robust parameters as needed though it was a very simple yet effective way to test the correct flow field calculations.

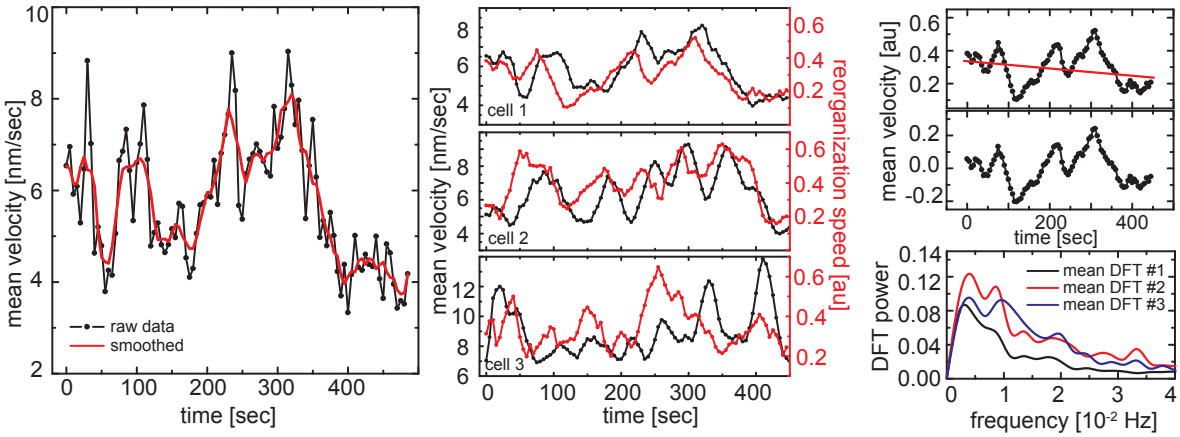

Figure 6.13: Mean optical flow velocity oscillates (left) and is very similar to reorganization speed oscillation (middle, red curves) thereby verifying occurence of oscillation and proper ITIC funcionality(middle). Analysis of mean velocity by discrete Fourier transformation (DFT) after subtraction of baseline (right, red line) for zero mode suppression does not lead to coherent results when comparing mean DFT curves (right, lower panel) of various control cell batches.

After testing various approaches to extract parameters without any success, we reflected back on the ITIC findings and continued our parameter finding by calculating the overall mean flow velocity per frame (Fig. 6.13, left). After Matlab based smoothing (robust local regression function 'rloess') of the calculated mean velocity the traces exhibited again an oscillatory character as for the ITIC curves. Indeed, comparison of optical flow based mean velocity traces and the corresponding ITIC based reorganization speed curves exhibited very similar behavior (Fig. 6.13, middle). Importantly, this finding evidenced that the newly developed ITIC method can be a very useful correlation based tool for finding global dynamic network characteristics within image sequences.

The oscillatory patterns of the mean velocity traces prompted us to more carefully investigate possible biological processes resulting in this myosin network pulsation. In a first approach to parametrize the oscillating traces we calculated the discrete Fourier transformation (DFT) of each trace to obtain a characteristic frequency range of oscillation. We first suppressed the zero mode of the Fourier transformation by subtracting an automatically fitted base line (Fig. 6.13, right panel, red line) from each trace. Subsequently, the DFT was calculated from the resulting trace oscillating around zero and the power spectra of all cell traces from one experimental batch were overlaid to find the resulting mean DFT power spectrum (Fig. 6.13, right,lower panel). However, we were not able to detect any distinct frequency domain from the resulting spectra. Since already different control cell batches from diverse experiments exhibited strong variation of DFT spectra and the overall maximal spectrum intensity was not significantly enhanced due to time-wise short traces with only few pulses we did not extend this analysis further. Here, only longer mean velocity traces would lead to better results which is however limited by the onset of photobleaching effects.

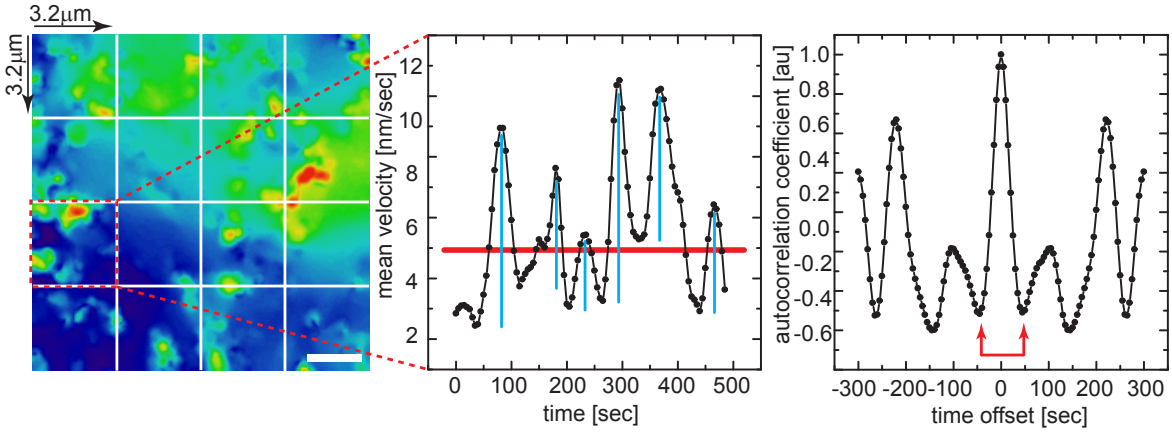

Figure 6.14: Final parametrization method of mean optical flow traces deduced from 50x50 pixel (3.2x3.2μm) sections of the absolute flow intensity sequences(left and middle). Traces were parametrized by overall mean velocity (middle, red line), activity potential (middle, blue lines) and oscillation period obtained from first two minima of autocorrelation curve (right, red arrows). Scale bar:2μm

As the DFT approach was limited by short mean velocity traces we set up another work flow to characterize the oscillatory traces. We started by segmenting the 200x200 pixel absolute

flow intensity movies into parts of 50x50 pixels (3.2x3.2μm) (Fig. 6.14, left). Note here that we chose these dimensions as we had calculated the characteristic spatial correlation length scale to 3μm (chapter 4.6). For each segment we calculated the mean flow velocity over time and subsequently characterized the traces using the following three parameters:

1. **overall mean velocity:** the overall mean of the flow velocity distribution to characterize overall movement (Fig. 6.14, middle, red line)
2. **activity potential:** the difference between a pulse maximum and its preceding minimum to characterize the myosin activity potential (Fig. 6.14, middle, blue lines)
3. **oscillation period:** the time between the first two minima of the mean velocity autocorrelation curve to characterize a frequency of oscillation (Fig. 6.14, right, red arrows)

To obtain the third parameter of oscillation period we autocorrelated the mean velocity trace with itself. Due to oscillatory signal trace the autocorrelation function (Fig. 6.14, right) of this signal oscillates accordingly and the period between the first two function minima calculated from the reference point of zero time shift directly reflect the oscillation period time.

This definition of three parameters for characterizing the oscillatory myosin network behavior turned out to be a good set for further investigations on the possible underlying biological or physical mechanisms leading to oscillatory behavior. We therefore continued our apical myosin network analysis by large scale experimental runs using various drugs or different cell lines to shed light on possible underlying mechanisms causing the oscillations. These results will be presented in the following chapter.

6.5 Discussion

In this chapter we have described various newly developed or adapted image analysis methods used in the course of this thesis to characterize the dynamical features of the identified novel cortical myosin network. While the first approach of highest intensity tracking only returned basic and insufficient data regarding dynamics characterization our newly developed method of incremental temporal image correlation (ITIC) revealed astonishing new insights. By plotting the characteristic decay constants for each frame over time we deduced an oscillatory pattern changing between times of slow and fast network reorganization (Fig. 6.3 and 6.4). Hence, the cortical myosin network exhibits a dynamical mechanism of oscillatory reorganization that is presumingly very similar to various published results from different biological research fields including results from the developmental field on apical constriction during *Drosophila melanogaster* morphogenesis (Ref.[133],[105],[104]), cell biological research on single non-adhering fibroblast undergoing shape oscillations (Ref.[144],[143]), or *in vitro* approaches using minimal actomyosin cytoskeleton mimicking assays (Ref.[81]). In all these experiments the interplay of myosin motors and actin filament caused oscillations leading in some cases to cell shape remodeling.

Various theories regarding the origin and need of oscillatory actomyosin behavior have been discussed with respect to experimental data of cellular behavior. While some theories focus on the protein based regulatory machinery underlying this oscillations (Ref.[132],[105]) other theories describing actomyosin driven oscillatory behavior are based on e.g. Ca^{2+}

or ATP pulsation (Ref.[144],[86],[74]), non uniform cortical tension (Ref.[87]) or intrinsic properties of the myosin motors such as binding affinity or load dependent mechanisms (Ref.[81],[16],[111],[101]). In the previous chapters we already presented data revealing (1) the existence of cortical tension (Fig. 4.13), (2) the dependency of dynamics on myosin activity (Fig. 4.11) as well as (3) long scale and long time oscillatory cortical rearrangements upon unbalancing the myosin network tension using drugs (Fig. 4.12). Hence, we presume a combination of these three effects to cause the observed oscillatory network reorganization. We furthermore tested a possible dependency of the oscillation on calcium influx as proposed by Salbreux or Westphale *et al.* (Ref.[144],[176]). However, using various approaches including switching to calcium free medium (HBSS(-), EpiLife), chelating extracellular calcium (EGTA, EDTA), blocking cellular calcium pumps by using gadolinium ions Gd3+ (Ref.[6]) or increasing calcium influx by small ionomycin concentration treatment (Ref.[121]) did not result in detectable changes of oscillatory behavior. Due to the invariant results we therefore do not present these data within this thesis. Nevertheless by performing these experiments we can now rule out a strong oscillation dependency on extracellular calcium levels.

Apart from discussing possible oscillation driving cellular regulators that will be discussed more detailed within the subsequent chapter we here presented one further image analysis approach, namely the optical flow analysis. As the ITIC method has the disadvantage to not return any detailed information on a sub-cellular level but rather describes global dynamical changes we applied an adapted version of a program accessible at the MatlabCentral server (FileID: 17500) previously used in the field of motion rendering for 2D or 3D computer animations. This third approach, in principle based on the famous 'gray value constancy assumption' formulated by Horn and Schunck (Ref.[61]), enabled us to gather detailed and novel information of sub-cellular dynamic differences. We can show that sub-cellular regions reorganize with different velocities leading to shear and stress within the cell cortex. Stress and strain within epithelial cell sheet layer have already been implied to act as cell guiding mechanisms for tissue migration during wound healing (Ref.[163]). That stress and strain is as well present in the cell cortex at sub-cellular level is to our knowledge not yet described. Moreover, we have first very preliminary indications (data not shown) that this sub-cellular differences of cortical myosin network reorganization regulates at least partially the plasma membrane organization (Ref.[79]). By restricting or enhancing lateral motion within certain cortical regions the distribution of membrane proteins could be affected either by direct transport (Ref.[8]) or by diffusion barrier and fencing effects (Ref.[139]). However, to answer the question of membrane organization a broad range of specific experiments has to be performed during future investigations to identify if plasma membrane associated proteins are directly affected in distribution and dynamics by the underlying myosin network motion.

As we were not able to standardize the cell state to perform comparable experiments by e.g. placing cells on specific substrate patterns (Fig. 4.7) we were forced to find parameters characterizing myosin network dynamics irrespective of cell behavior variances. By using three parameters (1) mean overall velocity, (2) activity potential and (3) oscillation period (chapter 6.4.3) we can now on one hand confirm the correct ITIC method based finding of oscillatory network behavior even though the ITIC over-samples. On the other hand we are now able to set up a complete range of experiments that allow for data comparison by analyzing all data using the same optical flow analysis pipeline. These biological experiments will be described in the subsequent chapter.

Chapter 7

Insights into myosin network regulation by optical flow analysis

7.1 Introduction

A key question during this thesis arose when we performed the ITIC analysis thereby finding the oscillatory behavior of reorganization speed. Is there a cellular regulatory machinery driving this oscillation in myosin activity or is this characteristic due to local force instabilities of a tensile isotropic network?

We already discussed in the previous chapter 6.5 that various mechanisms have been reported to cause oscillatory behavior within cells or even tissue. One mechanism that we assumed to act as a very likely oscillation driving factor was calcium ion variation. It has been reported several times that cytosolic calcium oscillates or pulsates in MDCK cells (Ref.[178],[179],[26]) due to e.g. Ca^{2+}-influx. As myosin activity is dependent on calcium (Fig. 7.3) we tested in various different experiments how myosin network oscillation changes upon extracellular calcium removal (chapter 6.5). However, extracellular calcium does not seem to be the direct underlying driving mechanism. Hence we here turn towards innercellular myosin regulation mechanisms.

Non-muscle myosin proteins are a key component of the cytoskeleton of epithelial cells. Hence the protein is highly regulated by various different activating or deactivating signal pathways (Ref.[22],[106]). For example, DeBlasio *et al.* (Ref.[26]) reported that innercellular Ca^{2+} signaling coherently changes the adhesion properties of MDCK cells. Other reports demonstrate RhoA mediated and calcium independent periodical cortical contractions occuring in spreading cells (Ref.[23]). Furthermore, anisotropic E-cadherin distribution has been shown to cause pulsatile actomyosin dependent contractions in *Drosophila melanogaster* tissue during embryonic germband extension (Ref.[132]). From the theoretical physics perspective, oscillatory motion of molecular motors can as well already occur by cooperative effects without any additional underlying regulation (Ref.[72]). This broad variation of regulatory cascades or cooperative effects causing oscillatory cell behavior nicely depicts the necessity to probe various cellular signaling pathways to get a glimpse on possible underlying mechanisms. Once the oscillation driving factor is deduced it should be fairly easy to conclude on the cellular function of the apical myosin network.

Here we describe our screen of experiments all performed identically to identify possible regulators of myosin that influence the network oscillation. We first show that all identified

cell lines with a cortical network (Fig. 4.4) oscillate on different time scales and with different reorganization speeds. We continue our screen by monitoring the effect of the scattering factor HGF on the myosin network oscillation revealing that the oscillation increases upon 24 hour HGF treatment. As it is known that HGF does not specifically target one protein signaling pathway but interferes with a broad range of cascades we subsequently test specific regulators of myosin. While some show interference effects either by drug treatment or by additional regulator protein expression other regulators do not seem to influence the oscillation and reorganization speed of the network. We conclude that RhoA is presumingly the candidate which should be more carefully investigated in future experiments to clarify its distinct role in cortical network regulation.

7.2 Model cell lines exhibit different dynamics and frequencies

We started our biophysical characterization of network behavior by measuring the three parameters (1) mean velocity, (2) activity potential and (3) oscillation period (chapter 6.4.3) for the various model cell lines. As already presented (Fig. 4.4) we identified the isotropic apical myosin network not only in MDCK cells but also in carcinoma cell lines (HeLa, PancI, MCF7) as well as in osteosarcoma cells (U20S) and in fibroblast-like (COS) or fibroblast cell lines (NIH-3T3). All networks dynamically reorganized though on different time scales. Using our optimized optical flow analysis (Fig. 6.14) we deduced distinct changes in all three parameters for the different cell lines (Fig. 7.1). Note here, that all following results are plotted using box plots with characteristics: (1) large box defining 25th to 75th quartile, (2) horizontal line in box defining median, (3) small box defining mean value, (4) whiskers defining outliers with intra-quartile range coefficient of 1.5.

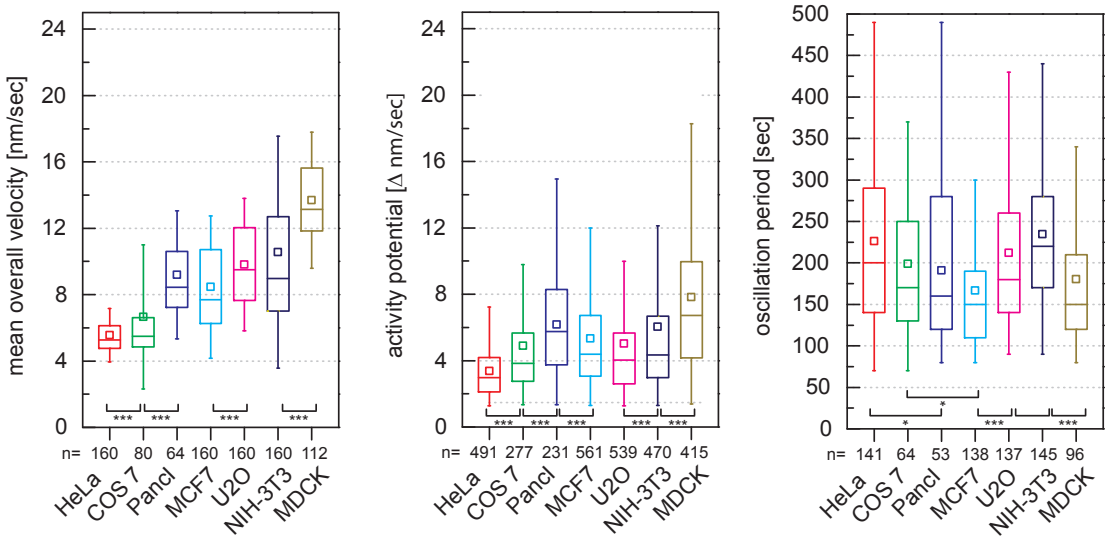

Figure 7.1: Optical flow analysis screen of various model cell lines reveals differences in all three parameters, mean overall velocity (left), activity potential (middle), and oscillation period (right).Importantly all cell lines exhibit dynamic reorganization.

Interestingly, we revealed a threefold increase in mean velocity when comparing the quasi-static HeLa dynamics (≈ 5nm/seconds) to MDCK cells (≈ 14nm/seconds). The other model cell lines tested in course of this study span the complete velocity range between slow HeLa and fast MDCK dynamics (Fig. 7.1, left). Activity potential, defining the difference between minimum and subsequent maximum velocity peak (Fig. 6.14), did not directly correlate with mean velocity (Fig. 7.1, middle). Rather than following the cell line specific steady increase of mean velocity the activity potential changed significantly and independent of slow or high mean velocities. Hence, the networks ability to change between states of slow and high reorganization dynamics was influenced by other factors than the overall network reorganization speed. Moreover, the oscillation period of different model cell lines exhibited interesting features as well (Fig.7.1, right). While HeLa as the slowest reorganizing cell line only oscillated on a time scale above 220 seconds MCF7 and MDCK cells changed more frequently between states of slow and high velocities on time scales around 150 seconds. We hypothesized from these differences in network oscillation period times that an underlying biological process possibly drives this oscillation in reorganization. Therefore, we set out to find this pacemaker by various experimental approaches discussed in the next section.

7.3 Experimental variation for characterizing parameters

As a first step to deduce the underlying cellular process of apical network dynamics and oscillation we had to define which model cell line we use for the experiments. As we had already established stable cell lines of MDCK and this cell line was moreover highly dynamic and oscillatory (Fig. 7.1) we continued our experiments with these standard ECs.

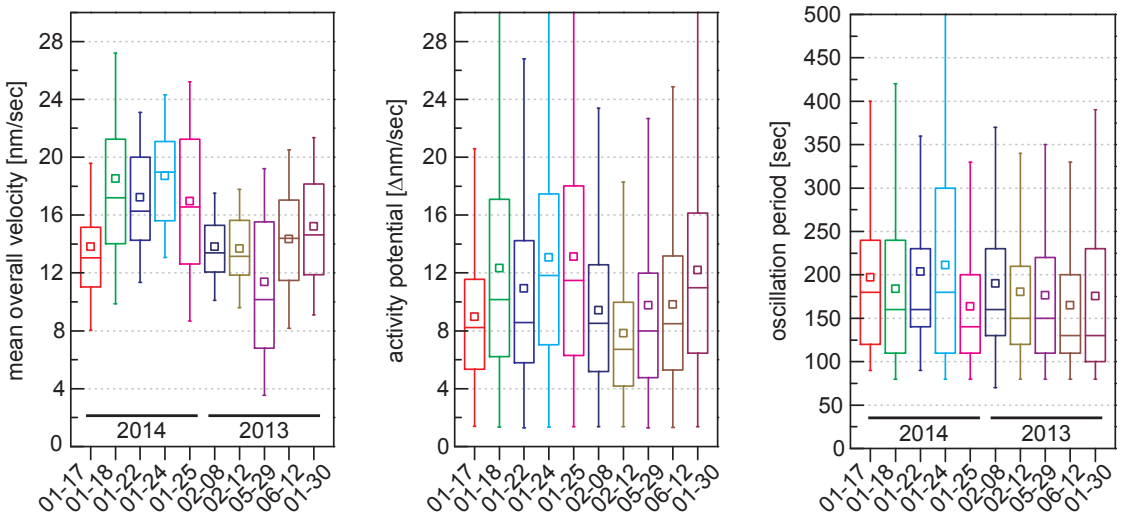

Figure 7.2: Parameter variation comparing sets of control experiments of MDCK cells from different days and different cell culture sessions.

Next we had to investigate on the daily or cell batch variations for the experimental routine. We therefore compared the controls of various experiments at different days and years to

get a glimpse on the time dependent parameter variation. To our surprise the variation of outcome was of significant order (Fig. 7.2). Mean velocities varied between 12-19 nm/second and activity potential had a similar range of about 5nm/second difference between varying control experiments. Logically, the oscillation period parameter changed as well significantly between different experiments. However, the resulting mean oscillation period was with one exception always below 200 seconds. Hence, the difference in oscillation period for different cell lines was not only an artifact of parameter variation but instead a distinct and significant change related to different cellular behavior (Fig. 7.1). As a final conclusion, we adapted our experimental routine the way that we always performed control experiments alongside to directly compare the parameter variation for each experimental run. Moreover, we repeated most experiments several times to assure that the measured effect was not an artifact of image analysis or cellular variation. The number of independent experimental runs will be marked for each approach.

7.4 HGF decreases oscillation period

Judging from effects described in chapter 3.2.5 of HGF on the structure and dynamics of the apical actin (Fig. 3.14) as well as from the already known effect of HGF to induce cell migration (Ref.[136]) we first tested for possible dynamical changes of the myosin network upon HGF stimulation. We incubated cells for 24 hours with 200 ng/ml HGF and compared the dynamics to a simultaneously growing untreated set of cells. This experiment was repeated independently for three times.

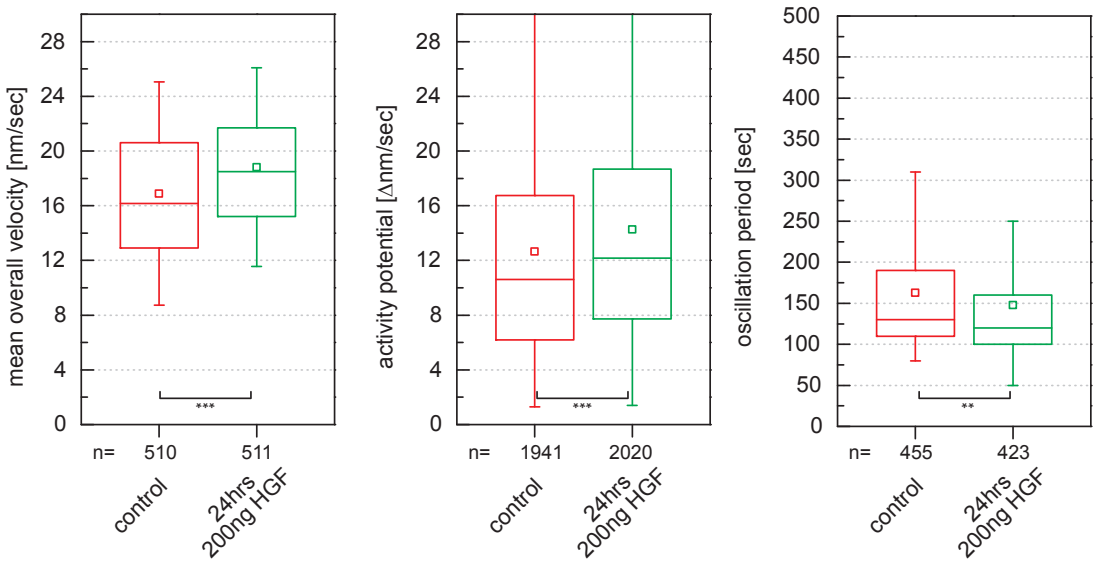

Figure 7.3: HGF increases reorganization speed (left) as well as activity potential (middle) and interestingly decreases oscillation period (right) to below 150 seconds. n-values for overall number of analyzed and recorded trace parameter.

As expected, the mean velocity for HGF treated cells increases slightly but significantly (Fig. 7.3, left). In close accordance to the known HGF induced increase of cell motility (Ref.[159],[15]) this increase in mean network velocity might result from necessary cellular adaptations to fast cell shape remodeling. Along this line, the finding of increased activity potential for HGF treated cells was an additional hint towards increased cellular apical myosin network activity (Fig. 7.3, middle). Most importantly though, the HGF treatment resulted in an oscillation period decrease, meaning that the time between states of slow and fast reorganization decreased (Fig. 7.3, right). The scatter factor HGF is known to activate the guanosine-triphosphate (GTP) binding protein Ras (Ref.[44]), a known signal transduction protein including signaling to the cytoskeleton ([47]). In addition, HGF induces a broad spectrum of biological activities in epithelial cells including mitogenesis or promotion of matrix invasion (Ref.[44]). Hence, in the context of finding a biological pacemaker, we interpreted this change of oscillation period upon HGF treatment as a strong indication for a presumably underlying myosin activity regulator that controls and drives the oscillation. We therefore continued experiments by focussing on the various cellular myosin activity regulators.

7.5 Myosin regulatory machinery

To interfere with specific myosin motor regulating proteins we first had to identify the regulatory key players involved in the activation and deactivation of the myosin motor. In the last decades of cytoskeleton research strong focus has been put on the understanding of the cellular regulatory machinery controlling cytoskeletal processes. These efforts resulted in the discovery of a broad range of regulatory proteins. In detail, for myosin motors only more than seven regulators have been implicated to directly activate or inactivate myosin (Ref.[106],[21]). For our purposes the identification of the key regulators, which we will denote here briefly, was sufficient for a first approach.

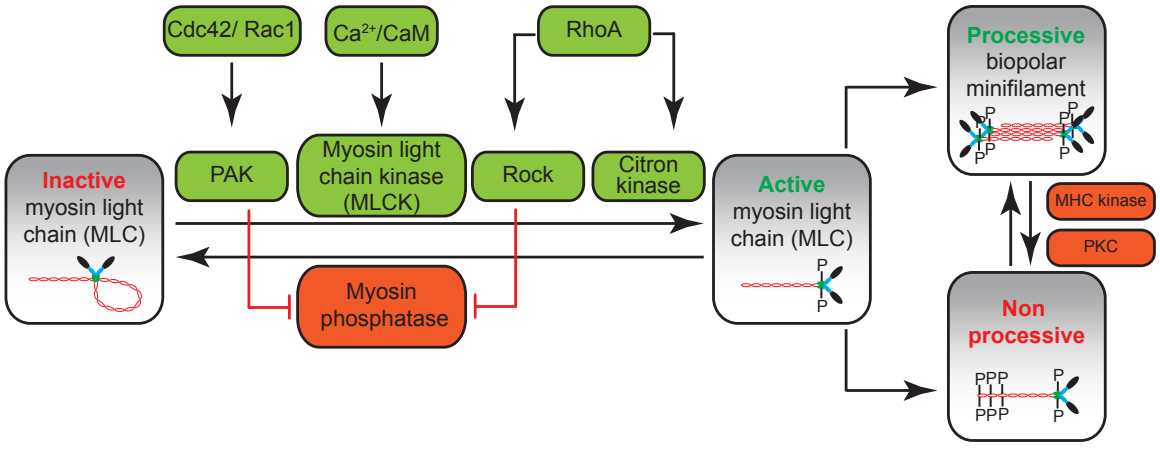

Figure 7.4: Scheme of myosin light chain key regulatory machinery with activating regulators (green) switching MLC from inactive to active by phosphorylation and deactivating regulators (red).

As already depicted in Fig. 4.1 myosin has a phosphorylation dependent inactive and active state. Whenever the myosin regulatory light chains (MLC) are phosphorylated, myosin decoils from its inactive state to the so called active state. In a second step, several active but unipolar myosin units can now assemble to a processive bipolar minifilament by attaching the myosin heavy chain (MHC) tail domains. As minifilaments the myosins are then the fundamental units for contractile force generation in nonmuscle cells (Ref.[92]). MHC kinases or the protein kinase C (PKC) are able to phosphorylate the heavy chain tail domain of single active myosin units or of minifilament subunits leading to the inactivation of myosin minifilaments (Fig. 7.4, right). However, the crucial step for assembling an actomyosin complex and initiating contraction is the phosphorylation and dephosphorylation of MLC (Ref.[106]). Here, several key regulatory players control the myosin conformational state. Shifting myosin from its inactive to active state is mainly regulated by myosin light chain kinase (MLCK) as well as by p21-activated kinase (PAK), Rho kinase (Rock) and citron kinase (Fig. 7.4, green boxes). The shifting from active to inactive state is mainly driven by the myosin phosphatase (Fig. 7.4, red box). Additional upstream regulators of the activators include Rac1, Calmodulin (CaM), calcium level (Ca^{2+}) and the RhoA protein, which is, as Rac1, a family member of the Rho GTPases (Ref.[106],[137]). In addition, the regulators themselves interfere with each other either by complementary inhibition or activation (Ref.[52]). In conclusion, the myosin light chain regulators form a very complex network of dependencies to tightly control the crucial step of contractility activation or deactivation.

7.6 Blocking MLCK activity blocks myosin dynamics

In the subsequent experiments we tested effects on myosin network dynamics while interfering with one specific regulator for each experimental run. We started our investigation by using the MLCK blocking drug ML7 (Ref.[174]) (Fig. 7.5, scheme). We already reported in chapter 4.9 that myosin network dynamics could be blocked using this drug (Fig. 4.11). With the help of our optical flow image analysis we could now verify this finding. This experiment was repeated independently for three times.

As expected the mean velocity significantly decreased after 15 minutes of 30μM ML7 incubation (Fig. 7.5, left). Moreover, the activity potential drastically dropped from a mean of 12 nm/seconds difference between minimum and maximum velocity to 8 nm/seconds difference (Fig. 7.5, middle). In contrast, the oscillation period increased from the mean value of 170 seconds in control cells to about 220 seconds period time after ML7 treatment. Hence, MLCK activity directly correlated with the networks ability to reorganize efficiently. Inhibiting the active state of myosin led to less powerful pulses of reorganization (decreased activity potential) and longer times between states of slow and fast reorganization (Fig. 7.5, right).

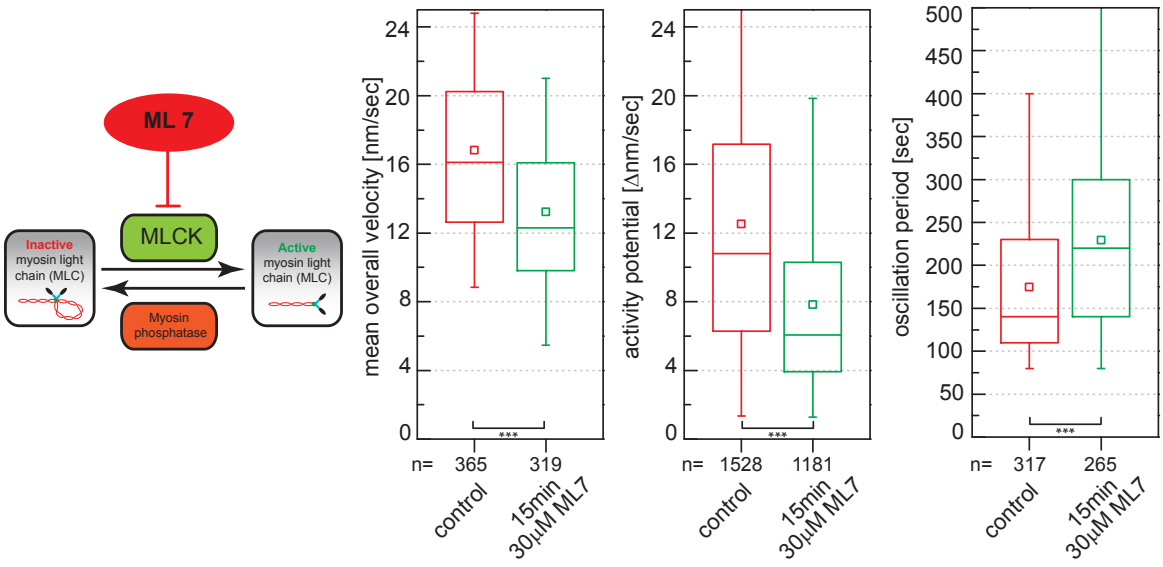

Figure 7.5: Blocking MLCK by ML7 drug significantly decreased mean overall velocity (left) and activity potential (middle) while shifting oscillation periodity to higher values (right). n-values for overall number of analyzed and recorded trace parameters.

7.7 Upstream MLCK regulators interfere with myosin dynamics

To further confirm the direct connection between MLCK activity and myosin dynamics we continued along this line by interfering with the upstream regulators of MLCK, namely the dependency on innercellular calcium ion level (Ca^{2+}) (Fig. 7.4). Treating cells for up to 20 minutes with 30μM Bapta-AM, a calcium chelator that binds intracellular calcium (e.g. Ref.[121]), should result in an inhibitory effect on MLCK and thereby on the activity of myosin (Fig. 7.6, scheme).

Indeed, performing this experiment twice, we monitored a decrease in mean velocity over time (Fig. 7.6, left). Similar to the direct blocking of MLCK, the activity potential decreased significantly as well upon intracellular Ca^{2+}-level reduction. Interestingly, the oscillation period first increased to above 200 seconds after 10 minutes of Bapta-AM incubation as for ML7 (Fig. 7.6, right). However, after 20 minutes of drug treatment the oscillation period recovered to the level of the control cell time scale. Hence, the cells presumingly counterbalanced the intracellular Ca^{2+} decrease either by releasing calcium from the cellular storages leading to saturation of the chelator molecules or by up-regulating other myosin regulators that are as well Ca^{2+} sensitive (Ref.[156])

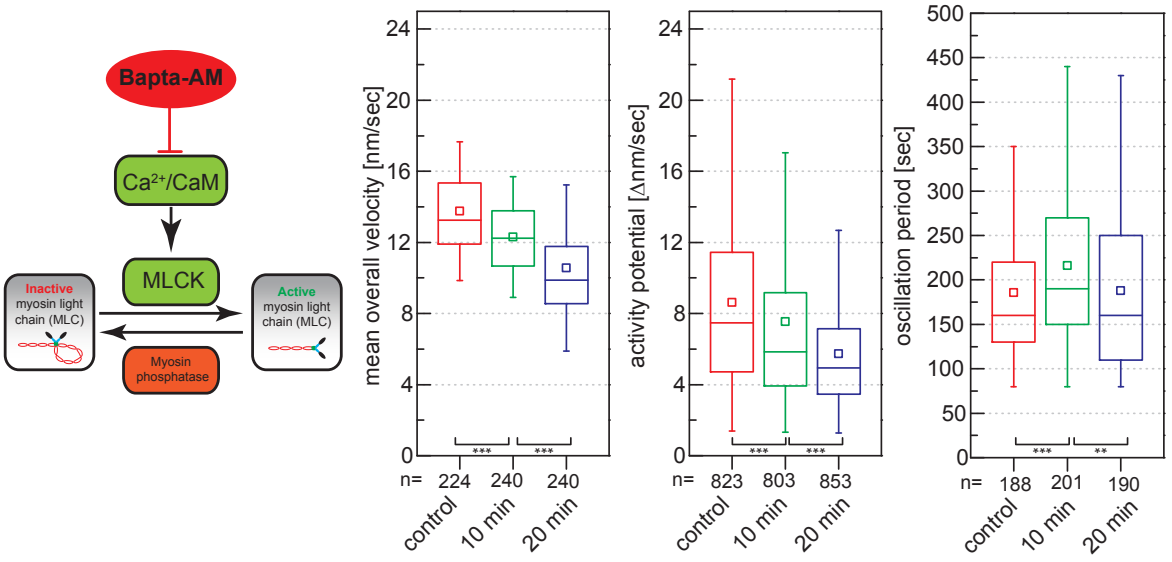

Figure 7.6: Treatment with 30μM Bapta-AM results in decreased mean overall velocity (left) and activity potential (middle) as for MLCK blocking. Oscillation period shows short interference effect of reduced intracellular calcium that is counterbalanced after 20min (right).

As already mentioned intracellular calcium level is a crucial aspect for correct cellular function as calcium is a fundamental signaling component and therefore under tight cellular control. To not only monitor the effect of intracellular calcium level decrease by using Bapta-AM we subsequently used the drug Bradykinin which triggers calcium influx. As this ion influx occurred instantaneously upon drug addition we monitored myosin network dynamics directly after Bradykinin was added to the cells as well as at a later time point of 10 minutes drug incubation (Fig. 7.7). This experiment was repeated independently for three times.

In contrast to our assumption, the intracellular calcium level increase induced only medium effects on the network dynamics. Mean velocity changed only slightly to faster dynamics after 10 minutes of incubation (Fig. 7.7, left). The activity potential decreased immediately upon Ca^{2+} influx and returned to control level after ten minutes of incubation. Moreover, the oscillation period significantly increased directly after drug addition rather than decreasing with increasing intracellular calcium level. This experimental result therefore contradicted our postulation that an increase in calcium leads to increase in MLCK thereby directly resulting in more activated MLC units (Fig. 7.7, scheme). Why this calcium influx did not result in significantly enhanced myosin network dynamics remains to be elucidated. It is known that cells adapt fast to an increase in intracellular calcium by quickly pumping the additional free ions to the cellular storages (Ref.[156]). Moreover, a bradykinin stimulus has been shown to result in intracellular calcium level oscillation after about ten minutes (Ref.[26]). If this calcium oscillation interferes with the myosin network dynamics is one key experiment for future investigations.

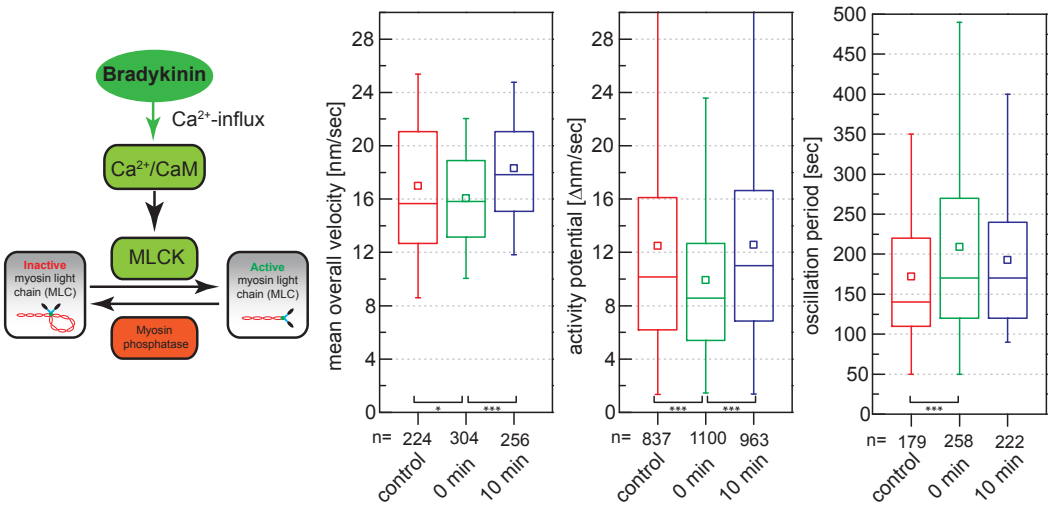

Figure 7.7: Only medium effects on reorganization dynamics after Ca^{2+} influx are observable with slight mean overall velocity increase after 10min of treatment (left) and oscillation period increase immediate to Ca^{2+} influx (right). Activity potential exhibits short term effects but recovers after 10 minutes (middle).

7.8 RhoA dependent changes in network dynamics

Apart from the MLCK dependency we further tested the effects of the myosin activator protein Rock and its upstream regulator RhoA (Fig. 7.4). Rock activity can be directly blocked by using the inhibitor drug Y27632 (Ref.[25]). We incubated cells for 30 minutes with 40μM of Y27632 and subsequently compared the myosin network dynamics to control cell dynamics. This experiment was performed once only.

Important to note here was the overall effect of Y27632 treatment on the network structure. After 30 minutes of incubation most cells showed no signs of a remaining apical myosin network (data not shown). In contrast, these cells exhibited high cytosolic fluorescence signals presumably related to disassembled myosin within the cell. We could only find very few cells with an intact apical myosin network. Monitoring the dynamic behavior of these cells led to the finding that Rock inhibition did not result in characteristic dynamical network changes (Fig. 7.8). All three parameters, mean velocity, activity potential and oscillation period, were comparable to the control set of cells. Hence, Rock is responsible to maintain the apical myosin network structure but is not directly related to drive the dynamics of the network. However, more experiments need to be executed to verify this statement.

As another approach than drug related inhibition or activation we continued our investigation by transfecting MDCK cells with plasmid constructs containing the sequence for expression of RhoA protein (Fig. 7.9, schematic). By single point mutations in the gene sequence the expressed protein can be turned into a constitutively active (mutation Q63L) or dominant negative (mutation T19N) state as described in Ref.[161]. We transfected our cells with the wildtype, constitutively active and dominant negative RhoA coding plasmid respectively and incubated cells for 24 hours. Subsequently we monitored possible changes in network

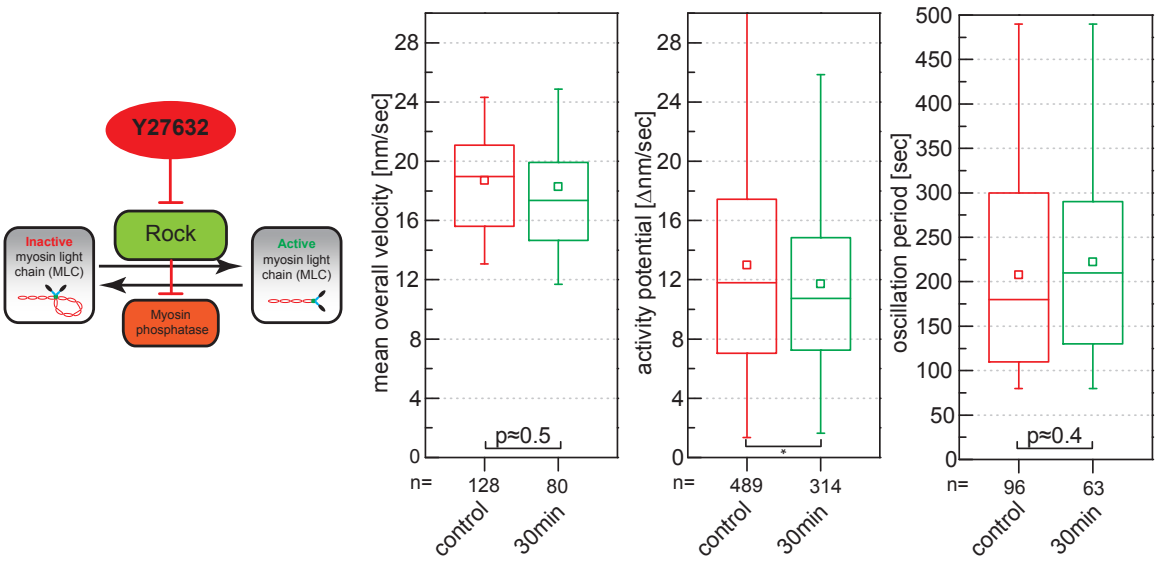

Figure 7.8: Blocking Rock activity by Y27632 drug causes no dynamic changes though most of the cells incubated for 30min with 40μM Y27632 have disassembled myosin networks(data not shown).

dynamics. Note here however, that the experiments were performed without knocking out the endogeneous background level of RhoA first which is necessary to achieve full mutation interference. Therefore these experiments, performed independently twice, can only roughly mimic possible effects on the dynamics.

While there were only slight to no effects detectable regarding changes of oscillation period (Fig. 7.9, right) the mean velocity and activity potential of cells additionally expressing constitutively active RhoA were significantly increased (Fig. 7.9, left and middle). In contrast, additional incorporation of dominant negative RhoA did not lead to dynamic variation in comparison to additional wildtype RhoA expression. This similar behavior might be due to the above mentioned underlying endogeneous level of RhoA expression as we did not knock down the gene expression level. Nevertheless, the increase in mean velocity and activity potential and the small decrease in oscillation period for cells expressing constitutively active RhoA could be interpreted such as RhoA directly influences the dynamical properties of the apical myosin network while Rock is responsible for the network maintenance. The known effect, that RhoA promotes cell contraction and stress fiber assembly (Ref.[146],[168]) might in this context account as a confirmation that the contractile apical myosin network is under RhoA control.

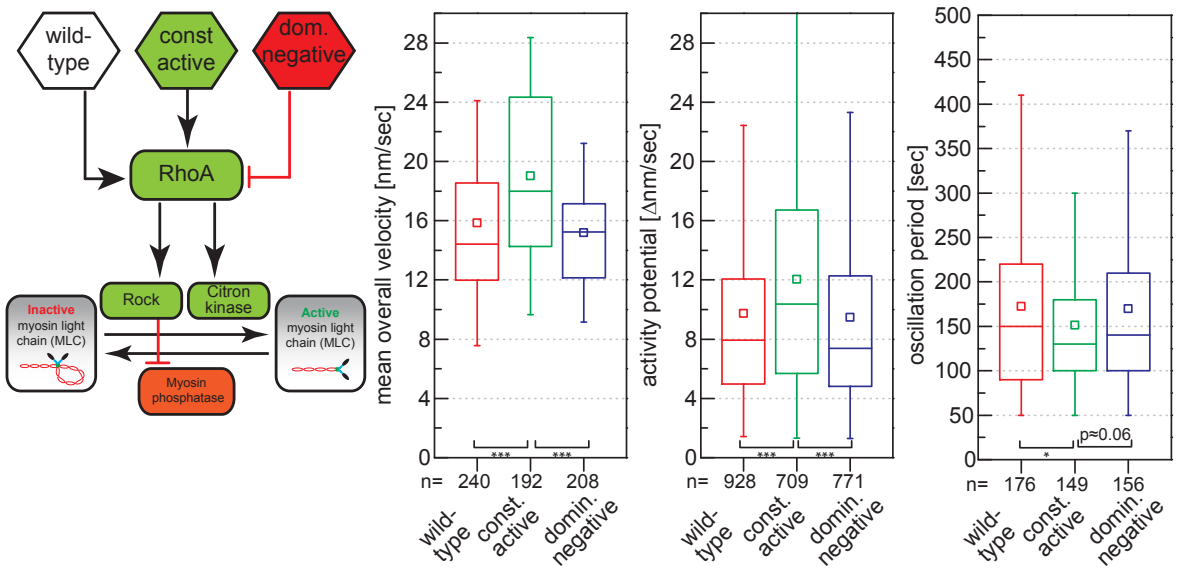

Figure 7.9: Additional constitutive active RhoA expression leads to increased reorganization speed (left), activity potential (middle) and has mild to no effects on oscillation period (right) while dominant negative expression is comparable to additional wildtype expression.

7.9 Rac1 dependent changes in network dynamics

Rac1 is another important member of the Rho GTPase family functioning as a counterpart to RhoA and being involved in myosin activity regulation (Fig. 7.4). Increasing activity of Rac1 or RhoA complementary downregulates the others GTPase activity respectively (Ref.[146],[184]). As a logical step we therefore repeated the experiments presented in the previous section though now using wildtype, constitutively active and dominant negative Rac1 plasmid constructs as described in Ref.[60]. The experiments were performed independently for two times.

Constitutively active RhoA induced an increase in mean velocity and activity potential (Fig. 7.9). It was hence unsurprising to obtain inverted results for the RhoA counterpart Rac1. Constitutively active Rac1 led to a significant decrease in mean velocity as well as in activity potential (Fig. 7.10, left and middle). Similar to the RhoA experiments, no interferences of additional Rac1 expression with network oscillation period was observable (Fig. 7.10, right). In contrast to the RhoA experiments however, the dominant negative Rac1 construct had the same effects on the network dynamics as the constitutively active construct as mean velocity and activity potential decreased. Why the dominant negative Rac1 construct induced such effects rather than showing no changes compared to wildtype constructs, as for RhoA (Fig. 7.9) could not be clarified. Again, more precise experiments using Rac1 knocked-out cells without an endogeneous background expression of Rac1 would presumably lead to more reliable data. These experiments should be of high interest for future characterization of the apical myosin network dynamics. In conclusion, we could establish with these plasmid construct based approaches that RhoA seemed to be the dynamic driving regulator keeping

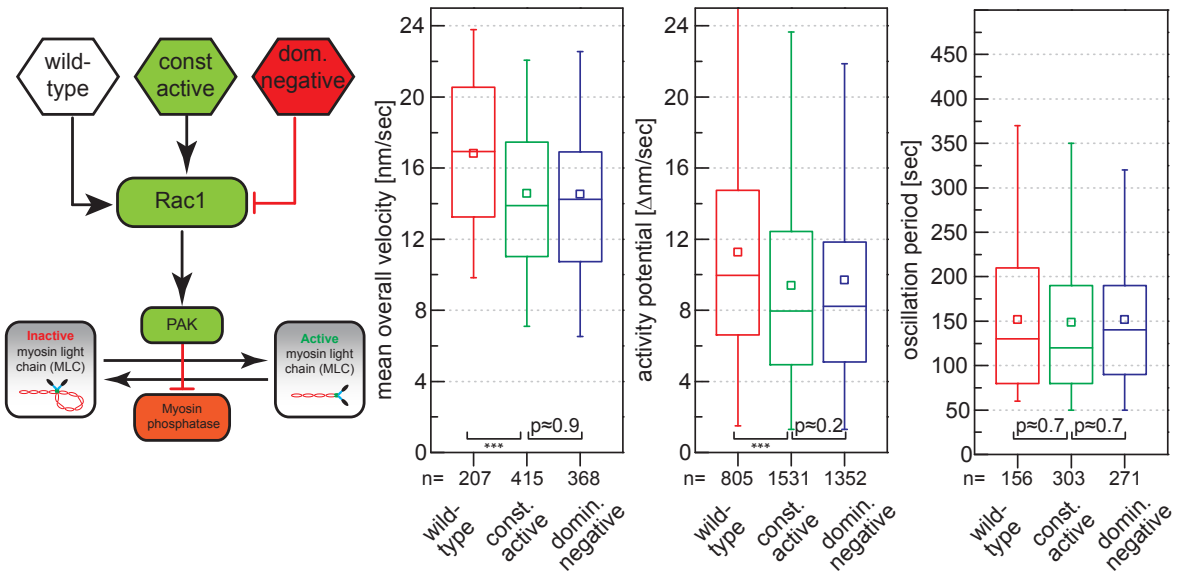

Figure 7.10: Additional constitutively active Rac1 expression leads to decreased reorganization speed (left), activity potential (middle) and has no effects on oscillation period (right). Different to RhoA dominant negative construct, the dominant negative Rac1 construct exhibits comparable effects on myosin dynamics as constitutive active construct expression.

up motion as well as the network structure itself. Its counterpart Rac1 counteracted this dynamic enhancing effect by inhibiting motion and thereby keeping the system in a tightly regulated and stable range of dynamics.

7.10 Myosin hyper-activation does not change network behavior

Until this point we only focussed on interfering with myosin motor regulating proteins that activate myosin units by facilitating or triggering phosphorylation of the regulatory light chain (Fig. 7.4). However, in another experimental approach we focussed on the myosin phosphatase protein, that inactivates myosin by a dephosphorylation step (Ref.[174]). We used small amounts of a drug called Calyculin A that blocks various phosphatase activities (Ref.[59]) Experiments with different Calyculin A concentrations were performed once each.

We titrated various amounts of Calyculin A to cells to identify the concentration range of intermediate effects. Relatively high concentrations of Calyculin A above 50nM eventually led to a fast detachment of the cell from the substrate due to focal adhesion rupture caused by the simultaneous pulling of hyper-activated motor proteins upon drug treatment (data not shown). Therefore we tested 10nM and 20nM Calyculin A concentration. However, we could not identify any significant change in the network dynamic parameters neither in mean velocity, activity potential nor in oscillation period (Fig. 7.11). If the optimal concentration window to interfere with the dynamical properties of the myosin network was just very narrow

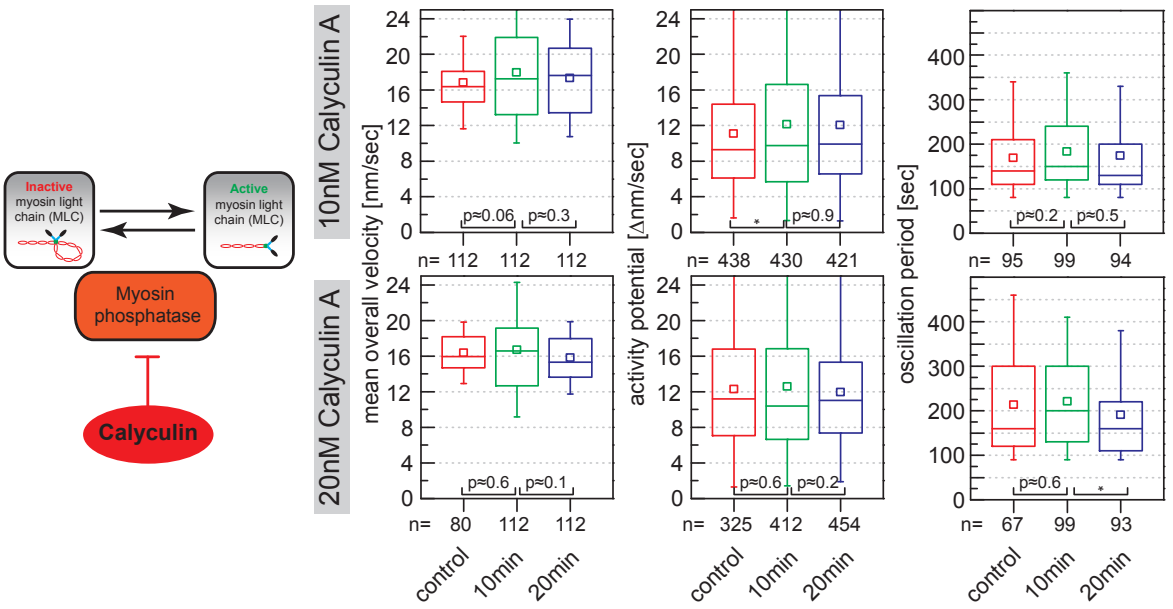

Figure 7.11: Hyper-activation of myosin by either 10nM (upper) or 20nM (lower panel) Calyculin A does not lead to significant changes in network reorganization dynamics.

when using Calyculin A or if the network dynamics were rather robust against myosin activity increase until a threshold level we could not clarify to this point. Here, more experiments with the complete titration range of Calyculin A concentrations would lead to more insights related to myosin hyper-activation.

7.11 Discussion

This chapter concentrated on finding possible myosin regulatory proteins that control the dynamical behavior of the identified apical network structure. We started our approach by screening various model cell lines exhibiting the network structure. By applying our in chapter 6 developed optical flow analysis we were able to characterize differences in dynamics, namely in reorganization speed, myosin activity potential and oscillation period changes between different cell lines (Fig. 7.1). Hence we can conclude two statements from this screen: (1) all cell lines with an apical network structure dynamically reorganize the apical myosin network and (2) these dynamical reorganization patterns occur on different time scales. Importantly, the oscillation periods between slow and fast network reorganization changes significantly when comparing e.g. HeLa cells ($\approx$ 225 seconds) and MCF7 or MDCK cells ($\approx$ 150 seconds). Concluding from these findings the myosin network with the characteristic oscillation is a general hallmark of adhering cells from various physiological backgrounds but with epithelial morphology.

Apart from the important finding of a general apical myosin network structure occurrence with similar dynamical features we were able to identify two regulating pathways interfering

with the isotropic cortical network behavior. First, we can show the direct link between MLCK and myosin network activity by either blocking MLCK directly (Fig. 7.5) or indirectly influencing the network behavior by chelating cytosolic Ca^{2+} (Fig. 7.6). We were even able to slightly increase the myosin reorganization speed by inducing calcium ion influx using the drug bradykinin (Fig. 7.7). However, upon influx of Ca^{2+} the oscillation period slowed down indicating that activated myosin does not necessarily result in faster reorganization pulses. Thus cytosolic calcium levels indirectly influence the network dynamics via MLCK activity. However, we have so far not succeeded in monitoring cytosolic calcium level changes that could drive myosin network oscillations as postulated by Veklser *et al.* (Ref.[169]). Precise measurement of cytosolic ion pulses and subsequent cross-correlation to the dynamical patterns of the cortical network should be performed to substantiate this hypothesis.

Second, we identified Rock and RhoA to be regulating the maintenance and increasing the dynamics of the isotropic cortical network respectively. While blocking Rock kinase does not interfere with the dynamics of the network though leading to the disassembly of the myosin structure (Fig. 7.8 and chapter 7.8), additional expression of constitutively active RhoA protein leads to increased myosin dynamics and a slight decrease of the oscillation period (Fig. 7.9). RhoA as a member of the Rho GTPase family has been implicated to regulate cell body contractility while its counterpart Rac1 promotes membrane protrusion (Ref.[131],[14]). Both, Rac1 and RhoA control actin and adhesion dynamics thereby controlling cell migration (Ref.[123],[99]). Hence our finding of increased myosin network activity upon enhanced and constitutively active RhoA expression (Fig. 7.8) point towards a possible function of the network structure for cell migratory purposes. Along this line the disappearance of the cortical network in confluent cells (Fig. 4.2) is an additional hint towards this cellular function. It has furthermore been reported that Rac1 expression antagonizes RhoA activity (Ref.[116],[146]) which is in good accordance with our finding of reduced network dynamics upon enhanced and constitutively active Rac1 expression (Fig. 7.10). Furthermore, the increased myosin activity of HGF treated cells (Fig. 7.3) substantiates the hypothesis that the cortical network plays a crucial role for the migratory behavior of non-confluent epithelial cells. However, biological experiments specifically addressing this presumption have to be performed to confirm the connection between cortical network occurrence. For example, inducible RhoA or Rock knock down while tracking network behavior and migratory activity of single cells could lead to important findings regarding the direct connection between the cortical network function and migration.

In general, we conclude from screening the regulatory machinery impact on the myosin network that we can easily change the mean velocity thus the myosin activity. However, the oscillation period of the network appears to be relatively robust against changes in the regulating pathways. While we can slow the oscillation down by inhibiting the active state of myosin, which is a logic effect, increasing the periodicity seems to be a non trivial task. Our approach of hyper activating myosin by blocking the myosin phosphatase with Calyculin A (Fig. 7.11) has induced no significant effects on the dynamical features or specifically oscillation period. Hence, we presume that characteristic network oscillations are only partially mediated by an underlying driving mechanism. The periodic changes between slow and fast reorganization could well be an intrinsic feature of an active and tensile actomyosin network as has been beautifully demonstrated *in vitro* with a minimal actomyosin system (Ref.[125]).

Chapter 8

Cortical network stiffness characterization and incision response

8.1 Introduction

Until here, we have presented experimental data and image analytical methods to describe the dynamical features of the myosin network structure and find the underlying driving mechanism leading to oscillation patterns in dynamical rearrangement. However, in recent years increasing focus has been put on questions regarding mechanotransduction and mechanoresponse. In fascinating experiments Disher *et al.* (Ref.[28]) and others have shown that cells feel and respond to the stiffness properties of the substrate. Moreover, mechanosignaling to the cell nucleus causing changes in gene expression has been reported (Ref.[154]). On the other hand the cell stiffness itself is controlled by cell shape and substrate rigidity (Ref.[164]). In organisms this interplay between substrate and cell stiffness could well act as a feed-back loop for quick adaption to microenvironmental changes. Hence it is highly important to physically characterize the stiffness properties of epithelial cells as they will presumably affect other cell or tissue responses in the physiological context of whole organisms.

We here present data of combined AFM and fluorescence microscopy data acquisition, a highly advanced and challenging experimental approach. In cooperation with the group of Prof. H. Oberleithner at the University of Muenster, Institute of Physiology II we monitor simultaneously the cell cortical elasticity by probing the cortex with AFM and the myosin network rearrangements by fluorescence microscopy. We can confirm a previously reported oscillatory change of cell elasticity over time (Ref.[148]) with similar oscillation periods compared to a network reorganization cycle time of about 200 seconds. However, though using cross-correlation analysis on the two signals of cellular elasticity and optical flow velocity we can not verify a direct correlation between these two oscillating signals.

Moreover, we present very recent and preliminary data of an unsuspected effect of the myosin network behavior when disturbing the cell cortical dynamics by cutting large cortical incisions using our ablation setup. The cut through large parts of the cortical network completely stalls the motion of the remaining myosin network structure dynamics suggesting that a force balance is of absolute necessity to retain the network function. In future investigations a strong focus should be put on these experiments as they will presumably lead to insights regarding the cellular function of the apical myosin network structure.

8.2 Cell elasticity and cortical tension correlation by simultaneous AFM and fluorescence measurement

It has been reported recently that epithelial cells undergo oscillatory change of cell elasticity (Ref.[148]). Schillers *et al.* revealed by AFM measurements that this oscillation in elasticity was myosin II dependent as they could inhibit oscillation using drugs as Latrunculin A (chapter 5), blebbistatin (chapter 3) or the calcium chelator Bapta-AM (chapter 7). We have already presented similar effects of these drugs on the oscillatory behavior of myosin. Hence we hypothesized that a direct connection between the change in elasticity and the observed oscillation patterns of myosin reorganization could exist. To confirm this assumption we performed simultaneous AFM and fluorescence microscopy in cooperation with Dr. J. Fels from the group of Prof. H. Oberleithner. As depicted in Fig. 8.1 we performed experiments using a sophisticated AFM setup mounted in a fluid chamber to enable live cell microscopy and used polystyrene microsphere cantilevers with a sphere size of 1μm (Fig. 8.1, left). As fluorescence microscope we used a confocal microscope for which we had to adapt our image filtering procedure due to resolution differences. After optimizing parameters of the block matching 3D filter (chapter 2.5.1) we obtained comparable fluorescence images of the myosin network structure (Fig. 8.1, middle). Scanning three focal planes with $\Delta z = 1\mu$m distance and subsequent maximum projection were performed as in previous experiments. In rare events we could detect a fluorescence signal from the 1μm AFM probe microsphere (Fig. 8.1, middle, arrow) which however did not interfere with our measurements. For analysis we cut 100x100 pixel large image areas (2x2μm, Fig. 8.1, middle, rectangles) of AFM measured regions for further image analysis using the optical flow approach (chapter 6).

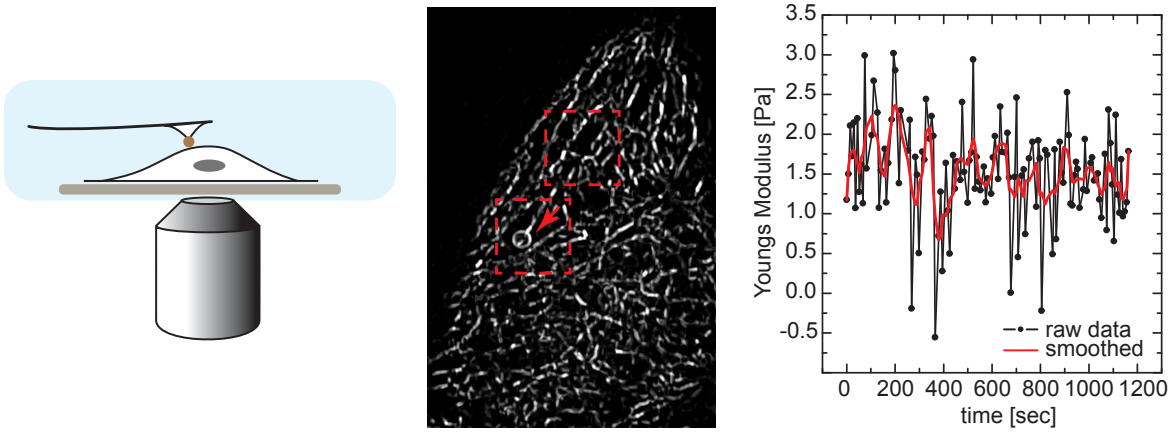

Figure 8.1: Combined AFM and fluorescence microscopy using 1μm polystyrene microsphere cantilever in fluid chamber (left) and confocal fluorescence microscope (middle). 100x100 pixel sections of image sequence were used for optical flow analysis (middle, rectangles). Rarely, microsphere fluorescence signal was detected (middle, arrow). AFM measurement reveals oscillatory change of cell elasticity (right).

Measurements of cell elasticity were performed by pushing the AFM cantilever a defined distance (1μm) into the cell cortex and subsequently calculating the elastic part of the deflection

curve considering the spring constant of the cantilever and other physical properties of the setup (Ref.[148]). As for the former study of Schillers *et al.* we could identify an oscillatory behavior of the cell elasticity after smoothing the data using adjacent averaging with a five point averaging window (Fig.8.1, right, red line).

Next we simultaneously monitored elasticity and fluorescence signal. As shown for three exemplary runs of experiment (Fig. 8.2, left) both elasticity (blue curves) and mean velocity of optical flow (red curves) exhibited oscillatory behavior on similar time scales.

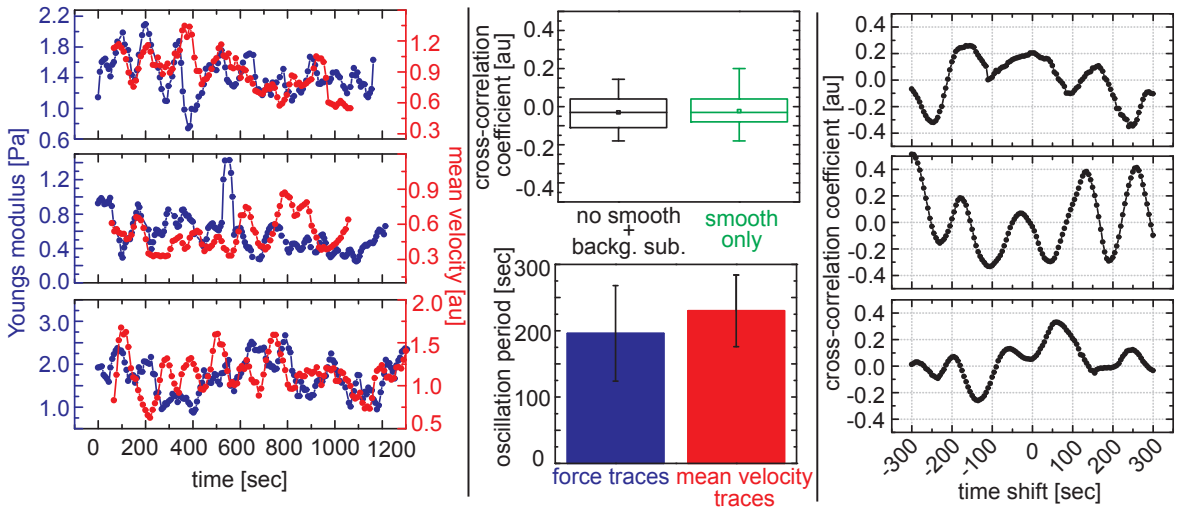

Figure 8.2: Results of combined AFM (left, blue curves) and fluorescence measurements (left, red curves) subsequently analyzed by cross-correlation analysis (middle, upper panel) and autocorrelation analysis (middle, lower panel) revealing no cross-correlation but similar oscillation periods. Time-shifted cross-correlation does not result in finding characteristic lag time (right).

To measure the correlation between cell elasticity and mean velocity oscillations we calculated the Pearson cross-correlation coefficient between the two signals using the 'cov'-function of Matlab (chapter 2.5.4). Prior to cross-correlation calculation we processed the signals either by incorporating a background subtraction step for the optical flow signal to suppress photobleaching effects such as constant signal decrease (as in Fig. 6.13, right) or we applied an additional smoothing procedure for both signals to circumvent small signal fluctuation interferences. However, in neither case we could deduce correlative or anti-correlative behavior of the two signals (Fig. 8.2, middle, upper panel). Cross-correlating signals of eleven independently measured cells resulted in no correlation as mean cross-correlation coefficients were always close to zero.

As we could not confirm a direct correlation between the two signals though the traces were oscillating on similar time scales we next performed autocorrelation analysis for each signal trace to deduce oscillation periods (Fig. 6.14, right). As assumed, the periodicity time scales of ten different force and mean velocity traces respectively were both in good agreement with mean velocity oscillation period (230 ± 54) seconds being slightly above the force trace period (196 ± 72) seconds (Fig. 8.2, middle, lower panel). Hence, even though we could not verify the

direct correlation between cellular elasticity and apical myosin network activity oscillation we revealed that both processes appeared on the same time scale.

In a last step to find a possible correlation between elasticity and mean velocity we time-shifted the signals with respect to each other and subsequently calculated the resulting cross-correlation coefficient for each time shift step. This approach allowed to deduce potential lag times between the two oscillatory signals implying that one oscillatory process results as a consequence of the other one. However, as exemplary shown (Fig. 8.2, right), time-shifting the signals (Fig. 8.2,left) did not lead to coherent results of an existing lag time. Though the time-shifted cross-correlation curve examples resemble each other somehow, more careful analysis of all eleven experimental runs did not verify this resemblance. Here, more data would be of high importance to more robustly investigate possible correlations. However, the sophisticated simultaneous fluorescence imaging and AFM measurements imply a multitude of crucial experimental conditions and are therefore highly complex, error-prone and time consuming experiments that will have to be performed during future investigations.

One possible solution for the lack of correlation between cell elasticity and mean velocity could be the perpendicular directionality of the two force related processes. While cell elasticity is measured perpendicular to the apical cell membrane the myosin reorganization speed dependent change in cortical tension propagates membrane parallel (Fig. 8.3, left, schematic). To test, if the change in myosin dependent tension was related to a cellular swelling and compression that could be measured by AFM, we developed an image analysis tool based on image stack registry (Ref.[41]). This mathematical process relates to a geometric transformation for aligning two images into the same coordinate system by a combination of (1) translation, (2) rotation and (3) scaling steps (Fig. 8.3, right, upper panel).

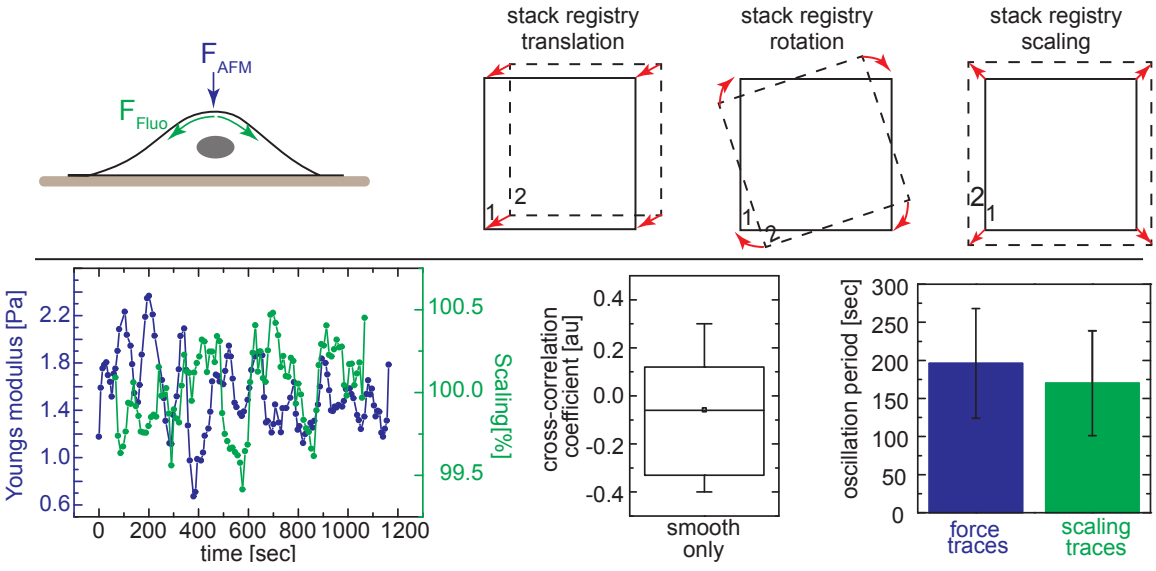

Figure 8.3: Image stack registry (upper panel) to extract possible cortical swelling and compression using scaling (upper panel, right) as parameter. Scaling parameter oscillates (lower panel, green) but correlation to elasticity (lower panel, blue) indicates no correlative dependency (lower panel, middle) though oscillation periods are similar (lower panel, right). n=10

The developed Matlab algorithm monitored all three parameters when registering the image sequence with an oversampling rate of one image. While translation and rotation was of minor interest for our intentions the scaling parameter monitored directly possible cortical surface swelling and compression. After smoothing procedure using five points adjacent averaging we could identify oscillatory changes in the scaling parameter as well (Fig. 8.3, left, lower panel). However, these changes appeared on a scale of ± 0.5 percent of enlarging or shrinking images and were thus relatively small changes. Nevertheless, we calculated the cross-correlation coefficients between cell elasticity and scaling signal which resulted in a wider distribution of coefficients but a mean value of zero correlation. Similar to the above described comparison between elasticity and mean velocity (Fig. 8.2) scaling and elasticity did therefore not correlate with each other. However, calculating the oscillation period of the scaling fluctuations we obtained a mean periodicity of (170 ± 69) seconds thereby being slightly faster than the cell elasticity oscillations (Fig. 8.3, right, lower panel). However, as already mentioned above more experimental data would here facilitate analysis and highly enhance the chance to find the physical connection between the two cell mechanical properties of tension and elasticity.

8.3 Large cortical incisions – research in progress

Notably, the latest state of the art experiments using the newly installed ablation setup revealed very promising and interesting results though these results were to the date of finishing this thesis not yet robustly confirmed. However, these research in progress results gave insights into a mechanical feature of the apical myosin network structure thereby pointing towards an alternative explanation for the oscillatory network. Without claiming to present robustly validated data we want to shortly describe the preliminary results here to complement our current picture of the apical myosin network organization and characteristics.

In contrast to the $1 - 3\mu$m small cuts of the myosin network structure, that we already described in chapter 4.10 (Fig. **??**), we here changed the experimental procedure to induce large cortical incisions (Fig. 8.4,upper panel, blue line) causing a full loss of tension within the cortical myosin network. The laser ablation cut was optimized in intensity so as to no membrane blebbing or other cell death characteristic effects such as apparent membrane injury or quick cell rounding and substrate detachment were observable (Ref.[35],[17],[93]). We assumed that by monitoring the apical myosin network structure over a long time range we could gain novel insights into the remodeling properties of the reconstituting network.

Surprisingly, we observed a very unusual and exceptional cellular behavior of the myosin network. After the large cortical incision (Fig. 8.4, upper panel, blue line) we first observed the very rapid tension release causing the large gap in network structure visible in the upper panel. Thereafter, we monitored the astonishing effect of a complete loss of dynamics within the remaining myosin structures for more than 600 seconds (Fig. 8.4, upper panel and kymograph). The cortical myosin network structure seemed to be stuck within the cell cortex. Sudden cell death was seemingly not the case as the cell would then eventually detach from the substrate or show plasma membrane injury effects. Further preliminary experimental runs resulted in even longer times of dynamics loss up to 60 minutes (data not shown). One possible explanation for the cells inability to quickly reconstitute its myosin network structure

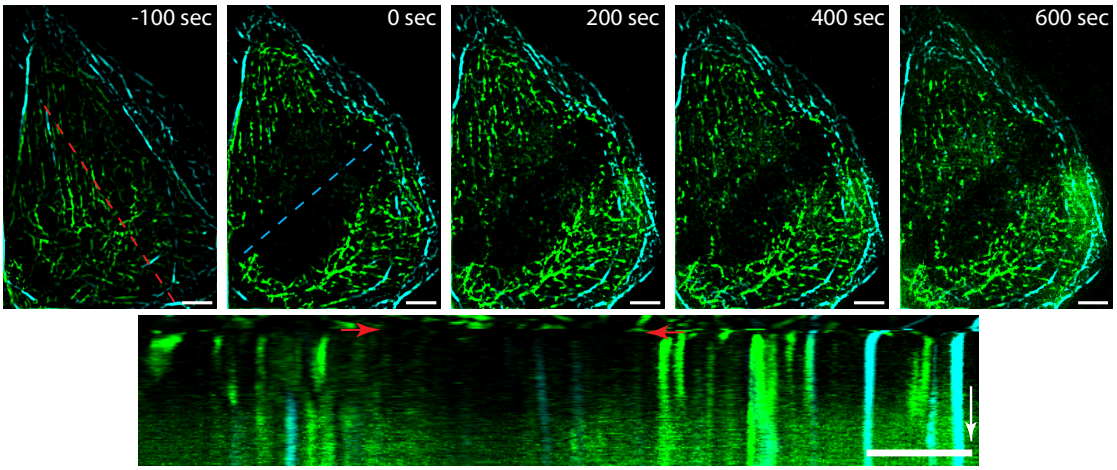

Figure 8.4: Large cortical incision (blue line, second image) stalls myosin network motion for over 600 seconds as visualized by kymograph (lower panel, red line). Red arrows in kymograph mark recoiled region after cut. Scale bar: 5μm time arrow: 400sec

could be the loss of physical anchor points necessary to counterbalance the tension establishment. Clarifying which physical mechanisms stall the myosin dynamics for such long times will be a very interesting and promising task in future experiments that should range from monitoring the final onset of network recovery, finding the critical point between fast tension recovery after small cuts (Fig. 4.13) and stalling of the dynamics after large incisions (Fig. 8.4) as well as describing in detail the innercellular responses and rearrangements caused by such a large cortical incision.

8.4 Discussion

In this last chapter we presented data of a highly advanced experimental approached based on the simultaneous use of AFM and fluorescence microscopy. We show that both, cell cortex elasticity and optical flow velocity, oscillate on very similar time scales. However, we can not find a direct correlation between the cell elasticity oscillation and the presumably pulsatile increase and decrease of cortical network tension leading to oscillations in the flow velocity. Why we are not able to resolve the interdependence of these two effects remains to be elucidated in future experiments. One possible solution to this lack of correlation might be the perpendicular alignment of force distribution with cell elasticity measured perpendicular to the cell cortex membrane while the tensional forces mediated by the myosin network propagate parallel to the cell cortex (Fig. 8.3, scheme). The resulting compaction of the inner cell leading to stiffening might be dependent on additional factors such as innercellular cytoskeletal elements, e.g. microtubule or intermediate filaments, that could serve as a buffer for the cell compacting cortical tension. However, even an alternative image analysis approach based on image registry to deduce a possible perpendicular force component from the fluorescence images has not resulted in successfully correlating tension and elasticity.

Though we still lack the knowledge of the interlinking component between the cell elasticity and the cortical tension oscillation we can however hypothesize about the possible cell regulatory functions of the oscillating network. Khatau *et al.* (Ref.[76],[77]) have published very convincing data of a perinuclear actin cap in fibroblasts that regulates the cell nucleus shape and thereby directly influences transcriptional activities (Ref.[108],[154]). Kim *et al.* (Ref.[78]) have subsequently shown that the actin cap associates with focal adhesions and plays distinct roles in cellular mechanosensing. In contrast to actin caps the here described cortical network structure seems to be uncoupled from the basal plane of the cell regarding force distribution dependencies (Fig. 4.12) as it can be destabilized without interfering with stress fiber structures. Though differences between actin caps and our cortical structures are apparent we hypothesize that this cortical network regulates similarly nucleus position and shape. Supporting this hypothesis would be straight forward using nucleus labeling proteins such as H2B and perform experiments such as HGF or Latrunculin treatment as well as cortical ablations. Monitoring at the same time the myosin network and the nucleus should then determine whether or not the cortical network structure is responsible for nucleus positioning.

The discussed connection of the actin cap to the focal adhesions (Ref.[78]) is another intriguing question considering the force balances within the apical myosin networks. We have so far not been able to resolve the linker protein that serves as the fix point to counterbalance tensional forces. It could be possible that the network is different to actin cap organization by means of being in a quasi stable state with isotropic tensional forces balancing out due to its highly isotropic structure. This so called tensegrity approach for describing the actomyosin network is a model intensively discussed in the field (Ref.[66],[65]) as then the actomyosin network would have the important key property that rearrangement can take on multiple size scales without instantaneously changing the overall structural integrity of the network. Moreover, transmission of mechanical forces over long distances are largely facilitated when considering the network as a tensegrity structure (Ref.[66]). In this context, the last presented experiments of large cortical incisions becomes an important first indication that the cortical myosin is indeed controlled by the counterbalance of tension and compression elements being the basic components of a tensegrity unit. While small cuts in the network do not result in the complete collapse of the structure (Fig. 4.13) an incision larger than the largest prestressed tensegrity unit leads to the immediate collapse of the complete network dynamics. Concluding, it will be at the same time intriguing and important to more carefully investigate the physical effects and responses caused by large scale incisions in the apical myosin network.

Chapter 9

General discussion and outlook

This section of general discussion serves as a recapitulation of the most important findings and results of this thesis. Detailed discussions of all specific results are already part of each chapter and will therefore not be restated here. The final paragraph will give a short outlook of possible future directions to further understand conceptual properties of isotropic actomyosin networks in cells and their role in supporting the mechanical properties of epithelial cells including shape maintenance, migration and signal transduction.

In this thesis we focus on the actomyosin structure and dynamics at the apical side of non-confluent epithelial cells. While we observe static microvilli organization in confluent epithelial cells (Ref.[11]), we monitor highly dynamic elongated and frequently bent actin filled apical protrusions (Fig. 3.16) that rearrange on time scales of roughly one minute (Fig. 3.17). In addition, these apical protrusions are frequently arranged parallel to the membrane rather than perpendicular. Despite these characteristic differences, compared to classical brush border microvilli (Ref.[56]), we classify the actin structures as microvilli due to similarities in protein composition and topology (Ref.[79]) (Fig. 3.5). However, the question remains, what distinct role these non-confluent highly dynamic microvilli serve in the cell?

Already in the 1970's examples of bent and elongated microvillar structures have been reported in scanning electron microscopy and fluorescence images (Ref.[13],[20]), though the focus has never been placed on characterizing their dynamic behavior. This gap of knowledge is presumably caused by the fact that epithelial cells are usually under investigation in the physiological context of cell sheet monolayers. The occurrence of the non-confluent cell situation is already a specialized situation e.g. during wound healing. This is supported by our observation that elongated microvilli protrusions can be experimentally induced in wound healing experiments (Fig. 3.13). Like actin filled filopodia protrusions at the basal surface of migrating non-confluent epithelial cells (Ref.[46]), the apical elongated microvilli might act as mechanosensing antennas. The constant remodeling of the elongated structures suggests that the apical cell region is used to scan for potential barriers such as cell neighbors. In this context the occurrence of strongly extended protrusions upon HGF treatment (Fig. 3.14) suggests a similar functional role as the morphologically similar filopodia (Ref.[141]). Filopodia are commonly related to being highly dynamic extending and retracting protrusions which explore the extracellular matrix and surface of other cells as a sensing unit (Ref.[180]). Microvilli, on the other hand, are known to store calcium ions (Ca^{2+}) (Ref.[90]). Thus, elongated apical protrusions would be ideal candidates to act as mechanosensing units that are able to release calcium signal upon external physical perturbances. This close resemblance of filopodia and elongated microvillar structures in epithelial cells has been recently proposed (Ref.[150])

based on the occurrence of similar actin bundling proteins, villin and fascin, in both structures. Hence, it will be very interesting in future experiments to functionally test the role in apical elongated microvilli protrusions by gene specific knock down. These knock down experiments might, however, be of limited informative value due to the presence of multiple other actin bundlers, which possibly confer functional redundancy.

The most important finding of this thesis is certainly the identification of an isotropic apical actomyosin network spanning the whole cell cortex of non-confluent epithelial cells (Fig. 4.2). Interestingly, this isotropic network seems to be a general feature of non-confluent migrating epithelial cells as we demonstrate the presence of comparable networks in various model cell lines from different physiological backgrounds (Fig. 4.4). We can further show that the apical isotropic network is the driving force responsible for the highly dynamic reorganization of the elongated microvilli protrusions (Fig. 3.20 and 4.12) which are mechanically linked to this cortical plasma membrane parallel actomyosin network (Fig. 5.3 and 5.4). The question, however, remains if this actomyosin structure only serves as a motion driving unit for apical microvilli or if there is a more general cellular function of this isotropic network?

Unfortunately we were not able to analyze the function of the cortical network with genetic knock down or knock out approaches nor with chemical inhibitors without affecting other actin structures. Nevertheless, we showed that the network is only present in non-confluent cells (Fig. 4.2) and in migrating cells at the border of closing wounds (Fig. 4.5). Thus, the network is hypothetically functioning as a cellular shape control for cells without mature cell-cell contacts. We can furthermore show that the actomyosin network has a functional link to the basal cell plane as the apical structure disassembles when cells are seeded on fibronectin coated micro-patterns of varying geometry (Fig. 4.7). The hindrance of cell migration from the small patterns by surrounding substrate inactivation, resulting in network disassembly is a reasonable hint towards a biological role in cell migratory regulation. Moreover, a similar apical actomyosin structure named 'actin cap' has been reported to position, control and influence the cell nucleus of migrating mouse embryonic fibroblasts (Ref.[76]). This apical cortex spanning actin fiber network is integrated into the basal plane via specific focal adhesion complexes and is implicated in functional mechanosensing of substrate elasticity (Ref.[78]). Although we could not detect a physical connection between the apical and basal actomyosin structures in non-confluent epithelial cells, a comparable link seems possible (Ref.[88]).

Intriguingly, we could demonstrate that the isotropic actomyosin network is prestressed (Fig. 4.13). Such tensile-loaded networks in cells have been reported to act as key players in various developmental processes such as gastrulation (Ref.[104]), germband extension (Ref.[132]), tension mediated tissue elongation (Ref.[34],[51]), apical constriction (Ref.[105]) or tension anisotropy based polarizing cortical flow (Ref.[107]). Notably, all these processes involve tissue level morphogenetic reorganization while the driving actomyosin based tension is generated on a cellular level. Levayer and Lecuit (Ref.[94]) discuss that several different regulating protein cascades lead to the activation of cellular tension depending on the morphogenetic process. Differences should be seen regarding temporal actomyosin tension behavior depending on the involved myosin isoform MHCA or MHCB (chapter 4.1). While myosin IIA should be a fast motor efficient for rapid remodeling processes due to its higher ATPase activity (Ref.[83]), myosin IIB related processes should be more stress resistant due to higher duty ratio of MHCB and its longer ADP removal kinetics (Ref.[94]). We were not able to

confirm these differences when comparing MHCA and MHCB network characteristics within a project related bachelor thesis (Ref.[185]).

We can however confirm that MHCA exhibits very adaptive contractile activity by treating non-confluent cells with small amounts of actin severing Latrunculin B drug (Fig. 4.12). Induced by local rupture of actomyosin structures, the resulting long-range network rearrangements last over ten minutes indicating that the network is able to quickly adapt and restructure upon small external interferences. Additionally we can demonstrate by these drug experiments that the network reorganizes in an oscillatory fashion (Fig. 4.12).

All actomyosin tension-dependent processes described in the preceding paragraphs reveal pulsatile or oscillatory actomyosin network behavior. Indeed, as our third key finding of this thesis we reveal oscillatory cortical network behavior (Fig. 6.4). This finding is based on an image analysis method developed in this thesis and called incremental temporal image correlation (ITIC, chapter 6.3). By analyzing the characteristic correlation time for each frame using temporal correlation analysis, we observe a periodic change between times of high and low reorganization speed. Notably, this important finding was purely based on developing image analysis tools to characterize the network dynamics. It, thus, shows the high importance of not only performing high level fluorescence microscopy but also of dedicating time to analyze the image sequences thoroughly. To accomplish an in depth image analysis of the dynamical network features we furthermore adapted the so called optical flow method (chapter 6.4) apart from ITIC. While the incremental temporal correlation extracts global network features, the optical flow analysis returns detailed insights in the local subcellular dynamic changes. We can demonstrate by this method that dynamic rearrangements on a subcellular scale occur within the apical cell cortex, leading to shear stress and friction within the cell cortex. We had, however, difficulties to parametrize the detailed information of the optical flow velocity maps due to very heterogeneous cell behavior. Trying various approaches of feature extraction, following e.g. Serra-Picamal *et al.*, by using a dimension compressed kymograph (Ref.[151]) or Tambe *et al.* by calculating the principle stress components (Ref.[163]), all failed to parametrize robustly the velocity fields. As a basic method of checking and quantifying the optical flow calculation, we developed the 'virtual beads' approach (Fig. 6.12) that locally followed the flow field intensity and direction thereby returning general network behavior. Finally, we have developed an algorithm that extracts local dynamic features such as the mean absolute flow velocity, myosin activity potential and, using signal autocorrelation correlation, the network reorganization oscillation period (Fig. 6.14). This parametrization allows us to quantify and compare large data sets of control versus treated cell cortex network behavior.

Intriguingly, the oscillatory behavior could be, in general, a result of two rather different effects. Either this oscillation is driven by an underlying regulatory pacemaker or it is spontaneously occurring. To test the first hypothesis we analyzed the effects of a broad range of myosin activity regulating proteins (chapter 7). This large screen on the myosin regulators identified Rock and RhoA to play an important role in the maintenance and dynamic regulation of the apical actomyosin network (chapter 7.8). This finding is in very good accordance to previously reported functions of RhoA regulating cell body contractility (Ref.[131], [51]). Moreover, RhoA, as well as its counterplayer Rac1, are involved in actin and adhesion dynamics thereby controlling cell migration (Ref.[123]). We already discussed in the beginning of this section a possible functional role of the myosin network for cell migration. Hence, the

RhoA dependency of this oscillatory behavior of isotropic apical structures is a further strong argument in support of this hypothesis.

As an alternative explanation and judging from a more biophysical and theoretical point of view, the oscillation of this network could as well be an intrinsic effect of local network force imbalances. It has been described that oscillations of actomyosin networks can occur by emerging from a collective activation of motor proteins that spontaneously breaks the symmetry of the isotropic force balance (Ref.[94],[72],[73]). Moreover, *in vitro* assays as well as models of minimal actomyosin systems (Ref.[16],[125]) confirm the possibility of spontaneously occurring oscillations emerging from collective dynamics of motor proteins and load dependence. As all prerequisites for spontaneous oscillation seem to be present in the newly identified actomyosin network, it is worthwhile to follow this hypothetical mechanism in future investigations. Here, a more detailed physical characterization of the actomyosin network based on the optical flow velocity fields could help to understand the mechanistic dependencies. One possibility could be to describe the isotropic actomyosin cell cortex structure as an active gel with viscoelastic properties on short time scales and fluid-like properties on long time scales, as has been proposed by Joanny *et al.* (Ref.[69]). Active gels can, in general, be characterized using parameters such as flow velocity gradient, stress component σ, ATP consumption rate and polarization fields (Ref.[70]). Except for ATP consumption rate, these parameters should, in principle, be possible to extract from the optical flow fields allowing for at least rough estimates describing the mechanical properties of the actomyosin cell cortex. While this newly identified system has the big advantage to allow the study of a quasi 2D isotropic actomyosin network behavior directly in its natural cellular environment, rather than in reconstituted *in vitro* assays (Ref.[64]), one drawback results from that situation. In the cellular environment, it is not possible to precisely characterize and control additional factors involved in the network maintenance and dynamics, such as cross-linking proteins and polymerization nucleators, as well as measuring the ATP consumption of the active network. This drawback presumably makes the characterization of the mechanical network properties by active gel theory a difficult task that should nonetheless be taken on in future experiments to shed light on the physical basis of the occurring oscillations.

The preliminary experiments of cutting through large sections of the network, presented in the last part of the thesis (chapter 8, Fig. 8.4), displays another intriguing investigation path to follow in the future. While small cuts through the actomyosin network result in short term tension release and subsequent network reconstitution (Fig. 4.13), large incisions seem to disturb the complete cortical tension force distribution, resulting in complete motion loss of the remaining network fractions. This effect can be, as already discussed, described using the tensegrity model. It would therefore be of high interest to test the whole dimension range and determine a phase diagram of the characteristic incision length that defines the border between network reconstitution and network disintegration. Moreover, the ablation experiments could be an ideal method to measure the network adaptation to medium force disturbances, for example, by cutting one of the three network anchor points or cutting through the equatorial ring (Fig. 4.6).

A future direction for the biological characterization of the cortical actomyosin network would certainly include continued investigations of the myosin activity regulating proteins, as already started in chapter 7. Moreover, performing cell migration assays while interfering with the network dynamics could verify our hypothesis about the functional role of the apical network.

In addition, the correlation between the cortical network and the cell nucleus behavior should be investigated. This might allow us to close the gap between the above discussed 'actin caps' in mouse embryonic fibroblasts and the here identified apical actomyosin network. Finally, the localization and function of additional network components should be investigated by monitoring cross-linking proteins, formins and actin-membrane interlinking proteins. In conclusion, these proposed future research goals should finally elucidate the functional role of the apical actomyosin network, refine the knowledge about the adaptability and mechanical response to external cues and shed light on the general concept of emerging actomyosin oscillations that play important roles in cell and developmental processes.

Bibliography

[1] Seyda Acar, David B Carlson, Madhu S Budamagunta, Vladimir Yarov-Yarovoy, John J Correia, Milady R Niñonuevo, Weitao Jia, Li Tao, Julie A Leary, John C Voss, James E Evans, and Jonathan M Scholey. The bipolar assembly domain of the mitotic motor kinesin-5. *Nature Communications*, 4:1343(11), January 2013.

[2] Jeremy Adler and Ingela Parmryd. Quantifying colocalization by correlation: The Pearson correlation coefficient is superior to the Mander's overlap coefficient. *Cytometry Part A*, 77A(8):733–742, March 2010.

[3] Thomas E Angelini, Edouard Hannezo, Xavier Trepat, Jeffrey J Fredberg, and David A Weitz. Cell Migration Driven by Cooperative Substrate Deformation Patterns. *Physical Review Letters*, 104(16):168104(4), April 2010.

[4] D Axelrod, D E Koppel, J Schlessinger, and E Elson. Mobility measurement by analysis of fluorescence photobleaching recovery kinetics. *Biophysical Journal*, 16:1055–1069, 1976.

[5] M J Black and P Anandan. The Robust Estimation of Multiple Motions: Parametric and Piecewise-Smooth Flow Fields. *Computer vision and image understanding*, 63(1):75–104, 1996.

[6] G W Bourne and J M Trifaro. The gadolinium ion: A potent blocker of calcium channels and catecholamine release from cultured chromaffin cells. *Neuroscience*, 7(7):1615–1622, 1982.

[7] A Boyde and E Maconnachie. Morphological correlations with dimensional change during SEM specimen preparation. *Scanning electron microscopy*, 4:27–34, January 1981.

[8] Clifford P Brangwynne, Gijsje H Koenderink, Frederick C MacKintosh, and David A Weitz. Intracellular transport by active diffusion. *Trends In Cell Biology*, 19(9):423–427, September 2009.

[9] Clifford P Brangwynne, Frederick C MacKintosh, Sanjay Kumar, Nicholas A Geisse, Jennifer Talbot, L Mahadevan, Kevin K Parker, Donald E Ingber, and David A Weitz. Microtubules can bear enhanced compressive loads in living cells because of lateral reinforcement. *The Journal of Cell Biology*, 173(5):733–741, 2006.

[10] A Bretscher. Localization of actin and microfilament-associated proteins in the microvilli and terminal web of the intestinal brush border by immunofluorescence microscopy. *The Journal of Cell Biology*, 79(3):839–845, December 1978.

[11] A Bretscher. Microfilament structure and function in the cortical cytoskeleton. *Annual Review of Cell Biology*, 7:337–374, 1991.

[12] Thomas Brox, Andrés Bruhn, Nils Papenberg, and Joachim Weickert. High Accuracy Optical Flow Estimation Based on a Theory for Warping. In *Computer Vision-ECCV 2004*, pages 25–36. Springer Berlin Heidelberg, Berlin, Heidelberg, 2004.

[13] U Brunk, J Schellens, and B Westermark. Influence of epidermal growth factor (EGF) on ruffling activity, pinocytosis and proliferation of cultivated human glia cells. *Experimental cell research*, 103:295–302, 1976.

[14] K Burridge and K Wennerberg. Rho and Rac Take Center Stage. *Cell*, 116:167–179, 2004.

[15] F Bussolino, M F Di Renzo, M Ziche, E Bocchietto, M Olivero, L Naldini, G Gaudino, L Tamagnone, A Coffer, and P M Comoglio. Hepatocyte growth factor is a potent angiogenic factor which stimulates endothelial cell motility and growth. *The Journal of Cell Biology*, 119(3):629–641, 1992.

[16] O Campàs, C Leduc, P Bassereau, J-F Joanny, and J Prost. Collective Oscillations Of Processive Molecular Motors. *Biophysical Reviews and Letters*, 04:163–178, April 2009.

[17] Guillaume Charras and Ewa Paluch. Blebs lead the way: how to migrate without lamellipodia. *Nature Reviews Molecular Cell Biology*, 9(9):730–736, July 2008.

[18] C S Chen, J Tan, and J Tien. Mechanotransduction at cell-matrix and cell-cell contacts. *Annual Review of Biomedical Engineering*, 6:275–302, 2004.

[19] Ekta Seth Chhabra and Henry N Higgs. The many faces of actin: matching assembly factors with cellular structures. *Nature Cell Biology*, 9(10):1110–1121, October 2007.

[20] M Chinkers, J A McKanna, and S Cohen. Rapid induction of morphological changes in human carcinoma cells A-431 by epidermal growth factors. *The Journal of Cell Biology*, 83:260–265, 1979.

[21] Kristopher Clark, Michiel Langeslag, Carl G Figdor, and Frank N van Leeuwen. Myosin II and mechanotransduction: a balancing act. *Trends In Cell Biology*, 17(4):178–186, April 2007.

[22] M A Conti and R S Adelstein. Nonmuscle myosin II moves in new directions. *Journal of Cell Science*, 121(1):11–18, January 2008.

[23] Nancy Costigliola, Maryna T Kapustina, Gabriel E Weinreb, Andrew Monteith, Zenon Rajfur, Timothy C Elston, and Ken Jacobson. RhoA Regulates Calcium-Independent Periodic Contractions of the Cell Cortex. *Biophysical Journal*, 99(4):1053–1063, August 2010.

[24] K Dabov, A Foi, and V Katkovnik. Image Denoising by Sparse 3–D Transform–Domain Collaborative Filtering. *IEEE TRANSACTIONS ON IMAGE PROCESSING*, 16(8):20802095, 2007.

[25] Hassina Darenfed, Bama Dayanandan, Tong Zhang, Sidney H K Hsieh, Alyson E Fournier, and Craig A Mandato. Molecular characterization of the effects of Y-27632. *Cell Motility and the Cytoskeleton*, 64(2):97–109, 2007.

[26] B F De Blasio, J A Rottingen, K L Sand, I Giaever, and J G Iversen. Global, synchronous oscillations in cytosolic calcium and adherence in bradykinin-stimulated Madin-Darby canine kidney cells. *Acta Physiologica Scandinavica*, 180(4):335–346, April 2004.

[27] D J DeRosier and L G Tilney. F-Actin Bundles Are Derivatives of Microvilli: What Does This Tell US about How Bundles Might Form? *The Journal of Cell Biology*, 148(1):1–6, January 2000.

[28] D E Discher, P Janmey, and Y Wang. Tissue Cells Feel and Respond to the Stiffness of Their Substrate. *Science*, 310:1139–1143, 2005.

[29] Mohammed El-Mezgueldi and Clive R Bagshaw. *The myosin family: biochemical and kinetic properties*, volume chapter 3 of *Myosins*. Springer Netherlands, 2008.

[30] Adam J Engler, Shamik Sen, H Lee Sweeney, and Dennis E Discher. Matrix Elasticity Directs Stem Cell Lineage Specification. *Cell*, 126(4):677–689, August 2006.

[31] Sharona Even-Ram, Vira Artym, and Kenneth M Yamada. Matrix Control of Stem Cell Fate. *Cell*, 126(4):645–647, August 2006.

[32] Richard G Fehon, Andrea I McClatchey, and Anthony Bretscher. Organizing the cell cortex: the role of ERM proteins. *Nature Reviews Molecular Cell Biology*, 11(4):276–287, April 2010.

[33] J Fels, P Jeggle, K Kusche-Vihrog, and H Oberleithner. Cortical Actin Nanodynamics Determines Nitric Oxide Release in Vascular Endothelium. *Plos One*, 7(7):e41520(11), 2012.

[34] Rodrigo Fernandez-Gonzalez, Sérgio de Matos Simoes, Jens-Christian Röper, Suzanne Eaton, and Jennifer A Zallen. Myosin II Dynamics Are Regulated by Tension in Intercalating Cells. *Developmental Cell*, 17(5):736–743, November 2009.

[35] I Joris G Majno. Apoptosis, oncosis, and necrosis. An overview of cell death. *The American Journal of Pathology*, 146(1):3–15, January 1995.

[36] Brian J Galletta and John A Cooper. Actin and endocytosis: mechanisms and phylogeny. *Current Opinion In Cell Biology*, 21(1):20–27, 2009.

[37] Damien Garbett, David P LaLonde, and Anthony Bretscher. The scaffolding protein EBP50 regulates microvillar assembly in a phosphorylation-dependent manner. *The Journal of Cell Biology*, 191(2):397–413, 2010.

[38] M L Gardel, F Nakamura, J H Hartwig, J C Crocker, T P Stossel, and D A Weitz. Prestressed F-actin networks cross-linked by hinged filamins replicate mechanical properties of cells. *Proceedings of the National Academy of Sciences*, 103(6):1762–1767, February 2006.

[39] M L Gardel, J H Shin, F C MacKintosh, and L Mahadevan. Elastic Behavior of Cross-Linked and Bundled Actin Networks. *Science*, 304:1301–1305, 2004.

[40] Benjamin Geiger, Joachim P Spatz, and Alexander D Bershadsky. Environmental sensing through focal adhesions. *Nature Reviews Molecular Cell Biology*, 10(1):21–33, January 2009.

[41] A Ardeshir Goshtasby. Image Registration Methods. In *Image Registration*, pages 415–434. Springer London, London, 2012.

[42] Nir S Gov and Ajay Gopinathan. Dynamics of Membranes Driven by Actin Polymerization. *Biophysical Journal*, 90(2):454–469, January 2006.

[43] Ralph Gräf, Jens Rietdorf, and Timo Zimmermann. Live Cell Spinning Disk Microscopy. In *Microscopy Techniques*, pages 57–75. Springer Berlin Heidelberg, Berlin, Heidelberg, May 2005.

[44] A Graziani, D Gramaglia, P dalla Zonca, and P M Comoglio. Hepatocyte growth factor/scatter factor stimulates the Ras-guanine nucleotide exchanger. *Journal of Biological Chemistry*, 268(13):9165–9168, 1993.

[45] Carol C Gregorio, Henk Granzier, Hiroyuki Sorimachi, and Siegfried Labeit. Muscle assembly: a titanic achievement? *Current Opinion In Cell Biology*, 11(1):18–25, February 1999.

[46] Stephanie L Gupton and Frank B Gertler. Filopodia: The Fingers That Do the Walking. *Science Signaling*, 2007(400):re5(8), August 2007.

[47] A Hall. The cellular functions of small GTP-binding proteins. *Science*, 249:635–640, 1990.

[48] John A Hammer and James R Sellers. Walking to work: roles for class V myosins as cargo transporters. *Nature Reviews Molecular Cell Biology*, 13(1):13–26, December 2011.

[49] Abraham Hanono, Damien Garbett, David Reczek, David N Chambers, and Anthony Bretscher. EPI64 regulates microvillar subdomains and structure. *The Journal of Cell Biology*, 175(5):803–813, 2006.

[50] Andrea Hartsock and W James Nelson. Adherens and tight junctions: Structure, function and connections to the actin cytoskeleton. *Biochimica et Biophysica Acta (BBA) - Biomembranes*, 1778(3):660–669, March 2008.

[51] Li He, Xiaobo Wang, Ho Lam Tang, and Denise J Montell. Tissue elongation requires oscillating contractions of a basal actomyosin network. *Nature Cell Biology*, 12(12):1133–1142, November 2010.

[52] Sarah J Heasman and Anne J Ridley. Mammalian Rho GTPases: new insights into their functions from in vivo studies. *Nature Reviews Molecular Cell Biology*, 9(9):690–701, September 2008.

[53] B Hebert, S Costantino, and P W Wiseman. Spatiotemporal Image Correlation Spectroscopy (STICS) Theory, Verification, and Application to Protein Velocity Mapping in Living CHO Cells. *Biophysical Journal*, 88:3601–3614, 2005.

[54] Harald Herrmann, Harald Bär, Laurent Kreplak, Sergei V Strelkov, and Ueli Aebi. Intermediate filaments: from cell architecture to nanomechanics. *Nature Reviews Molecular Cell Biology*, 8(7):562–573, 2007.

[55] Henry N Higgs. Discussing the morphology of actin filaments in lamellipodia. *Trends In Cell Biology*, 21(1):2–4, January 2011.

[56] N Hirokawa, L G Tilney, K Fujiwara, and J E Heuser. Organization of actin, myosin, and intermediate filaments in the brush border of intestinal epithelial cells. *The Journal of Cell Biology*, 94:425–443, 1982.

[57] Nobutaka Hirokawa, Yasuko Noda, Yosuke Tanaka, and Shinsuke Niwa. Kinesin superfamily motor proteins and intracellular transport. *Nature Reviews Molecular Cell Biology*, 10(10):682–696, October 2009.

[58] Kenneth C Holmes. Myosin Structure. In *Myosins*, pages 35–54. Springer Netherlands, Dordrecht, 2007.

[59] Richard E Honkanan, Burt A Codispoti, Kathy Tse, and Alton L Boynton. Characterization of natural toxins with inhibitory activity against serine/threonine protein phosphatases. *Toxicon*, 32(3):339–350, March 1994.

[60] Adam D Hoppe and Joel A Swanson. Cdc42, Rac1, and Rac2 Display Distinct Patterns of Activation during Phagocytosis. *Molecular Biology of the Cell*, 15:3509–3519, 2004.

[61] Berthold K Horn and Brian G Schunck. Determining Optical Flow. In James J Pearson, editor, *1981 Technical Symposium East*, pages 319–331. SPIE, November 1981.

[62] Pirta Hotulainen and Pekka Lappalainen. Stress fibers are generated by two distinct actin assembly mechanisms in motile cells. *The Journal of Cell Biology*, 173(3):383–394, May 2006.

[63] Bo Huang, Mark Bates, and Xiaowei Zhuang. Super-Resolution Fluorescence Microscopy. *Annual Review of Biochemistry*, 78(1):993–1016, June 2009.

[64] D Humphrey, C Duggan, D Saha, D Smith, and J Käs. Active fluidization of polymer networks through molecular motors. *Nature*, 416(6879):413–416, March 2002.

[65] D E Ingber. Tensegrity and mechanotransduction. *Journal of bodywork and movement therapies*, 12:198–200, 2008.

[66] Donald E Ingber. Cellular mechanotransduction: putting all the pieces together again. *The FASEB journal*, 20:811–827, 2006.

[67] H C Ishikawa-Ankerhold, R Ankerhold, and GPC Drummen. Advanced fluorescence microscopy techniques—Frap, Flip, Flap, Fret and flim. *Molecules*, 17:4047–4132, 2012.

[68] W G Jiang and S Hiscox. Hepatocyte growth factor scatter factor, a cytokine playing multiple and converse roles. *Histology and Histopathology*, 12(2):537–555, April 1997.

[69] J-F Joanny, Karsten Kruse, Jacques Prost, and Sriram Ramaswamy. The actin cortex as an active wetting layer. *The European Physical Journal E*, 36(5):1–6, 2013.

[70] Jean-Francois Joanny and Jacques Prost. Active gels as a description of the actin-myosin cytoskeleton. *HFSP Journal*, 3(2):94–104, April 2009.

[71] Frank H Johnson, Osamu Shimomura, Yo Saiga, Lewis C Gershman, George T Reynolds, and John R Waters. Quantum efficiency ofCypridina luminescence, with a note on that ofAequorea. *Journal of Cellular and Comparative Physiology*, 60(1):85–103, August 1962.

[72] F Jülicher and J Prost. Spontaneous oscillations of collective molecular motors. *Physical Review Letters*, 78(23):4510–4513, 1997.

[73] Frank Jülicher and Jacques Prost. Cooperative Molecular Motors. *Physical Review Letters*, 75(13):2618–2621, September 1995.

[74] Maryna Kapustina, Gabriel E Weinreb, Nancy Costigliola, Zenon Rajfur, Ken Jacobson, and Timothy C Elston. Mechanical and biochemical modeling of cortical oscillations in spreading cells. *Biophysical Journal*, 94(12):4605–4620, June 2008.

[75] Julia R Kardon and Ronald D Vale. Regulators of the cytoplasmic dynein motor. *Nature Reviews Molecular Cell Biology*, 10(12):854–865, December 2009.

[76] S B Khatau, C M Hale, P J Stewart-Hutchinson, M S Patel, C L Stewart, P C Searson, D Hodzic, and D Wirtz. A perinuclear actin cap regulates nuclear shape. *Proceedings of the National Academy of Sciences*, 106(45):19017–19022, November 2009.

[77] S B Khatau, D H Kim, C M Hale, R J Bloom, and D Wirtz. The perinuclear actin cap in health and disease. *Nucleus*, 1(4):337–342, 2010.

[78] Dong-Hwee Kim, Shyam B Khatau, Yunfeng Feng, Sam Walcott, Sean X Sun, Gregory D Longmore, and Denis Wirtz. Actin cap associated focal adhesions and their distinct role in cellular mechanosensing. *Scientific Reports*, 2(555):srep00555(13), August 2012.

[79] Christoph Klingner, A Cherian, P Diesinger, R Aufschnaiter, N Maghelli, T Keil, G Beck, I Tolic-Norrelykke, M Bathe, and Roland Wedlich-Söldner. An isotropic actomyosin network promotes organization of the apical cell cortex in epithelial cells. *The Journal of Cell Biology*, in revision.

[80] Gijsje H Koenderink, Zvonimir Dogic, Fumihiko Nakamura, Poul M Bendix, Frederick C MacKintosh, John H Hartwig, Thomas P Stossel, and David A Weitz. An active biopolymer network controlled by molecular motors. *Proceedings of the National Academy of Sciences*, 106(36):15192–15197, September 2009.

[81] Simone Köhler, Volker Schaller, and Andreas R Bausch. Collective dynamics of active cytoskeletal networks. *Plos One*, 6(8):e23798(8), 2011.

[82] D L Kolin and P W Wiseman. Advances in Image Correlation Spectroscopy: Measuring Number Densities, Aggregation States, and Dynamics of Fluorescently labeled Macromolecules in Cells - Springer. *Cell Biochemistry and Biophysics*, 49:141–164, 2007.

[83] M Kovacs. Functional Divergence of Human Cytoplasmic Myosin II: Kinetic Characterization Of The Non-Muscle Iia Isoform. *Journal of Biological Chemistry*, 278(40):38132–38140, July 2003.

[84] M Kovacs. Mechanism of Blebbistatin Inhibition of Myosin II. *Journal of Biological Chemistry*, 279(34):35557–35563, May 2004.

[85] M Kovacs, K Thirumurugan, P J Knight, and J R Sellers. Load-dependent mechanism of nonmuscle myosin 2. *Proceedings of the National Academy of Sciences*, 104(24):9994–9999, June 2007.

[86] K Kruse, JF Joanny, F Jülicher, J Prost, and K Sekimoto. Generic theory of active polar gels: a paradigm for cytoskeletal dynamics. *The European Physical Journal E: Soft Matter and Biological Physics*, 16(1):5–16, 2005.

[87] K Kruse and D Riveline. Forces and Tension in Development - Google Books. *Current topics in developmental biology*, 95:67, 2011.

[88] Abhishek Kumar, Ananyo Maitra, Madhuresh Sumit, Sriram Ramaswamy, and G V Shivashankar. Actomyosin contractility rotates the cell nucleus. *Scientific Reports*, 4:srep03781(7), 2014.

[89] D P LaLonde, D Garbett, and A Bretscher. A Regulated Complex of the Scaffolding Proteins PDZK1 and EBP50 with Ezrin Contribute to Microvillar Organization. *Molecular Biology of the Cell*, 21(9):1519–1529, April 2010.

[90] Klaus Lange. Fundamental role of microvilli in the main functions of differentiated cells: Outline of an universal regulating and signaling system at the cell periphery. *Journal of Cellular Physiology*, 226(4):896–927, July 2010.

[91] Thomas Lecuit and Pierre-François Lenne. Cell surface mechanics and the control of cell shape, tissue patterns and morphogenesis. *Nature Reviews Molecular Cell Biology*, 8(8):633–644, August 2007.

[92] Thomas Lecuit, Pierre-François Lenne, and Edwin Munro. Force Generation, Transmission, and Integration during Cell and Tissue Morphogenesis. *Annual Review of Cell and Developmental Biology*, 27(1):157–184, November 2011.

[93] John J Lemasters, James DiGuiseppi, Anna-Liisa Nieminen, and Brian Herman. Blebbing, free Ca2+ and mitochondrial membrane potential preceding cell death in hepatocytes. *Nature*, 325(6099):78–81, January 1987.

[94] Romain Levayer and Thomas Lecuit. Biomechanical regulation of contractility: spatial control and dynamics. *Trends In Cell Biology*, 22(2):61–81, 2012.

[95] John Limouze, Aaron F Straight, Timothy Mitchison, and James R Sellers. Specificity of blebbistatin, an inhibitor of myosin II. *Journal of Muscle Research and Cell Motility*, 25(4-5):337–341, July 2004.

[96] B D Lucas and T Kanade. An iterative image registration technique with an application to stereo vision. *Proceedings 7th International Joint Conference on Artificial Intelligence*, pages 674–679, 1981.

[97] Tianzhi Luo, Krithika Mohan, Pablo A Iglesias, and Douglas N Robinson. Molecular mechanisms of cellular mechanosensing. *Nature Materials*, 12(11):1064–1071, October 2013.

[98] W Luo, C h Yu, Z Z Lieu, J Allard, A Mogilner, M P Sheetz, and A D Bershadsky. Analysis of the local organization and dynamics of cellular actin networks. *The Journal of Cell Biology*, 202(7):1057–1073, September 2013.

[99] Matthias Machacek, Louis Hodgson, Christopher Welch, Hunter Elliott, Olivier Pertz, Perihan Nalbant, Amy Abell, Gary L Johnson, Klaus M Hahn, and Gaudenz Danuser. Coordination of Rho GTPase activities during cell protrusion. *Nature*, 461(7260):99–103, August 2009.

[100] F MacKintosh, J Käs, and P Janmey. Elasticity of Semiflexible Biopolymer Networks. *Physical Review Letters*, 75(24):4425–4428, December 1995.

[101] F MacKintosh and A Levine. Nonequilibrium Mechanics and Dynamics of Motor-Activated Gels. *Physical Review Letters*, 100(1):018104(4), January 2008.

[102] Makoto Makishima, Yoshio Honma, Motoo Hozumi, Kazumi Sampi, Masao Hattori, and Kazuo Motoyoshi. Induction of differentiation of human leukemia cells by inhibitors of myosin light chain kinase. *FEBS Letters*, 287(1-2):175–177, August 1991.

[103] Adam C Martin. Pulsation and stabilization: Contractile forces that underlie morphogenesis. *Developmental Biology*, 341(1):114–125, May 2010.

[104] Adam C Martin, Michael Gelbart, Rodrigo Fernandez-Gonzalez, Matthias Kaschube, and Eric F Wieschaus. Integration of contractile forces during tissue invagination. *The Journal of Cell Biology*, 188(5):735–749, 2010.

[105] Adam C Martin, Matthias Kaschube, and Eric F Wieschaus. Pulsed contractions of an actin–myosin network drive apical constriction. *Nature*, 457(7228):495–499, November 2008.

[106] Fumio Matsumura. Regulation of myosin II during cytokinesis in higher eukaryotes. *Trends In Cell Biology*, 15(7):371–377, July 2005.

[107] Mirjam Mayer, Martin Depken, Justin S Bois, Frank Jülicher, and Stephan W Grill. Anisotropies in cortical tension reveal the physical basis of polarizing cortical flows. *Nature*, 467(7315):617–621, September 2010.

[108] A Mazumder and G V Shivashankar. Emergence of a prestressed eukaryotic nucleus during cellular differentiation and development. *Journal of The Royal Society Interface*, 7(Suppl-3):S321–S330, April 2010.

[109] Russell E McConnell, James N Higginbotham, David A Shifrin, David L Tabb, Robert J Coffey, and Matthew J Tyska. The enterocyte microvillus is a vesicle-generating organelle. *The Journal of Cell Biology*, 185(7):1285–1298, 2009.

[110] Etienne Mémin and Patrick Pérez. Hierarchical Estimation and Segmentation of Dense Motion Fields - Springer. *International Journal of Computer Vision*, 46(2):129–155, 2002.

[111] D Mizuno, C Tardin, C F Schmidt, and F C MacKintosh. Nonequilibrium Mechanics of Active Cytoskeletal Networks. *Science*, 315:370–373, 2007.

[112] Rosalind E Mott and Brian P Helmke. Mapping the dynamics of shear stress-induced structural changes in endothelial cells. *American Journal of Physiology - Cell physiology*, 293(5):C1616–26, November 2007.

[113] P Naumanen, P Lappalainen, and P Hotulainen. Mechanisms of actin stress fibre assembly. *Journal of Microscopy*, 231(3):446–454, September 2008.

[114] W J Nelson and C Yeaman. Protein trafficking in the exocytic pathway of polarized epithelial cells. *Trends In Cell Biology*, 11(12):483–486, 2001.

[115] R Niederman and T D Pollard. Human platelet myosin. II. In vitro assembly and structure of myosin filaments. *The Journal of Cell Biology*, 67(1):72–92, October 1975.

[116] Anjaruwee S Nimnual, Laura J Taylor, and Dafna Bar-Sagi. Redox-dependent downregulation of Rho by Rac. *Nature Cell Biology*, 5(3):236–241, February 2003.

[117] Lucy Erin O'Brien, Mirjam M P Zegers, and Keith E Mostov. Opinion: Building epithelial architecture: insights from three-dimensional culture models. *Nature Reviews Molecular Cell Biology*, 3(7):531–537, July 2002.

[118] Eric A Osborn, Aleksandr Rabodzey, C Forbes Dewey, and John H Hartwig. Endothelial actin cytoskeleton remodeling during mechanostimulation with fluid shear stress. *American Journal of Physiology - Cell physiology*, 290(2):C444–52, February 2006.

[119] N Otsu. A threshold selection method from gray-level histograms. *IEEE TRANSACTIONS ON SYSTEMS, MAN, AND CYBERNETICS*, SMC-9(No.1):62–66, January 1979.

[120] D Pantaloni. Mechanism of Actin-Based Motility. *Science*, 292(5521):1502–1506, May 2001.

[121] Anant B Parekh and Jr James W Putney. Store-Operated Calcium Channels. *Physiological Reviews*, 85(2):757–810, April 2005.

[122] J Pawley. Handbook of Biological Confocal Microscopy - James Pawley - Google Books. 2010.

[123] Olivier Pertz, Louis Hodgson, Richard L Klemke, and Klaus M Hahn. Spatiotemporal dynamics of RhoA activity in migrating cells. *Nature Cell Biology*, 440(7087):1069–1072, March 2006.

[124] Robert D Phair, Stanislaw A Gorski, and Tom Misteli. Measurement of Dynamic Protein Binding to Chromatin In Vivo, Using Photobleaching Microscopy. In *Methods in Enzymology*, pages 393–414. Elsevier, 2003.

[125] P-Y Plaçais, M Balland, T Guérin, J-F Joanny, and P Martin. Spontaneous oscillations of a minimal actomyosin system under elastic loading. *Physical Review Letters*, 103(15):158102(4), October 2009.

[126] T D Pollard and G G Borisy. Cellular motility driven by assembly and disassembly of actin filaments. *Cell*, 112(4):453–465, 2003.

[127] T D Pollard and J A Cooper. Actin, a Central Player in Cell Shape and Movement. *Science*, 326(5957):1208–1212, November 2009.

[128] K Poole and D Müller. Flexible, actin-based ridges colocalise with the $\beta 1$ integrin on the surface of melanoma cells. *British Journal of Cancer*, 92(8):1499–1505, April 2005.

[129] Kate Poole, Doris Meder, Kai Simons, and Daniel Müller. The effect of raft lipid depletion on microvilli formation in MDCK cells, visualized by atomic force microscopy. *FEBS Letters*, 565(1-3):53–58, May 2004.

[130] D Pruyne. Role of Formins in Actin Assembly: Nucleation and Barbed-End Association. *Science*, 297(5581):612–615, June 2002.

[131] Myrto Raftopoulou and Alan Hall. Cell migration: Rho GTPases lead the way. *Developmental Biology*, 265(1):23–32, January 2004.

[132] Matteo Rauzi, Pierre-François Lenne, and Thomas Lecuit. Planar polarized actomyosin contractile flows control epithelial junction remodelling. *Nature*, 468(7327):1110–1114, November 2010.

[133] Matteo Rauzi, Pascale Verant, Thomas Lecuit, and Pierre-François Lenne. Nature and anisotropy of cortical forces orienting Drosophila tissue morphogenesis. *Nature Cell Biology*, 10(12):1401–1410, November 2008.

[134] Emil Reisler, Craig Smith, and George Seegan. Myosin minifilaments. *Journal of Molecular Biology*, 143(1):129–145, October 1980.

[135] C Revenu, F Ubelmann, I Hurbain, F El-Marjou, F Dingli, D Loew, D Delacour, J Gilet, E Brot-Laroche, F Rivero, D Louvard, and S Robine. A new role for the architecture of microvillar actin bundles in apical retention of membrane proteins. *Molecular Biology of the Cell*, 23(2):324–336, January 2012.

[136] A J Ridley, P M Comoglio, and A Hall. Regulation of scatter factor/hepatocyte growth factor responses by Ras, Rac, and Rho in MDCK cells. *Molecular and Cellular Biology*, 15(2):1110–1122, 1995.

[137] Anne J Ridley. Rho GTPases and actin dynamics in membrane protrusions and vesicle trafficking. *Trends In Cell Biology*, 16(10):522–529, October 2006.

[138] Julia Riedl, Alvaro H Crevenna, Kai Kessenbrock, Jerry Haochen Yu, Dorothee Neukirchen, Michal Bista, Frank Bradke, Dieter Jenne, Tad A Holak, Zena Werb, Michael Sixt, and Roland Wedlich-Söldner. Lifeact: a versatile marker to visualize F-actin. *Nature Methods*, 5(7):605–607, 2008.

[139] Ken Ritchie, Ryota Iino, Takahiro Fujiwara, Kotono Murase, and Akihiro Kusumi. The fence and picket structure of the plasma membrane of live cells as revealed by single molecule techniques (Review). *Molecular Membrane Biology*, 20(1):13–18, January 2003.

[140] M Roh-Johnson, G Shemer, C D Higgins, J H McClellan, A D Werts, U S Tulu, L Gao, E Betzig, D P Kiehart, and B Goldstein. Triggering a Cell Shape Change by Exploiting Preexisting Actomyosin Contractions. *Science*, 335(6073):1232–1235, March 2012.

[141] I Royal, N Lamarche-Vane, L Lamorte, K Kaibuchi, and M Park. Activation of Cdc42, Rac, PAK, and Rho-Kinase in Response to Hepatocyte Growth Factor Differentially Regulates Epithelial Cell Colony Spreading and Dissociation. *Molecular Biology of the Cell*, 11(5):1709–1725, May 2000.

[142] T Sakamoto, J Limouze, C A Combs, and A F Straight. Blebbistatin, a Myosin II Inhibitor, Is Photoinactivated by Blue Light - Biochemistry . *Biochemistry*, 44:584–588, 2005.

[143] G Salbreux, G Charras, and E Paluch. Actin cortex mechanics and cellular morphogenesis. *Trends In Cell Biology*, 22(10):536–545, 2012.

[144] G Salbreux, J F Joanny, J Prost, and P Pullarkat. Shape oscillations of non-adhering fibroblast cells. *Physical Biology*, 4(4):268–284, December 2007.

[145] P Sand and S Teller. Particle Video: Long-Range Motion Estimation Using Point Trajectories - Springer. *International Journal of Computer Vision*, 80:72–91, 2008.

[146] Eva E Sander, Jean P ten Klooster, Sanne van Delft, Rob A van der Kammen, and John G Collard. Rac Downregulates Rho Activity: Reciprocal Balance between Both Gtpases Determines Cellular Morphology and Migratory Behavior. *The Journal of Cell Biology*, 147(5):1009–1021, November 1999.

[147] I F Sbalzarini and P Koumoutsakos. Feature point tracking and trajectory analysis for video imaging in cell biology. *Journal of Structural Biology*, 151(2):182–195, August 2005.

[148] Hermann Schillers, Mike Wälte, Katarina Urbanova, and Hans Oberleithner. Real-Time Monitoring of Cell Elasticity Reveals Oscillating Myosin Activity. *Biophysical Journal*, 99(11):3639–3646, December 2010.

[149] Johannes Schindelin, Ignacio Arganda-Carreras, Erwin Frise, Verena Kaynig, Mark Longair, Tobias Pietzsch, Stephan Preibisch, Curtis Rueden, Stephan Saalfeld, Benjamin Schmid, Jean-Yves Tinevez, Daniel James White, Volker Hartenstein, Kevin Eliceiri, Pavel Tomancak, and Albert Cardona. Fiji: an open-source platform for biological-image analysis. *Nature Methods*, 9(7):676–682, July 2012.

[150] Khurana Seema and Sudeep P George. The role of actin bundling proteins in the assembly of filopodia in epithelial cells. *Cell Adhesion & Migration*, 5(5):409–420, 2011.

[151] Xavier Serra-Picamal, Vito Conte, Romaric Vincent, Ester Anon, Dhananjay T Tambe, Elsa Bazellieres, James P Butler, Jeffrey J Fredberg, and Xavier Trepat. Mechanical waves during tissue expansion. *Nature Physics*, 8(8):628–634, July 2012.

[152] Nathan C Shaner, Paul A Steinbach, and Roger Y Tsien. A guide to choosing fluorescent proteins. *Nature Methods*, 2(12):905–909, December 2005.

[153] Osamu Shimomura, Frank H Johnson, and Yo Saiga. Extraction, Purification and Properties of Aequorin, a Bioluminescent Protein from the Luminous Hydromedusan,Aequorea. *Journal of Cellular and Comparative Physiology*, 59(3):223–239, June 1962.

[154] G V Shivashankar. Mechanosignaling to the Cell Nucleus and Gene Regulation. *Annual Review of Biophysics*, 40(1):361–378, June 2011.

[155] Jerome Solon, Aynur Kaya-Çopur, Julien Colombelli, and Damian Brunner. Pulsed Forces Timed by a Ratchet-like Mechanism Drive Directed Tissue Movement during Dorsal Closure. *Cell*, 137(7):1331–1342, June 2009.

[156] Andrew P Somlyo and Avril V Somlyo. Ca2+ Sensitivity of Smooth Muscle and Nonmuscle Myosin II: Modulated by G Proteins, Kinases, and Myosin Phosphatase. *Physiological Reviews*, 83(4):1325–1358, October 2003.

[157] I Spector, N R Shochet, Y Kashman, and A Groweiss. Latrunculins: novel marine toxins that disrupt microfilament organization in cultured cells. *Science*, 219:493–495, 1983.

[158] B Sprague and J Mcnally. FRAP analysis of binding: proper and fitting. *Trends In Cell Biology*, 15(2):84–91, February 2005.

[159] Michael Stoker, Ermanno Gherardi, Marion Perryman, and Julia Gray. Scatter factor is a fibroblast-derived modulator of epithelial cell mobility. *Nature*, 327(6119):239–242, May 1987.

[160] A F Straight, A Cheung, J Limouze, and I Chen. Dissecting Temporal and Spatial Control of Cytokinesis with a Myosin II Inhibitor. *Science*, 299:1743–1747, 2003.

[161] M C Subauste. Rho Family Proteins Modulate Rapid Apoptosis Induced by Cytotoxic T Lymphocytes and Fas. *Journal of Biological Chemistry*, 275(13):9725–9733, March 2000.

[162] J Swift, I L Ivanovska, A Buxboim, T Harada, P C D P Dingal, J Pinter, J D Pajerowski, K R Spinler, J W Shin, M Tewari, F Rehfeldt, D W Speicher, and D E Discher. Nuclear Lamin-A Scales with Tissue Stiffness and Enhances Matrix-Directed Differentiation. *Science*, 341(6149):1240104–1240104, August 2013.

[163] Dhananjay T Tambe, C Corey Hardin, Thomas E Angelini, Kavitha Rajendran, Chan Young Park, Xavier Serra-Picamal, Enhua H Zhou, Muhammad H Zaman, James P Butler, David A Weitz, Jeffrey J Fredberg, and Xavier Trepat. Collective cell guidance by cooperative intercellular forces. *Nature Materials*, 10(6):469–475, June 2011.

[164] Shang-You Tee, Jianping Fu, Christopher S Chen, and Paul A Janmey. Cell Shape and Substrate Rigidity Both Regulate Cell Stiffness. *Biophysical Journal*, 100(5):L25–L27, March 2011.

[165] Jean Paul Thiery, Hervé Acloque, Ruby Y J Huang, and M Angela Nieto. Epithelial-Mesenchymal Transitions in Development and Disease. *Cell*, 139(5):871–890, November 2009.

[166] Xavier Trepat, Linhong Deng, Steven S An, Daniel Navajas, Daniel J Tschumperlin, William T Gerthoffer, James P Butler, and Jeffrey J Fredberg. Universal physical responses to stretch in the living cell. *Nature*, 447(7144):592–595, May 2007.

[167] R Y Tsien. The green fluorescent protein . *Annual Review of Biochemistry*, 67:509–544, 1998.

[168] Frank N van Leeuwen, Hendrie E T Kain, Rob A van der Kammen, Frits Michiels, Onno W Kranenburg, and John G Collard. The Guanine Nucleotide Exchange Factor Tiam1 Affects Neuronal Morphology; Opposing Roles for the Small GTPases Rac and Rho. *The Journal of Cell Biology*, 139(3):797–807, 1997.

[169] Alex Veksler and Nir S Gov. Calcium-Actin Waves and Oscillations of Cellular Membranes. *Biophysical Journal*, 97(6):1558–1568, September 2009.

[170] A B Verkhovsky. Myosin II filament assemblies in the active lamella of fibroblasts: their morphogenesis and role in the formation of actin filament bundles. *The Journal of Cell Biology*, 131(4):989–1002, November 1995.

[171] Miguel Vicente-Manzanares, Xuefei Ma, Robert S Adelstein, and Alan Rick Horwitz. Non-muscle myosin II takes centre stage in cell adhesion and migration. *Nature Reviews Molecular Cell Biology*, 10(11):778–790, November 2009.

[172] Viola Vogel and Michael Sheetz. Local force and geometry sensing regulate cell functions. *Nature Reviews Molecular Cell Biology*, 7(4):265–275, February 2006.

[173] Ning Wang, Jessica D Tytell, and Donald E Ingber. Mechanotransduction at a distance: mechanically coupling the extracellular matrix with the nucleus. *Nature Reviews Molecular Cell Biology*, 10(1):75–82, January 2009.

[174] Toshiyuki Watanabe, Hiroshi Hosoya, and Shigenobu Yonemura. Regulation of Myosin II Dynamics by Phosphorylation and Dephosphorylation of Its Light Chain in Epithelial Cells. *Molecular Biology of the Cell*, 16:605–616, 2007.

[175] S A Weed and J T Parsons. Cortactin: coupling membrane dynamics to cortical actin assembly.: EBSCOhost. *Oncogene*, 20:6418–6434, 2001.

[176] H J Westphale, L Wojnowski, A Schwab, and H Oberleithner. Spontaneous membrane potential oscillations in Madin-Darby canine kidney cells transformed by alkaline stress - Springer. *Pflügers Archiv*, 421:218–223, 1992.

[177] Günther Woehlke and Manfred Schliwa. Directional motility of kinesin motor proteins. *Biochimica et Biophysica Acta (BBA) - Molecular Cell Research*, 1496(1):117–127, March 2000.

[178] L Wojnowski, J Hoyland, W T Mason, and A Schwab. Cell transformation induces a cytoplasmic Ca2+ oscillator in Madin-Darby canine kidney cells - Springer. *Pflügers Archiv*, 426:89–94, 1994.

[179] L Wojnowski, A Schwab, J Hoyland, and W T Mason. Cytoplasmic Ca2+ determines the rate of Ca2+ entry into Mardin-Darby canine kidney-focus (MDCK-F) cells - Springer. *Pflügers Archiv*, 426:95–100, 1994.

[180] William Wood and Paul Martin. Structures in focus—filopodia. *The International Journal of Biochemistry & Cell Biology*, 34(7):726–730, July 2002.

[181] Michele A Wozniak and Christopher S Chen. Mechanotransduction in development: a growing role for contractility. *Nature Reviews Molecular Cell Biology*, 10(1):34–43, January 2009.

[182] M Zimmer. Green fluorescent protein (GFP): applications, structure, and related photophysical behavior. *Chemical Reviews*, 102(3):759–781, 2002.

[183] Joshua Zimmerberg and Michael M Kozlov. How proteins produce cellular membrane curvature. *Nature Reviews Molecular Cell Biology*, 7(1):9–19, November 2005.

[184] G C M Zondag. Oncogenic Ras Downregulates Rac Activity, which Leads to Increased Rho Activity and Epithelial-Mesenchymal Transition. *The Journal of Cell Biology*, 149(4):775–782, May 2000.

[185] Natalie Zwing. Bachelor Thesis: Structural and dynamical characterization of non-muscle myosin heavy chain II-B in epithelial MDCK II cells. March 2014.

Acknowledgements

Fünf Jahre nach der Diplomarbeit ist es wieder soweit. Ich kann wieder sagen - Geschafft. Und es ist wohl das letzte Mal, dass ich eine Seite füllen darf mit Danksagungen an Menschen, die mir nicht nur geholfen, sondern häufig genug auch persönlich viel bedeutet haben. Da wäre als aller Erstes - Roland, bitte verzeih mir - Barbara, der ich nach der Diplomarbeit noch als Freundin, und nun endlich als meiner Frau danken darf, vor allem dafür, dass sie in den letzten Monaten dieser Arbeit mit engelsgleicher Geduld mein ständiges Fehlen für Sie und unsere junge Tochter Ella ertragen hat und die ganze junge Familie alleine auf Kurs gehalten hat.

Als nächstes gilt natürlich mein besonderer Dank Roland Wedlich-Söldner, der mir diese Arbeit in seiner Gruppe ermöglicht hat und Prof. J. Rädler, dass er mich als Doktorvater betreut hat, obwohl ich als externer Doktorand eigentlich nie für ihn zur Verfügung stand und ich ihm, wie auch Dr. Carsten Grasshoff, dem hiermit auch herzlich gedankt sei, nur Arbeit durch vorweihnachtliche Statusreporte verursacht habe. Prof. E. Frey, Prof. J. Lipfert und Prof. T. Liedl möchte ich herzlich für ihre Bereitschaft danken, in meiner Prüfungskommission mitzuwirken und mich mit Fragen zu überhäufen. Des Weiteren möchte ich natürlich dem IMPRS-LS Programm des MPI unter dem Koordinator H.J. Schaeffer danken für die immensen Möglichkeiten, sich sowohl persönlich als auch wissenschaftlich weiterbilden zu können.

Doch bevor ich weiter Wissenschaftlern danke, möchte ich zunächst noch einmal meinen Eltern für die immer währende Unterstützung danken, die zwar nun zum Glück nicht mehr finanzieller, doch oft genug noch ideeller Art ist.

Mein tiefer Dank geht natürlich auch an unsere Arbeitsgruppe mit Tina, Gisela, Julia, Nikola, Kaja, Felix, Alvaro, Anoop und Jon, die sich nun leider in alle Winde zerstreut hat. Ganz besonders danken möchte ich Roland Aufschnaiter, der nicht nur durch Ruhe und Weitblick einige Konflikte entschärft, sondern vor allem immer mit perfektem Rat und Tat zur Seite stand, wenn ich mal wieder die Richtung verloren hatte. Bei Doris Berchtold möchte ich mich bedanken für zwei Jahre, in denen nicht nur auf Arbeit viel Stress durch teilweise völlig sinnfreies, doch befreiendes Quatschen abgebaut wurde, sondern in denen ich, auch auf einigen Bergtouren, viel Unterstützung bezüglich meiner Arbeit bekommen habe. Bei Johannes Fels möchte ich mich für die unkomplizierte und extrem hilfsbereite Unterstützung bei allen AFM Aufnahmen bedanken und wünsche ihm für die Fortführung des Projekts in Rolands Gruppe alles Erdenklich Gute. Bleibt mir zu guter letzt nur noch, herzlichst Amit Gupta und Christine Kienzle zu danken. Amit dafür, dass er es wirklich geschafft hat, die komplette Doktorarbeit Korrektur zu lesen und Christine sowohl fürs Korrekturlesen der Arbeit, als auch für die vielen Male in den letzen Monaten, in denen sie mir in Momenten der Verzweiflung gut zugesprochen hat. Allen, die ich nun vergessen habe, zu danken, verzeihen mir hoffentlich und nehmen den nun hiermit ausgesprochenen anonymen Dank an - Danke.